Characterization of Bax and Drp1 during apoptosis with advanced microscopy techniques

Dissertation

der Mathematisch-Naturwissenschaftlichen Fakultät

der Eberhard Karls Universität Tübingen

zur Erlangung des Grades eines

Doktors der Naturwissenschaften

(Dr. rer. nat.)

vorgelegt von

Raquel Salvador Gallego

aus Zaragoza, Spanien

Tübingen

2016

Gedruckt mit Genehmigung der Mathematisch-Naturwissenschaftlichen Fakultät der Eberhard Karls Universität Tübingen.

Tag der mündlichen Qualifikation:	13.07.2016
Dekan:	Prof. Dr. Wolfgang Rosenstiel
1. Berichterstatter:	Prof. Dr. Ana J. García Sáez
2. Berichterstatter:	Prof. Dr. Doron Rapaport
3. Berichterstatter:	Prof. Dr. Jean-Claude Martinou

Summary

Bax is a pro-apoptotic Bcl-2 family member that experiences a net translocation from the cytosol to mitochondria under cell stress. It inserts and oligomerizes irreversibly in the mitochondrial outer membrane (MOM) to mediate its permeabilization, leading to cytochrome c release and cell death. Bax translocation also correlates with massive mitochondrial fragmentation. Indeed, Bax colocalizes with the dynamin-related protein 1 (Drp1) at fission sites during apoptosis. However, the molecular basis behind Bax function and the nature of Bax structures responsible for MOM permeabilization remain poorly understood.

In this thesis, we studied the nanoscale spatial organization of Bax at mitochondria of apoptotic cells using dual-color super-resolution microscopy. We also investigated Bax interplay with Drp1 at the single-molecule level by fluorescence cross-correlation spectroscopy (FCCS).

We show that active Bax assembled into distinct architectures including full rings, arcs, and lines that localized in discrete foci along mitochondria in close association with Drp1 foci. The physiological relevance of these structures is supported by the different organization adopted by an inactive mutant that constitutively localizes at the MOM. Remarkably, both rings and arc-shaped oligomeric assemblies of Bax perforated the membrane, as revealed by atomic force microscopy in lipid bilayers.

Moreover, in vitro FCCS assays with recombinant proteins in single-vesicle approaches threw light upon the interaction between Bax and Drp1, where the membrane environment has an active contribution.

Our data identify the supramolecular organization of Bax during apoptosis and support a molecular mechanism in which Bax fully or partially delineates pores of different sizes to permeabilize the MOM. Altogether, our results contribute to the understanding of the interplay between the mitochondrial fission machinery and cell death regulation.

Zusammenfassung

Bax ist ein pro-apoptotisches Mitglied der Bcl-2 Proteinfamilie, das während Zellstress vom Cytosol zur den Mitochondrien bewegt. Bax dringt in die mitochondrialen Außenmenbran ein. Durch Oligomerisierung bildet es Poren durch die Cyt c entweicht, was letztlich zum Zelltod führt. Die Translokation von Bax korreliert auch mit der massiven Fragmentierung von Mitochondrien. Zusätzlich kolokalisiert Bax mit dem Dynamin-verwandten Protein 1 (Drp1) an den Teilungsregion der Mitochondrien während Apoptose. Allerdings sind die molekularen Grundlagen der Funktion von Bax sowie die strukturelle Anordnung dieses Proteins bei der Membran-Permeabilisierung weitgehend unbekannt.

In der vorliegenden Arbeit haben wir die Nano-Anordnung von Bax in apoptotischen Mitochondrien mit zweifarbigen hochauflösenden Mikroskopie ermittelt. Weiter haben wir auch das Zusammenspiel zwischen Bax und Drp1 auf Einzelmolekülebene mit Hilfe von Fluoreszenz-Kreuzkorrelations-Spektroskopie (FCCS) untersucht.

Unser Ergebnis zeigt, dass aktives Bax Ringe, unvollständige Ringe, Bögen und Linien entlang der Mitochondrien in enger Verbingung mit Drp1 ausbildet. Die physiologische Bedeutung dieser Strukturen wird von einer inaktiven, konstitutiv Membran-gebundenen Mutante von Bax unterstützt, die nicht dieselben Anordnungen an der Membran zeigt. Bemerkenswert hierbei ist, dass sowohl volle als auch unvollständige Ringe die Membran durchlöcherten, wie Atomkraftmikroskopie mit Lipiddoppelschichten zeigte.

Außerdem, gaben in vitro FCCS Untersuchungen einen Einblick in das Bax-Drp1 Zusammenspiel, wobei die Membranumgebung einen essentiellen Beitrag leistet.

Unsere Studien haben den supramolekularen Aufbau von Bax während der Apoptose aufgeklärt. Hierbei unterstützen die Daten einen molekularen Mechanismus bei dem Bax gänzlich oder teilweise Poren unterschiedlicher Größe ausbildet um die mitochondriale Außenmembran zu permeabilisieren. Zussamenfassend trägt diese Arbeit zu unserem Verständis des Zusammenspiels zwischen mitochondrieller Dynamik und programmiertem Zelltod bei.

Contents

List of Figures

List of Tables

Nomenclature

Bak Bcl-2 homologous antagonist killer

Bax Bcl-2 associated protein X

Bcl-2 B-cell lymphoma 2

Bcl-xL B-cell lymphoma extra large

BH Bcl-2 homology domain

Bid BH3 interacting domain death agonist

BSA Bovine serum albumi

CL Cardiolipin

cyt c Cytochrome c

DISC Death inducing signaling complex

DOPC 1,2-Dioleoyl-sn-glycero-3-phosphocholine

Drp1 Dynamin related protein 1

FCCS Fluorescence cross-correlation spectroscopy

FCS Fluorescence correlation spectroscopy

GUV Giant unilamellar vesicle

MIM Mitochondrial inner membrane

MOM Mitochondrial outer membrane

MPT Mitochondrial permeability transition

PARP Poly ADP ribose polymerase

PE Egg L-α-phosphatidylethanolamine

PMT Photomultiplier

RIPK Receptor interacting protein kinase

SMLM Single molecule localization microscopy

STED Stimulated emission depletion microscopy

TNF Tumor necrosis factor

Part I.

Introduction

1 Programmed cell death

Billions of cells die in our body every day, but when can we state that a cell is dying, or really dead? These concepts have kept researchers busy for the last decades and many definitions and nomenclatures concerning a cell's life path have been published. In 2009, The Nomenclature Committee on Cell Death (NCCD) collected this hodgepodge of terminologies and agreed on a universal criteria for the definition of cell death characteristics and morphology, which is continuously updated. According to the NCCD, there is an irreversible point that a cell reaches in the dying process. Depending on the type of cell death, this step can be characterized by: externalization of phospatidylserine, extensive caspase activation, loss of mitochondrial membrane potential, or permeabilization of the mitochondrial outer membrane (MOM). If the cell loses the plasma membrane integrity, it is fragmented into bodies and these fragments are eaten by the neighboring cells, then death can be confirmed (Kroemer et al., 2009).

It was not until 1965 when the term "programmed cell-death" (PCD) was officially used to define a controlled, intracellular, self-destruction process observed in insect cells during their development (Lockshin and Williams, 1965). Some years later, "apoptosis" came onto the scene to name a specific type of programmed cell death with conserved morphological features (Kerr et al., 1972). While this is the most acclaimed form, additional types of programmed cell death with unique phenotypes and biochemical characteristics have arisen, including autophagy, necroptosis, cornification and other minor types. In this chapter, I will introduce the different PCD types and comment on their differences and similarities, and then focus on apoptosis.

1.1. Apoptosis

Although it may sound illogical, the destruction of cells is as essential as their creation in the course of proper formation, growth and development of multi-cellular organisms. Most of the cells bring about their demise through apoptosis (from the Greek, "fall off"). Far from being random, this process is deliberately controlled and programmed, following a specific hierarchy of molecular events. The term was first coined by J Kerr and colleagues (Kerr et al., 1972) and ever since, scientists have worked tirelessly to deeply understand the significance, regulation and mechanisms behind this transcendent process. It has long been known that the size and shape of some tissues are determined by a coordination of cell death patterns. Our webbed limbs give rise to separate fingers and toes when cells between them

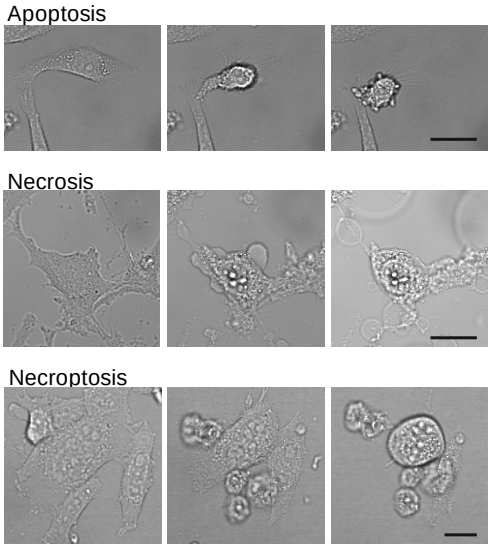

Figure 1.1. Programmed cell death morphology. Cell shape transformation after induction of different types of cell death. Left panels show healthy cells and middle and right panels show sequential induction times.

die (Zakeri et al., 1994) and programmed cell death also sculpts other organs such as the intestine or the palate (Cuervo and Covarrubias, 2004). During the development of the nervous system, cells that are not needed for proper synaptic connections have to be removed (Kim and Sun, 2011). Besides characterizing tissue and organ morphogenesis, apoptosis helps to maintain cellular homeostasis, for instance, by killing cells of the uterine wall during menstruation (Li et al., 2005). Moreover, cells also kill themselves off when they sense a potential threat to the organism, such as a virus infection or DNA damage (Hardwick, 2001).

In order to function correctly, adult tissues need a perfect balance between cell proliferation and death, and apoptosis mismanagement can carry fatal consequences. Excessive cell death causes tissue damage and is associated with the occurrence of strokes, heart attacks or diseases such as Alzheimer's and Parkinson's (Su et al., 1994; Lev et al., 2003). On the other hand, if not enough cells die, then their massive accumulation in some organs can lead to a reaction against the organism's own cells, causing autoimmune diseases. The lack of apoptosis is also linked to tumor growth because cancer cells can escape the cell death signals and grow excessively, responding ineffectively to anti-cancer therapies (Vaux et al., 1988; Tsujimoto et al., 1984).

Apart from being essential to human development, apoptosis differs from other cell death types in the events that trigger it and in the morphological transformations that it generates. Apoptotic cells die in a rather "clean" way, without leaving a trace or awakening any inflammatory response. The apoptotic phenotype is characterized by cell shrinkage and overall round shape, chromatin condensation, organelle packing and plasma membrane blebbing. These blebs ultimately separate from the cell forming membrane-

enclosed apoptotic bodies which are rapidly eaten up by the neighboring cells or by macrophages (Fig. 1.1).

The main actors of apoptosis comprise a large set of proteins located in different cell compartments contributing to the process in a regulatory, receptive, adaptive or executioner manner. The discovery of the Bcl-2 mammalian gene laid the foundation to understand the apoptotic machinery, followed by the constitution of the Bcl-2 family of proteins, which are the key orchestrators of apoptosis. A family of cystein proteases known as caspases coordinate to dismantle the cell and act exclusively in the apoptotic play. They are commonly classified according to their function as initiators (caspase-2,-8,-9,-10), executioners (caspase-3,-6,-7) and inflammatory caspases (caspase-1,-4,-5). Caspases are first synthesized as inactive zymogens and become activated after diverse death signaling events, generating an activation cascade that allows the final controlled demolition of the cellular components(Kischkel, F.C., S Hellbardt, I Behrmann, M Germer, M Pawlita, P H Krammer, 1995). In addition, many induced transcription factors (ITFs), apoptogenic factors such as cytochrome c (cyt c), receptors of the tumor necrosis factor (TNF) family or particular lipids have a remarkable role in supporting the apoptotic scenario. Therefore, it is to be noted that the term apoptosis defines precise phenotypes and biochemical characteristics and should not be used as a mere synonym for programmed cell death.

1.2. Programmed necrosis

In contrast to apoptosis, necrosis leaves a more “chaotic” scenario. After an external insult such as an infection or a cut off in the blood supply, cells burst, swell and the intracellular components are spread to the extracellular milleu, inducing inflammation (Vandenabeele et al., 2010). Although it has been considered as an accidental and random type of cell death for a long time, growing evidence supports the existence of programmed necrosis, the most common form known as necroptosis (Degterev et al., 2005).

This controlled cell death becomes activated not only after physical damage, but also during neurodegeneration and ischemia. It was discovered as a back-up mechanism for cell suicide after the inhibition of caspases. Necroptosis is triggered in response to specific signal transduction pathways dependent mainly on one kinase: RIPK1. (Degterev et al., 2005). Other downstream kinases such as RIPK3 or the pseudo-kinase MLKL act as the executioners of the necroptotic cascade (Sun et al., 2012; Cai et al., 2014; Cho et al., 2009). The concept of programmed necrosis has been gaining ground with the implication of other components such as death domain receptors (e.g. TNFR1, Fas/CD95 and TRAIL-R), Toll-like receptors (e.g., TLR3 and TLR4) or NADPH oxidases. Besides necroptosis, mitochondrial permeability transition (MPT)-regulated necrosis and parthanatos, which depends on the activation of PARP , have been described as additional types of controlled necrosis (Jouan-Lanhouet et al., 2012). Despite the obvious discrepancies

with apoptosis, both processes seem to share some common mediators, such as some death receptors, the p53 gene and even certain Bcl-2 proteins (Muñoz-Pinedo, 2012; Golstein and Kroemer, 2007; Whelan et al., 2012) (Fig. 1.2).

1.3. Autophagy

Autophagy is a self-cannibalization mechanism designed for recycling long-living proteins and damaged organelles. During this conserved catabolic process, the cytoplasm suffers large vacuolization and the chromatin is usually not condensed, so cells can recover until the last stages of the process (Nikoletopoulou et al., 2013). The most studied type of autophagy is macroautophagy, where double-membrane vesicules (autophagosomes) surround the cytoplasmic macromolecules and other cellular components, targeting them for lysosomal degradation by specific hydrolases (Levine and Kroemer, 2008). Far from being just a recycle bin, autophagy can also be promoted during normal development and differentiation but excessive autophagy is also linked to the progression of some diseases (Ding et al., 2006; Nikoletopoulou et al., 2013). This dual role of autophagy in cell death and survival is therefore a matter of debate. Interestingly, a special type of autophagy implicated in mitochondria turnover has recently emerged and named mitophagy (Lemasters, 2005).

The crosstalk between autophagy and apoptosis is more than evident. Both are activated in response to metabolic stress and can collaborate to influence the cell's fate. Indeed, the Bcl-2 family member Mcl-1 acts as a stress sensor that coordinately controls autophagy and apoptosis (Germain et al., 2011). Furthermore, according to some reports, the autophagic protein Beclin-1 interacts with the anti-apoptotic proteins Bcl-2 and Bcl-xL; although these observations are still controversial in the field (Pattingre et al., 2005; Takacs-Vellai et al., 2005)(Fig. 1.2).

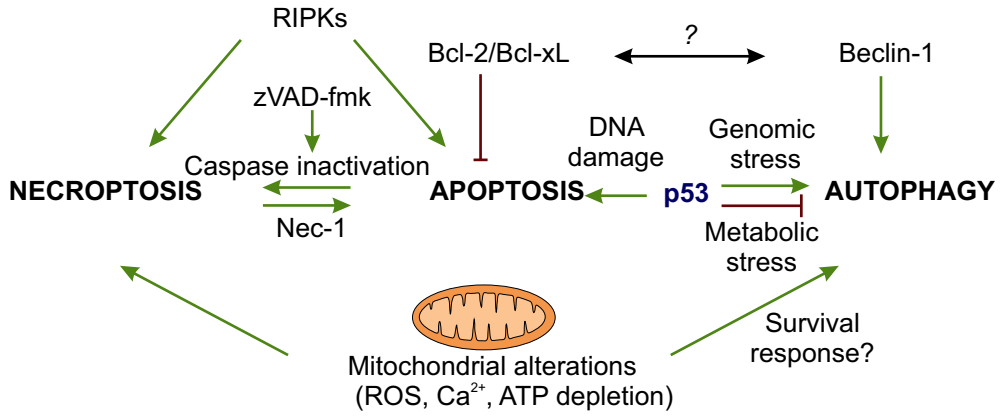

Figure 1.2. Interplay between different types of programmed cell death.

1.4. Other PCD types

The field of cell death has expanded tremendously and new cell death modalities have been outlined including cornification, mitotic catastrophe, anoikis, paraptosis, pyraptosis, and entosis. Cornification is seen as a particular epithelial differentation mechanism by the formation of corneocytes, which are dead keratynocites containing proteins and lipids that provide the necessary elasticity, stability and mechanical resitance to the skin (Candi et al., 2005). We can refer to mitotic catastrophe when cells die as a result of defective mitosis and experience micro- or multi-nucleation (Roninson et al., 2001). Anoikis represents an altered form of apoptosis induction, when cells detach from the substrate or from other cells (Grossmann, 2002). Paraptosis defines a particular cell death induced by the expression of insulin-like growth factor receptor 1. It involves cytoplasm vacuolization and mitochondrial swelling, but it is resistant to caspase inhibition and to overexpression of anti-apoptotic Bcl-2 proteins (Sperandio et al., 2000). Contrarily, pyroptosis was introduced as a caspase-1 dependent process suffered by macrophages after the infection with diverse pathogens (Fink and Cookson, 2007). Finally, entosis happens when one cell acts as a "cannibal" by engulfing a live neighbouring cell, which dies afterwards within the phagosome (Overholtzer et al., 2007). Regardless of the big increase in the number of publications related to PCD, the specific characteristics of these atypical types still need to be further elucidated.

2 Molecular pathways of apoptosis

The following chapter describes the details of the apoptotic process, starting with the leading pathways and including its intriguing regulators and the proposed models for its activation and control, as well as its connections with mitochondrial dynamics.

2.1. Highways to death

When a cell is committed to die via apoptosis, it can follow two main routes depending on the signals that have triggered the stress: the extrinsic or the intrinsic route (Fig. 2.1). The former gathers signals from the extracellular environment, while the latter responds to intracellular signals and it is often nicknamed as the "mitochondrial pathway". There is an additional secondary apoptosis pathway used by cytotoxic cells and induced via the secretion of a granule serine-protease, granzyme B. Despite the different starting points, these roads mostly converge at mitochondria and lead to the activation of the same executioner caspases, sharing the last stages of the apoptotic process (Elmore, 2007).

2.1.1. Extrinsic pathway

The extrinsic apoptotic pathway has proved vital for the correct functioning of the immune system. In this route, the signal for suicide comes from outside, through the ligation of surface receptors belonging mainly to the tumor necrosis factor (TNF) superfamily (Walczak and Krammer, 2000; Locksley et al., 2001; Fulda and Debatin, 2006). Some of the best studied ligand-receptor couples include FasL/FasR, TNF-α/TNFR1, Apo3L/DR3, Apo2L/DR4 and Apo2L/DR (Ashkenazi and Dixit, 1998; Rubio-Moscardo et al., 2005). After recruiting the apoptotic ligands in the extracellular side, the death receptors form trimers in the plasma membrane and undergo conformational changes. This leads to their interaction with intracellular cytoplasmatic adaptor proteins containing death domains, such as RIPK1, FADD (Fas-associated death domain protein) and c-FLIP. As a result, the death inducing signaling complex (DISC) is assembled, which promotes the auto-catalytic activation of procaspase-8, a further downstream activation of executioner caspases and ultimately cell death (Deveraux et al., 1998; Muzio et al., 1996; Lavrik et al., 2005) (Fig. 2.1). The final steps of this

route diverge according to the cell type. In type I cells (e.g.: lymphocytes), caspase-8 or 10 can directly cleave the executioner caspases, whereas type II cells (e.g., hepatocytes) require a detour through the mitochondrial pathway in order to conclude the process (Li et al., 1998; Scaffidi et al., 1998).

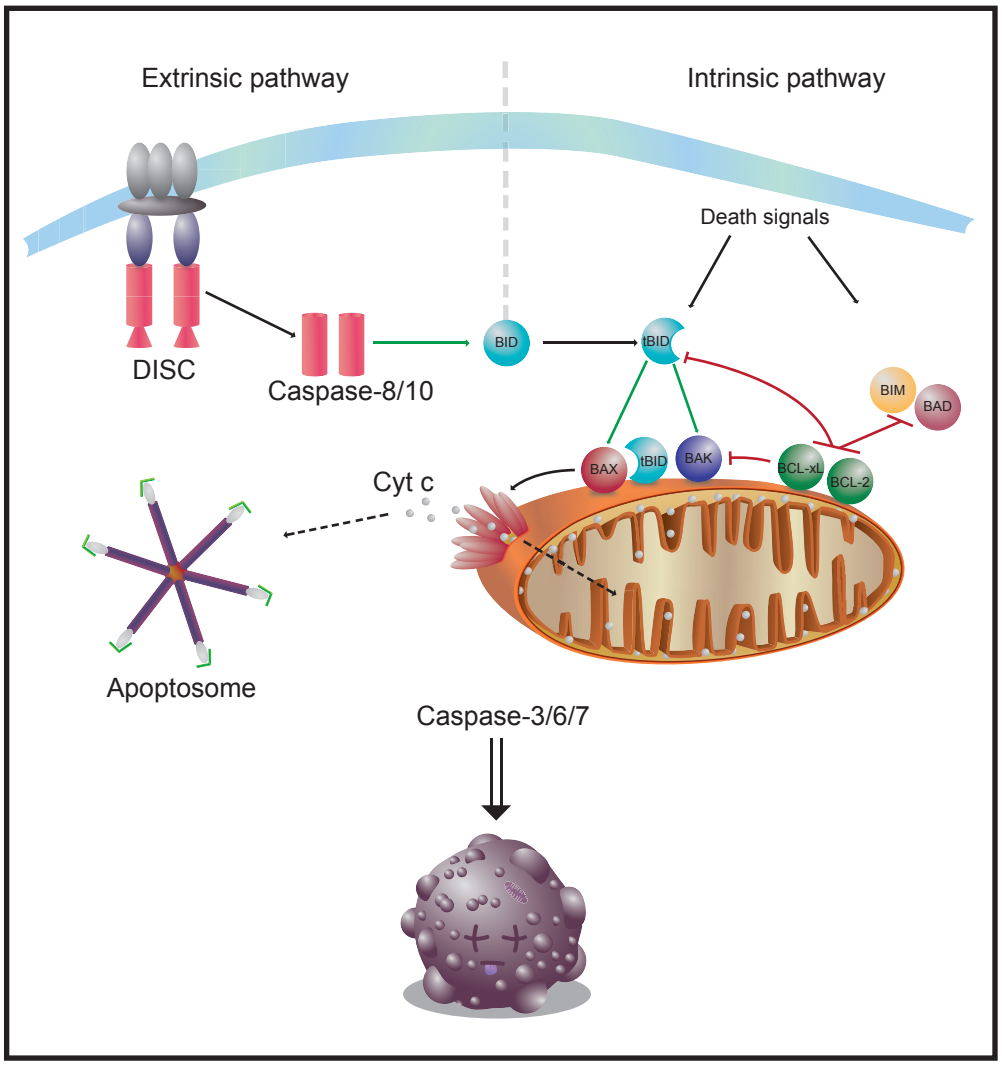

Figure 2.1. Main apoptotic pathways. In the extrinsic pathway, binding of ligands to the death receptors triggers the formation of the complex DISC. Activation of caspase-8 can activate BID by cleavage, which relays the death signal to the intrinsic pathway. When BH3-only proteins are activated, they can inhibit the anti-apoptotic Bcl-2 members and activate Bax and Bak, leading to MOMP and cell death.

2.1.2. Intrinsic pathway

When death stimuli reach the cell internally via a non receptor-mediated mechanism, such as radiation or oxidative stress, the intrinsic pathway of apoptosis is triggered (Green and Kroemer, 2004). The key event of no return

is the permeabilization of the mitochondrial outer membrane (MOMP) by pro-apoptotic members of the Bcl-2 family of proteins. Close to reaching this point, mitochondria experience membrane potential loss and functional and morphological alterations, such as fission, lipid peroxidation or cristae remodeling. Once the membrane is permeable, the so-called apoptotic factors are released from the intermembrane space of mitochondria into the cytosol. These include cyt c, SMAC/Diablo, Omi/HrtA2, Apoptosis Inducing Factor (AIF) and Endonuclease G (EndG). As a consequence, the apoptosome is formed, a multiprotein complex composed by cyt c, APAF-1 (apoptosis protease activating factor), initiator caspase 9 and ATP. Once active, this molecular platform can cleave caspase-9, leading in turn to further caspase-3 and -7 activation and finally to apoptotic cell death (Fig. 2.1).

2.1.3. Meeting point of apoptosis pathways at mitochondria

Although the connection between the release of certain mitochondrial-residing proteins in the cytosol and apoptosis progression was not established until the late 90s, it was soon taken for granted that mitochondria constitute a cross-road in the cell's suicide mechanism. Once mitochondria are severly compromised, cells will die no matter what, in a rather fast process. A regulator member of the Bcl-2 family called Bid connects the two main apoptotic routes (Luo et al., 1998) (see section 2.2). This pro-death protein is not only cleaved and activated during the intrinsic pathway but also by the active caspase-8 generated in the receptor pathway.

As mentioned earlier, mitochondria serve as a safe compartment where apoptotic factors are kept in healthy cells but discharged in a controlled manner after apoptotic insults. The small (12 kDa) electron carrier cyt c is one of the components of the apoptosome and is released into the cytosol after MOM permeabilization and oxidation of cardiolipin (CL), a mitchondrial lipid loosely associated to the MOM (Liu et al., 1996). Two larger proteins, SMAC/DIABLO (25 kDa) and Omi/HtrA2 (37 kDa) are also released to facilitate caspase activation by binding and neutralizing specific endogenous inhibitors of caspases (IAPs)(Saelens et al., 2004). AIF (62 kDa) and EndoG (23 kDa) translocate to the nucleus after their release and mediate chromatin condensation and DNA fragmentation (Parrish et al., 2001; Susin et al., 1996). There are different theories about the release order of all these proteins from the mitochondria. Some reports assume a step-wise dispensation of cyt c, SMAC/DIABLO, and AIF (Daugas et al., 2000; Chauhan et al., 2001) while others defend the simultaneous release of cyt c and SMAC/DIABLO (Rehm et al., 2003; Muñoz-Pinedo et al., 2006). One argument in favor of uncoordinated timing would be the different confinement mechanisms of these proteins within the mitochondria. For instance, AIF is anchored to the inner membrane and needs to be cleaved in order to be released, while more than 85% of the cyt c is bound to CL

on the cristae, which have to remodel before cyt c can be released. (Polster et al., 2005; Scorrano et al., 2002). Furthermore, it is unclear if the MOM pores can be size- and protein- selective, so that only specific factors could pass through.

2.2. Bcl-2 family: ying and yang of cell death

2.2.1. Origin and classification

In the 1980s, studies in human follicular lymphoma identified a new gene involved in the 14;18 chromosome translocation that was found to promote cell survival (Tsujimoto et al., 1984; Vaux et al., 1988). This oncogene, named B-cell lymphoma 2 (Bcl-2), was later linked to apoptosis due to its high homology with the gene that inhibits cell death in C. Elegnans (CED-9) (Hockenbery et al., 1990). Ever since, a long road has been paved towards the understanding of apoptotis regulation and Bcl-2 has given rise to a well matched family of proteins that work together to balance all the mechanisms involved in this pathway of programmed cell death.

All the members of this family share one or more of the four conserved Bcl-2 homology (BH) regions that determine to a big extent the proteins' function and classification (Fig. 2.2). When the four BH regions (BH1-BH4) are present, the Bcl-2 homologs are commonly anti-apoptotic, enclosing Bcl-2, Bcl-w, Bcl-xL, Mcl-1, and A1. If BH4 region is absent or modified, the proteins exhibit pro-apoptotic functions mainly due to pore forming properties (Bax, Bak, Bok). A third group contains only the BH3 domain, the so called BH3-only proteins, and has evolved to feel cellular stress and to regulate the other two groups to promote apoptosis. The BH3-only members can be further divided into sensitizers (e.g, Bad, Bmf, Bik, Noxa or Hrk), which only interact with antiapoptotic proteins to inhibit their effect, and direct activators (e.g: Bid, Bim, Puma), which also directly activate Bax and Bak (García-Sáez, 2012; Shamas-Din et al., 2011). An updated database compiling all the sequence, structural, and functional information about Bcl-2 proteins can be found here https://bcl2db.ibcp.fr/BCL2DB/

2.2.2. Structural details

Despite their opposing functions in cell death regulation, Bcl-2 homologs are evolutionary conserved and show high resemblance in structure and sequence (Petros et al., 2004). These small proteins can be found in a water-soluble, membrane-associated, or membrane-embedded conformation. The multi-domain members of the family share a common, globular fold consisting of a bundle of 9 or 10 α-helices. Helices 1 to 8 constitute the Bcl-2 core and the hydrophobic C-terminal helix α9 is tipically a transmembrane domain responsible for membrane anchoring. Strikingly, the Bcl-2 core fold is very similar to the pore-forming domain of some bacterial toxins, which

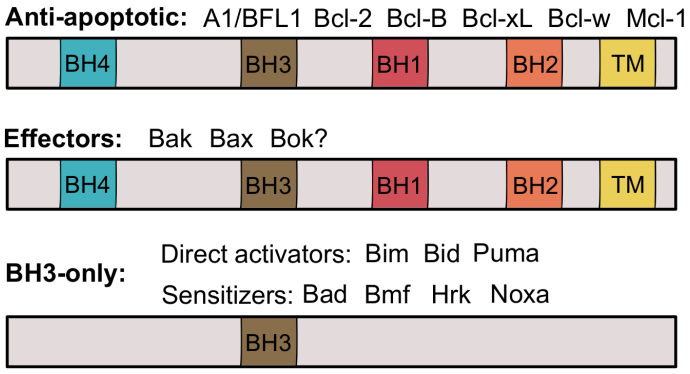

Figure 2.2. Bcl-2 family classification. Representation of the different Bcl-2 groups with the corresponding structural BH and transmembrane domains (TM).

can also adopt soluble and membrane structures (Muchmore et al., 1996; Petros et al., 2004).

While there is extensive detailed information about the tridimensional structure of Bcl-2 proteins in solution, the membrane structural knowledge is still limited. However, this situation is slowly changing thanks to the recent progress on this topic.

Solution

In the aqueous environment, the central hydrophobic hairpin of Bcl-2 homologs α5-α6 is surrounded by the rest of amphipatic helices of different lengths. The domains BH1 to BH3 are in close proximity and shape a hydrophobic cleft carved in the protein surface where the hydrophobic α9 is sequestered, rendering the protein hydrosoluble. If α9 is dispatched, this cleft becomes the binding site for the BH3 domains of other Bcl-2 proteins (Suzuki et al., 2000; Petros et al., 2000) (Fig. 2.3).

The first water soluble structure to be resolved was that of Bcl-xL lacking the C-terminal domain (Muchmore et al., 1996). The rest of the anti-apoptotic Bcl-2 members show a very similar fold, diverging mainly in the BH3-binding groove. In general, an increase in distance between α3 and α4 is the main rearrangement produced in anti-apoptotic proteins upon BH3-ligand binding. In the case of Bcl-xL, the plasticity of this segment enables the interaction with PUMA and prevents the binding of p53 (Follis et al., 2013). On the contrary, Mcl-1 shows a more loosely packed α3 and α4 helices, favored by regions with high positive electrostatic potential flanking the hydrophobic cleft (Day et al., 2005). Based on their BH3-binding patterns, we can distinguish two main types of soluble structures among the Bcl-2-like proteins, one including Bcl-xL, Bcl-w and Bcl-2 itself and the other enclosing Mcl-1 and A1 (Dutta et al., 2010; Certo et al., 2006).

Bax is an inactive monomeric protein in solution that also displays a central amphipathic hairpin surrounded by solvent-exposed helices. Its C-terminal tail resembles the one of Bcl-xL and it is normally hidden within the

surface groove preventing the binding to any potential partner (Muchmore et al., 1996; Suzuki et al., 2000; Moldoveanu et al., 2006). Nonetheless, BH3 ligands can also interact with Bax in a non-canonical way to an alternative cleft located in α1-α6. This association allosterically regulates the activation and oligomerization of Bax, as well as its interactions with external partners (Gavathiotis et al., 2008; Edwards et al., 2013; Leshchiner et al., 2013).

In turn, inactive Bak is constitutively bound to the MOM via the C-terminal helix α9, with the helices within the Bcl-2 core in a globular fold facing the cytosolic side. Nevertheless, studies with BH3 peptides have revealed that in Bak unbound state, the canonical BH grove is occluded by other means (Moldoveanu et al., 2013). Unlike Bax, Bak lacks a non-canonical groove, so in order to be activated by homo-oligomerization and to interact with other partners it has to adopt an open conformation making the BH cleft available for binding (Moldoveanu et al., 2013, 2006).

BH3-only proteins are physiologically unstructured, with the exception of Bid, which features a comparable Bcl-2 core architecture (Hinds et al., 2007). However, they can fold in a well-ordered helix upon binding to Bcl-2 partners. Bid has a disordered region between α2 and α3 that is targeted for cleavage by caspase 8, generating the active truncated form (tBID), in which the BH3 domain is exposed and ready for binding (Chou et al., 1999; McDonnell et al., 1999; Gross et al., 1999). This intrinsic disordered region has also been observed for other Bcl-2 members. For instance, Bcl-xL displays a flexible, unstructured loop placed between α1 and α2 that can be targeted by caspases, turning Bcl-xL into a pro-death Bax-like protein (Cheng et al., 1997; Basañez et al., 2001).

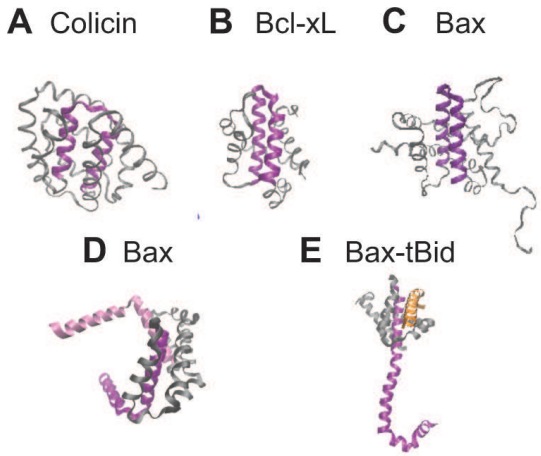

Figure 2.3. Structures of Bcl-2 proteins compared to the pore forming domain of colicin. The central hairpin is shown in purple and the rest in grey. (A) Soluble pore forming domain of colicin (PDB:). (B) Soluble form of human Bcl-xL without the C-terminal domain (PDB:1MAZ) (Muchmore et al., 1996). (C) Soluble form of Bax (Suzuki et al., 2000) . (D) Membrane form of Bax dimer in a clamp conformation (Bleicken et al., 2014). (E) Bax monomer forming part of the domain swapped dimer in complex with BidBH3 (Czabotar et al., 2013)

Membrane

During apoptosis, Bax and Bak form big clusters in the MOM to mediate its permeabilization. The indisputable analogy between Bcl-2 members and the pore-forming domains of bacterial toxins supposed a big boost to the structural understanding of the active, membrane-bound state of the killer Bcl-2 proteins (Muchmore et al., 1996). Bacterial toxins are believed to make a pore by penetrating the membrane with their two hydrophobic core helices arranged as a hairpin. Taking this into account, the "umbrella model" was introduced, implying that the central helices of Bak and Bax (α5 and α6) might insert across the MOM in an analogous way (Ros and García-Sáez, 2015; Cosentino et al., 2015; Annis et al., 2005). On that basis, several groundbreaking studies have come up with different structural models for Bax and Bak accommodation and aggregation in the MOM that defend or dispute this initial view.

As previously mentioned, Bak is a membrane integral protein with a sole interaction site for activation (BH groove). BH3 ligands bind transiently to this site, inducing a structural reorganization that ends up in an increasing distance between the core and latch Bak subdomains (Leshchiner et al., 2013; Moldoveanu et al., 2013; Brouwer et al., 2014). This separation drives the formation of Bak homo-dimers through their BH3 domains, which then evolve into high order oligomers that enable MOM permeabilization (Dewson et al., 2008). Although the longstanding hairpin insertion model for Bak (and Bax) has been supported by several membrane accesibility studies (García-Sáez et al., 2004; Annis et al., 2005), the trend is changing to a situation where α5 and α6 only interact superficially with the membrane (Bleicken et al., 2014; Westphal et al., 2014).

Bax is mainly a cytosolic protein in its inactive form, although it can also loosely bind to the MOM (Schellenberg et al., 2013; Todt et al., 2013). Its stepwise activation process begins with the binding of BH3-only proteins (Bid, Bim and maybe Puma) to the non-canonical cleft (Edwards et al., 2013; Gavathiotis et al., 2008; Lovell et al., 2008), which triggers the freeing of α9 from the BH-groove. This is followed by the building of a symmetric dimer interface by helices α2 to α4 and irreversible insertion in the MOM. Bax membrane-embedded form displays helices α5, α6 and α9 inaccessible to water, therefore pointing them as the best candidates to be tucked in the bilayer. In line with this observations, the initial "umbrella" model for active Bax proposed the insertion of the α5-α6 hairpin across the membrane, together with α9 (Annis et al., 2005). However, the only helix hydrophobic enough to be fully inserted in the bilayer is α9, and this model argues with evidences that show an unaltered and functional Bax BH-groove after membrane spanning, which would not be possible in the proposed arrangement.

Recent crystallography data with truncated forms of Bax in detergents suggested that the core hairpin is indeed completely open during Bax activation, resulting in the displacement of the latch and core domains, (like its "cousin"

Bak) (Czabotar et al., 2013; Brouwer et al., 2014). This situation would render an active Bax dimer where exclusively α9 would cross the membrane and the rest of the protein would lay on the bilayer surface, with helices α5 and α6 only partially inserted in it (Westphal et al., 2014) (Fig. 2.3). Taking into account the crystal structure, the structure of active, full-length Bax in the lipid membrane was further modeled by double electron-electron resonance (DEER) spectroscopy (Bleicken et al., 2014). The main highlight of this study confirms a partial opening of the α5-α6 hairpin, that allows Bax to adopt a clamp-like conformation on the lipid bilayer, crutial for the formation of active face-to-face dimers. These stable dimers would constitute the building blocks for further Bax homo-oligomerization in the membrane, observations that have also been confirmed by single-molecule studies with recombinant proteins and supported bilayers (Subburaj et al., 2015). In addition to the "dimerization domain" between α2 and α5, a flexible domain comprising α6 to α9 slightly pinches the membrane and would be responsible for inter-dimer interactions. The amphipatic helix α6 of each monomer would therefore lie on the surface of both membrane leaflets, favoring the formation of a lipidic pore, as discussed below (section 2.2.4 on page 29).

Although the full-length membrane-bound structure of anti-apoptotic Bcl-2's remains a mystery, structural studies with detergents and with peptides have nicely contributed to the literature on the association of these proteins to the membrane (Losonczi et al., 2000; Chi et al., 2014). The consensus view seems to be that they need to insert in the membrane to act as inhibitory proteins (García-Sáez et al., 2004; Losonczi et al., 2000). Indeed, the transmembrane tail of Bcl-xL is able to regulate the overall binding affinity of the protein and mediate Bax retrotranslocation (Todt et al., 2013). According to some reports, the integration of Bcl-xL in the membrane may lead to BH3-ligand release and induce considerable structural changes (Denisov et al., 2006; Basañez and Hardwick, 2008). A recent detergent-free study with nanodiscs fostered debate on this belief, showing that both soluble and membrane Bcl-xL conformations have high BH3 ligand affinity and that membrane embedding does not induce major conformational changes in the aqueous head, which retains the hydrophobic groove (Yao et al., 2015).

2.2.3. Bcl-2 family in action

It is not an easy task to unravel the precise mechanisms that this complex family of proteins follow to orchestrate the cell fate, but tantalizing clues have emerged over the years that give us a hint about how the Bcl-2 interaction network, together with other cellular factors and the MOM itself, harmonize in the course of apoptosis. In the literature, several models have been proposed to explain how Bcl-2 interactions inhibit or advocate MOM permeabilization, listed below (Fig. 2.4).

Direct model

According to this theory, the effectors Bax and Bak are constitutively inactive and have to be activated by BH3-only proteins in order to insert and oligomerize in the membrane. The activation can proceed by two means, which divide the BH3-only members in two subgoups (Letai et al., 2002; Kuwana et al., 2005). On one hand, the "direct activators" (e.g. Bim, tBid) can directly activate the killers Bax and Bak by binding. This is prevented by the association of the anti-apoptotic members to these direct activators, thereby inhibiting apoptosis. On the other hand, the "sensitizers" (e.g. Bad, Noxa) act by displacing the direct activators from their complexes with the anti-apoptotic members, therefore indirectly activating Bax and Bak. The antiapoptotic members can also inhibit activated Bax and Bak, which are released from the complex by both types of BH-3 only proteins. This scenario was supported by the high efficiency observed for tBid to enhance Bax and Bak permeabilizing function in model membranes (Kuwana et al., 2002; Bleicken et al., 2010; Oh et al., 2010). The main drawback of this method is the difficulty to detect interactions of the direct activators with Bax and Bak, which led to hypothesize a transient, "kiss-and-run" mechanism (Eskes et al., 2000; Wei et al., 2000; Lovell et al., 2008; Dai et al., 2011). However, new lines of evidence in NMR experiments support a direct physical interaction between Bax or Bak and the BH3-domains of Bid or Bim (Gavathiotis et al., 2008; Moldoveanu et al., 2013; Czabotar et al., 2013).

Indirect model

This model, also known as "de-repression model" postulates that the effectors are constitutively active, but bound to the anti-apoptotic homologs to stay inhibited. Upon cell stress, the BH3-only proteins displace and neutralize the anti-apoptotic proteins and free Bax and Bak to exert their pro-death function (Willis et al., 2005, 2007). Among the pool of BH3-only members, only Bid, Bim and Puma can interact with all the Bcl-2 type proteins, being also the most powerful killers, whereas the rest have unequal binding affinities. For example, Bad only binds to Bcl-2, Bcl-xL and Bcl-w; and Noxa to Mcl-1 and A1 (Chen et al., 2005). However, more proofs are still needed to assert that Bax and Bak are instrinsically active and this model fails to explain why *in vivo* only a portion of Bax and Bak are sequestered by the anti-apoptotic homologs.

Membrane embedded model

The previously described models propose irreversible protein-protein interactions and do not pay attention to the role of the membrane in Bcl-2 interactions and functions. The "embedded together" model, which combines the direct and indirect models, recognizes that the conformational changes in most of the Bcl-2 members upon membrane insertion affect considerably their

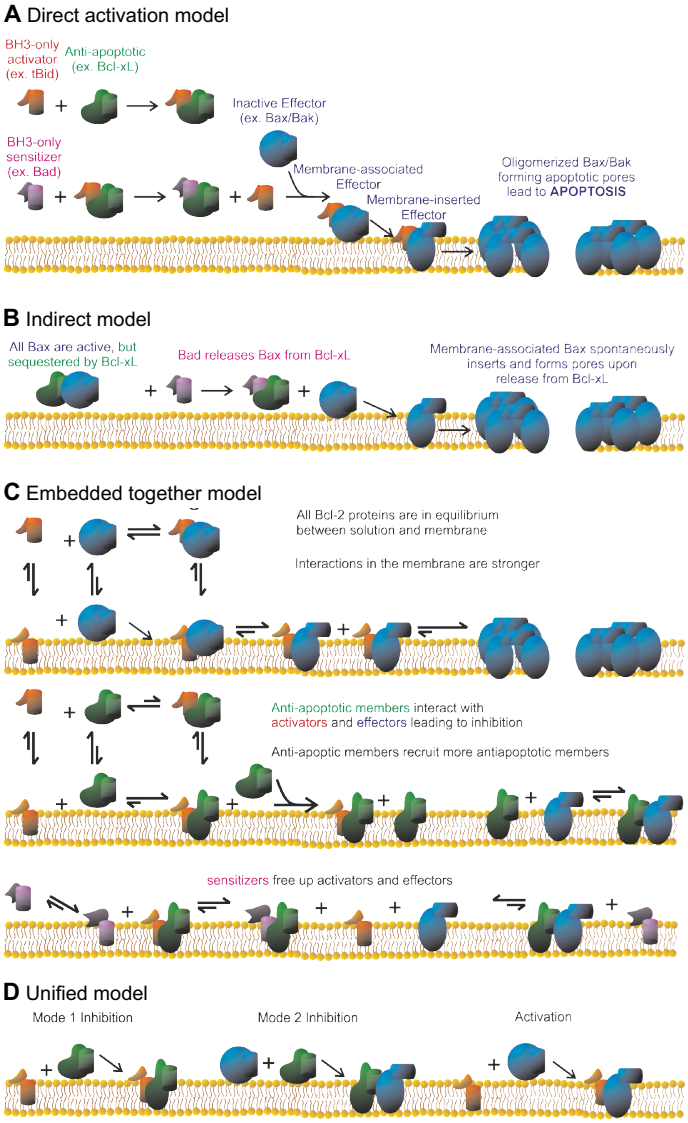

Figure 2.4. Models for the regulation of apoptosis by Bcl-2 proteins.

binding patterns and in turn the global regulation of MOM permeabilization (Leber et al., 2007; Lovell et al., 2008).

In this case, BH3-only proteins can spontaneously bind to membranes and they directly activate Bax/Bak or sequester anti-apoptotic proteins to hinder their prosurvival function. In general, the Bcl-2 proteins would exist in an equilibrium between the cytosol and the membrane until the point of no return in MOM permeabilization is reached, defined by Bax and Bak insertion and oligomerization. Therefore, in this scenario, the membrane becomes a regulating parameter for the interaction of all the functional Bcl-2 groups. The active role of the membrane has been embodied by advanced fluorescence microscopy for Bcl-xL-tBid and Bax-tBid association (García-Sáez et al., 2009; Liu et al., 2012). Moreover, only the membrane-bound conformation of Bax is active and able to oligomerize (Annis et al., 2005;

Bleicken et al., 2013). Importantly, additional mitochondrial membrane proteins not related to the Bcl-2 family can play a regulatory role at the membrane level: Mtch2 facilitates the recruitment of tBid to mitochondria (Zaltsman et al., 2010; Shamas-Din et al., 2011) and Drp1 can enhance Bax pore forming activity (Montessuit et al., 2010).

Unified model

As an extension of the "embedded together" model, the unified model specifically accounts for the relative affinities of anti-apoptotic Bcl-2 proteins for BH-3 only activators (Mode1) and for the effectors Bax and Bak (Mode 2). This model also connects the inhibitor effect of anti-apoptotic proteins with the role of mitochondrial dynamics in apoptosis regulation. Some anti-apoptotic members would inhibit only through Mode 1 (Bcl-2) or Mode 2 (Mcl-1), and some through both (Bcl-xL). Although both modes block membrane permeabilization, the unified model postulates that preventing Bax or Bak homo-oligomerization directly seems more efficient than doing it by a detour through inhibition of BH3-activators (Llambi et al., 2011).

Last but not least, the MOM lipid composition cannot be left aside when talking about the Bcl-2 network connections during apoptosis. Mitochondrial lipids such as cardiolipin can influence Bax activity by binding to cBid (Terrones et al., 2004) and they favor alterations in the bilayer properties related to its remodeling and permeabilization (Unsay et al., 2013).

2.2.4. It is all about the pore

Following an apoptotic insult, both Bax and Bak insert extensively in the MOM, where they oligomerize and arrange in clusters that ultimately trigger MOM permeabilization (Lovell et al., 2008; Eskes et al., 2000; Korsmeyer et al., 2000). Despite intense research, the molecular mechanisms underlying this process are still unsettled.

The early view of the apoptotic pore considered Bax and Bak as regulators of endogenous mitochondrial channels. Through physical interactions, Bax and Bak would induce the opening of a permeability transition pore (mPTP) located at mitochondrial contact sites, enabling the free flux of ions and water into the matrix and the rupture of the MOM (Narita et al., 1998; Brenner and Grimm, 2006). However, several arguments against the mPTP hypothesis have arisen. For instance, genetic studies have challenged the need of such components for apoptotic progression (Baines et al., 2005, 2007; Nakagawa et al., 2006) and the resulting cell death appearance via transition pores differs considerably from the classical apoptotic morphology (Nakagawa et al., 2006; Tsujimoto, Nakagawa, and Shimizu, Tsujimoto et al.). Moreover, Bax/Bak double knock-out cells fail to die by many apoptotic stimuli of the mitochondrial pathway, so they are essential for pore formation (Wei et al., 2001).

To date, the most accepted model involves the formation of pores at the MOM that allow cyt c and the other apoptotic factors to go through. This is mostly based on the structural resemblance of the Bcl-2 homologs to bacterial pore-forming toxins (Suzuki et al., 2000) and on the pore activity detected for Bax and Bak in vitro using artificial model membranes in the absence of any other mitochondrial components (Martinez-Caballero et al., 2009; Basañez et al., 2002; Antonsson, 1997). However, the exact nature of the apoptotic pore is not free of controversy. Some groups support a pore fromed exclusively by proteins, while others are in favor of a proteolipidic pore.

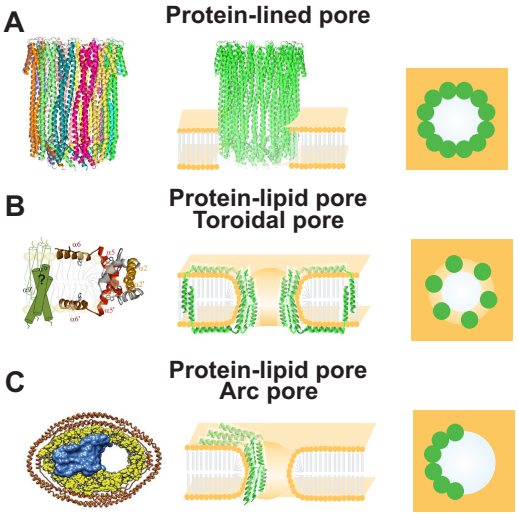

Figure 2.5. Pore formation models for Bax. Left pannels show representative pore forming protein structures. Middle pannels show a side view cartoon of the pore and right panels show the top view graphical representation. (A) Barrel-state pore model formed by ClyA (PDB:2WCD). (B) Toroidal pore. Clamp model proposed for Bax pore. (C) Arc pore. Pore formed by Bax monomers in lipid nanodiscs. Adapted from (Cosentino et al., 2015)

Proteinaceous channel

The idea of a purely proteinaceous Bax an Bak channel was taken from the beta-barrel pores formed by some toxins. Bax was postulated to create a Mitochondrial Apoptosis-induced Channel constisting of up to 9 Bax molecules (Martinez-Caballero et al., 2009) and a size ranging from 3 to 8 nm. This barrel-stave channel would allow to release proteins up to 17 kDa, but it is not permeable to bigger Dextrans (Dejean et al., 2010). An alternative study showed that a tetrameric Bax channel is enough to release cyt c from liposomoes (Saito et al., 2000), but none of these models is able to justify the release of proteins of various sizes suggested for Bax-mediated MOM pores.

Proteolipidic pore

Current research appears to validate that Bax and Bak activity fits best with the formation of mixed protein/lipid structures known as toroidal pores (Qian et al., 2008), which are long-lived and large enough to release high molecular weight molecules (Bleicken et al., 2013).

Toroidal pores avoid the high energetic cost of exposing their hydrophobic helices to the aqueous environment by lipid bending and formation of a highly curved, non-bilayer structure at the pore edge (García-Sáez, 2012) (Fig. 2.5). In agreement with this, Bax can induce the redistribution of lipids in liposomes and its central helix $\alpha 5$ is able to decrease the line tension at the pore edge (Terrones et al., 2004; García-Sáez et al., 2007). The size of Bax pores is tunable and can be regulated by protein density on the membrane, indicating the ability of Bax to form relatively flexible structures of different dimensions (Bleicken et al., 2013).

Recent structural studies have shown that active, full-length membrane-embedded Bax arranges into symmetric dimers, which serve as building blocks for the complex aggregates that mediate membrane disruption (Bleicken et al., 2014; Subburaj et al., 2015). These structural data suggest that the stabilization of the toroidal pore is accomplished by the Bax dimer lining the highly curved lipid structure thanks to an opening of the hairpin between helices α5-α6 in a suitable angle to clamp the membrane (Bleicken et al., 2014). This property inherent to Bax should not be underestimated, since it can be important for Bax interplay in other cellular processes such as mitochondrial morphology (see section 2.2.5)

Strikingly, very recent work envisions another kind of protein–lipid pore structure for Bax, where the protein forms an arc on one side of the pore, and the lipids complete the toroidal structure (Xu et al., 2013; Salvador-Gallego et al., 2016). The arc model has been postulated for multiple pore-forming proteins like perforins or cholesterol-dependent cytolysins (Gilbert et al., 2014; Leung et al., 2014; Metkar et al., 2015; Sonnen et al., 2014; Stewart et al., 2015). So far, membrane perforation by this type of conformation had only been proposed for β pore-forming toxins, but lipid pores containing only one active Bax molecule have been recently visualized in lipid nanodiscs, which strongly support the toroidal pore model for Bax function (Xu et al., 2013).

Accordingly, superresolution microscopy has revealed arc-shaped Bax assemblies in mammalian cells, which are enough to perforate the membrane of lipid bilayers, as seen by AFM (Salvador-Gallego et al., 2016). Thus, it could be hypothesized that the toroidal conformation of the lipids in the arc pore architecture may be an intermediate stage during the assembly of full ring protein-lined pores.

2.2.5. Apoptosis and mitochondrial dynamics walk hand-in-hand

At this point, we are convinced that mitochondria not only play a major role in providing energy to the cell, but are also crucial for a number of cellular processes including calcium homeostasis and lipid metabolism. Importantly, these cellular organelles also constitute the main check-point of the apoptotic cascade.

In contrast to the classical view of the organelle found in textbooks, live cell microscopy has revealed that mitochondria form a dynamic tubular network that is continuously fusing and dividing. The balance between these two processes is known as mitochondrial dynamics and is essential to maintain a functional organelle with proper shape. Indeed, aberrant mitochondrial fusion and fission are tightly linked to a wide range of disorders, like premature aging, neurodegenerative diseases, or cancer (Friedman and Nunnari, 2014). The main regulators of mitochondrial dynamics are a group of large dynamin-related GTPases (DRPs). Mitochondrial fusion requires integral outer and inner membrane DRPs, named mitofusins and OPA1. In vertebrates, mitofusin proteins (Mfn1 and Mfn2) reside in the MOM and regulate its fusion (Legros et al., 2002; Chen et al., 2003), whereas OPA1 is responsible for MIM fusion and cristae remodeling (Cipolat et al., 2004; Frezza et al., 2006). These proteins self assemble in order to control membrane remodeling and lipid mixing.

Mitochondrial division is catalyzed by the Dynamin-related protein 1 (Drp1 in mammals and Dnm1 in yeast), a predominantly cytosolic DRP which drives back and forth to the MOM in healthy cells when required for mitochondrial fission. In order to exert its function, Drp1 is believed to oligomerize into helical structures that embrace and constrict mitochondria until the complete fission of the outer and inner membranes is achieved (Bleazard et al., 1999; Smirnova et al., 2001).

During apoptosis, the interconnected mitochondrial network disintegrates, yielding smaller punctiform organelles. There is overwhelming evidence corroborating the notion that mitochondrial dynamics can be regulated by some apoptosis-related proteins, strongly supporting a tight link between the two processes (Ugarte-Uribe and García-Sáez, 2014; Martinou and Youle, 2011).

Under normal growth conditions, Bax and Bak are required for the usual rate of mitochondrial fusion and both can activate Mfn2, leading to the assembly of progressive fusion sites (Karbowski et al., 2006). Along these lines, in vitro studies showed that only the soluble, monomeric state of Bax favors fusion, mainly when it is mediated by Mfn2-Mfn2 complexes. However, this stimulation is blocked by the gathering of membrane-inserted, oligomerized Bax (Hoppins et al., 2011). The anti-apototic protein Bcl-xL also plays a housekeeping role in the regulation mitochondrial dynamics. In neurons, Bcl-xL contributes to an increase in the mitochondrial biomass

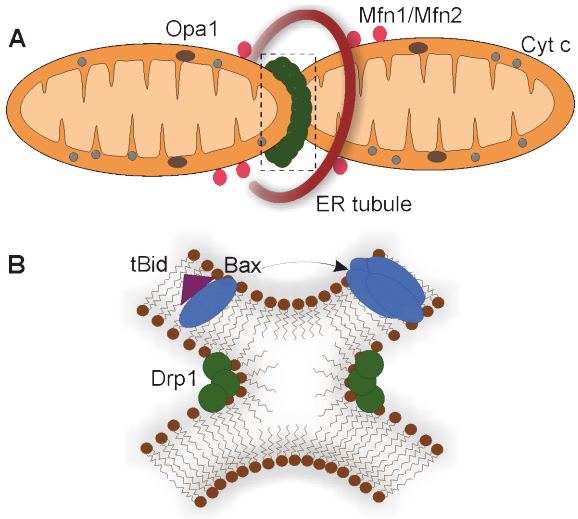

Figure 2.6. Interplay between Bcl-2 proteins and mitochondrial dynamics. (A) During apoptosis, Drp1 is recruited to mitochondrial foci to mediate mitochondrial constriction and fission. (B) Model explaining the role of mitochondrial membrane hemifission or hemifusion intermediates in Bax oligomerization. During apoptosis, Bax is recruited to the outer mitochondrial membrane by tBid (or other BH3 only proteins) where it inserts. At the same time, Drp1 constricts the organelle, triggering the formation of a hemifission intermediate that would help Bax oligomerization.

and in the fusion/fission events. Moreover, it enhances the GTPase activity of Drp1 and induces Drp1-dependent synapse formation (Li et al., 2008; Berman et al., 2009).

During apoptosis, active Bax and Bak accumulate in specific foci where mitochondrial fission takes place, colocalizing with Drp1 and Mfn2 (Karbowski et al., 2002) (Fig. 2.6). Indeed, Drp1 stably oligomerizes in these sites through SUMOylation in a Bax/Bak-dependent manner (Wasiak et al., 2007). Although the mechanistic link between Drp1 and Bax or Bak remains vague, a recent study argues that SUMOylation of Drp1 by the protein MAPL at the ER/mitochondria contact sites stabilizes a signaling platform downstream of Bax/Bak activation, required for efficient cyt c release (Prudent et al., 2015). Drp1 can also form hemifusion intermediates in liposomes that stimulate tBid-induced Bax oligomerization and cyt c release (Montessuit et al., 2010). Such non-bilayer structures could be formed in cardiolipin-enriched sites, and probably directly affect the integrity of the MOM by lowering the energy required for toroidal pore formation and stabilization, providing another link for mitochondria permeabilization and mitochondria fragmentation (Martinou and Youle, 2011). This connection was confirmed by a study that shows that the mitochondrial network shape strongly dictates the successful coordination of a subset of BH3-only members to promote Bax-induced MOM permeabilization and apoptosis (Renault et al., 2015). Besides Drp1, the literature has documented a wide range of mitochondrial morphogenesis

proteins that are also involved in apoptosis regulation (Table 2.1)

Gene product	Process	Loc.alization	Loss-of-function phenotype	Apoptosis regulation	References
Opa 1	Fusion	MIM	Fragmented mitochondria. Decrease in ATP production, potential and oxygen consumption.	Downregulation sensitizes cells to apoptosis. Remodeling of mitochondrial cristae during apoptosis.	Cipolat et al. (2006) Scorrano et al. (2002) Frezza et al. (2006)
Mitofusins (Mfn1 and Mfn2)	Fusion	MOM	Fragmented mitochondria. Changes in potential. Decline in mitochondrial function. Developmental defects.	Downregulation sensitizes cells to apoptosis. Overexpression delays apoptosis and inhibits Bax oligomerization. Interactions with Bax and Bak.	Brooks and Dong (2007) Karbowski et al. (2006)
Drp1	Fission	MOM, peroxisomes, cytosol	Elongated mitochondria and peroxisomes	Downregulation, or inhibition delays apoptosis and cyt c release. Interactions with Bcl-xL. Stabilized on mitochondria in a Bax/Bak dependent manner.	Li et al. (2008) Frank et al. (2001) Montessuit et al. (2010)
Fis1	Fission	MOM and peroxisomes	Elongated mitochondria	Downregulation delays apoptosis, overexpression induces cell death. Molecular interactions with Bcl-xL.	James et al. (2003) Lee et al. (2004)
Mff	Fission	MOM and peroxisomes	Elongated mitochondria	Downregulation delays apoptosis.	Gandre-Babbe and van der Bliek (2008) Otera et al. (2010)
MID49 MID51	Fission Fusion	MOM	Elongated or fragmented mitochondria	Binding and inhibition of Drp1. Depending on the stimulus, stimulation of fission.	Xu et al. (2016) Palmer et al. (2013)
Mitofilin	Cristae structure	MIM	Defective cristae	Downregulation induces apoptosis.	Yang et al. (2012)
PARL	Cristae structure (processing of Opa1)	MIM	Defective cristae	Loss of expression induces apoptosis.	Cipolat et al. (2006)

Table 2.1. Proteins implicated in regulation of mitochondrial dynamics and apoptosis. Adapted from (Karbowski, 2010)

3 Microscopy techniques

3.1. Fundamentals of light microscopy

Back in the 16th century, curious spectacle-makers realized that an image could be greatly magnified by using two or more lenses inside a tube. They had just invented the first compound microscope. Years later, Robert Hooke published his acclaimed microscope-based work "Micrographia", where he used the word "cell" for the first time in a biological context. For his studies, he used a simple, single lens microscope illuminated by a candle, most likely giving birth to the first light microscope. This technique was also chosen by his colleague van Leeuwenhoek, who polished the device and grabbed the attention of biologists with his images. It took a long time until the compound microscopes could provide the same image quality as single light microscopes, due to difficulties in solving spherical and chromatic aberrations. With his theory for the resolving power of the microscope, Ernest Abbe introduced the term Numerical Aperture (mathematical calculation of the light-gathering capabilities of a lens) and clarified the differences between resolution and magnification. Resolution is the ability to distinguish two bright objects very closely located while magnification refers to the number of times an image is enlarged. Abbe's diffraction equation demonstrates that the higher the numerical aperture and the shorter the wavelength, the better resolution is achieved (Eq. 3.1).

$$d = \frac{\lambda}{2n \sin \alpha} = \frac{\lambda}{2NA} \tag{3.1}$$

These findings, together with the implementation of Köhler Illumination, which produces a bright, uniform lighting of the specimen, brought light microscopy to a new level. It is important to note, that according to Abbe's equation, the maximum resolution of a light microscope is around 200 nm, and the pattern of light emitted by the smallest possible fluorescent point is actually a diffraction limited spot called point spread function (PSF). Nowadays, microscope imaging has managed to go beyond this diffraction limit, as we will discuss later.

3.2. Fluorescence microscopy

Fluorescence is the ability of certain molecules to absorb light at specific wavelengths, which brings them to an excited electronic state, and to emit

light of longer wavelengths as they return to the ground state after a short delay, called fluorescence lifetime. After Stokes identified this wavelength shift between absorbed and emitted photons, it turned out that many specimens such us crystals, vitamins, and inorganic compounds could fluoresce when irradiated with the proper light. This properties gave rise to the development of a broad spectrum of fluorophores that enabled one to specifically stain and observe intracellular components simultaneously in a non-destructive manner (Lichtman and Conchello, 2005; Giepmans et al., 2006).

In a widefield fluorescence microscope, the sample is illuminated through the objective lens with a high-intensity excitation light reflected from the surface of a dichroic mirror. The fluorescence emitted by the specimen passes back through the mirror and is focused to the detector through the same objective. Selective spectral emission filters separate the illumination light from the emitted fluorescence and an additional excitation filter blocks the unwanted excitation wavelengths, therefore increasing the signal to noise ratio. The image is brought into focus for the eye by the ocular lens or digitally by charged-coupled device (CCD) cameras (Combs, 2010). The main components of a fluorescence microscope are illustrated in Fig. 3.1.

Fluorescence microscopy has become a powerful tool to observe individual organelles and macromolecular complexes simultaneously with different colors, as well as to follow several pathways and dynamics in living cells that would otherwise be unreachable (Lichtman and Conchello, 2005; Bacia and Schwille, 2007). The final resolution is governed by the wavelength of light, the objective lens, and the properties of the specimen itself. As a result, the basic design of optical microscopes has not changed much since its origins. However, the technique now has a much higher level of sophistication due to a significant improvement in sample contrast and resolution.

3.2.1. Confocal microscopy

Confocal microscopy stands out over conventional widefield microscopy in the way that it allows the elimination of out-of-focus glare, to collect several thin optical sections from thick samples, and to improve the axial and lateral resolution.

In contrast to the mercury or xenon lamps used standard widefield illumination, in a confocal microscope the specimen is scanned point by point (PSF by PSF) by a laser beam to build the images. The emitted fluorescence is then directed back to reach light sensing detectors such as photomultipliers (PMTs). An aperture (pinhole) inserted in front of the detector, in the conjugated focal plane to the point of focus in the sample, acts as a barrier for the out-of-focus light. The pinhole size can be modulated, allowing more or less light to arrive to the detector and enabling high contrasted, tunable, optical sectioning. The laser beam intensity and wavelength are regulated by an AOTF (Acousto-Optical Tunable Filter) and in some models a separation of the visible spectrum wavelengths is achieved by a diffraction grating or

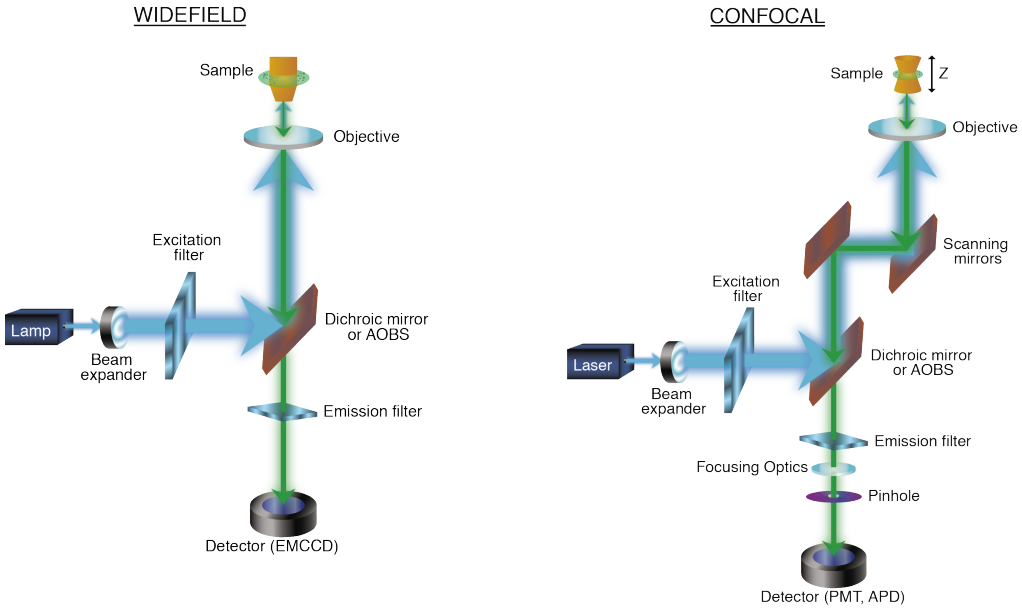

Figure 3.1. Differences between Widefield and Confocal microscopes. In confocal microscopy (B) the concept of illuminating the sample with excitation light (e.g., blue light) and the sample emitting light with a longer wavelength (e.g., green light) is identical to the general principles of fluorescence in wide field microscopy (A). The differences to wide field microscopy are: (i) the excitation laser light is scanned over the sample and the emitted light originates from this area; (ii) on the detection beam path a pinhole aperture in front of the detector prevents light emitted from above or below the focal plane (dotted lines) from reaching the detector; and (iii) because only light from the focal plane (solid line) reaches the detector an optical section is generated.

by a prism located in the light path before the detectors (Combs, 2010) (Fig. 3.1).

Even though it is an outstanding technique for biological applications, Laser Scanning Confocal Microscopy has some limitations. It is in general a rather slow process, so that in new spinning-disk confocal microscopes the single pinhole is replaced by a spinning disk with multiple tiny apertures that are scanned simultaneously. This increases temporal resolution but impairs spatial resolution. In addition, visible linear wavelengths have a low penetration depth in living tissues. This drawback is overcome with two-photon laser scanning microscopes, which in addition detect scattered photons and minimize the overall toxicity while imaging.

3.2.2. Fluorescence Correlation Spectroscopy (FCS)

Fluorescence correlation spectroscopy (FCS) is a powerful technique with high spatiotemporal resolution to quantitatively determine the concentration, diffusion properties and interactions of fluorescent molecules with single molecule sensitivity. The most common implementation of FCS uses a

confocal microscope to detect fluctuations of single molecules in a tiny, sub-femtoliter detection volume, whose size depends on the pinhole aperture, the intensity of the laser beam, and the light wavelength. Such fluorescent fluctuations mostly rely upon the fluorophore's mobility, but are also affected by its photophysical properties, concentrations and brightness (Ries et al., 2012).

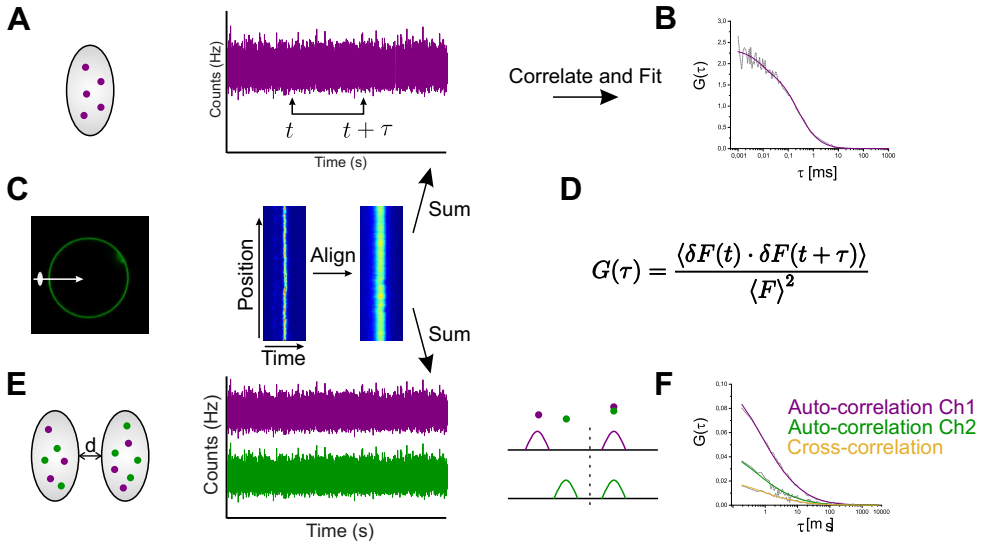

Figure 3.2. FCS principle. (A) Fluorescence molecules diffusing through the detection volume produce intensity fluctuations. (B) The fluctuations are temporally autocorrelated to measure the self-similarity of the signal over time and fitted with a model function. (C) In scanning FCS, the detection volume is scanned through the membrane. The line scans are arranged and aligned to correct for membrane movements. For each line scan, the detected photons are summed up to create a fluorescence intensity trace, which is auto-correlated and fitted with diffusion models. (D) Expression used to calculate the temporal autocorrelation analysis. G is the autocorrelation function, F is the fluorescence intensity as a function of time t, and τ is the correlation time. (E) Two focus dual-color FCS: fluorescence molecules differently labeled diffuse through two detection volumes separated by a known distance d. If the two molecules bind and co-difuse, there will be a correlation between the green and magenta intensities, leading to a positive cross-correlation amplitude (F)

To perform FCS, PMT detectors are replaced by highly sensitive avalanche photo diodes (APDs), which detetect the fluorescence as a stream of single photon arrival times, which constitute the raw data. These times are used to calculate the fluctuating intensity of fluorescence, which is then analyzed by applying the temporal autocorrelation of the recorded intensity signal. The autocorrelation analysis is a mathematical tool that measures the self-similarity of the signal with time, reflecting the probability that the signal at different times still belongs to the same molecular event.

In order to calculate the parameters of interest, the measured correlation curve is then fitted with a mathematical function that models the origin of

the fluorescence fluctuations inside the detection volume, according to the characteristics of the system under investigation (Fig. 3.2). The parameters that are considered in this model are usually the size and shape of the detection volume, the brightness and concentration of the fluorophore, and other photophysical phenomena generating additional fluctuations (e.g. triplet, blinking). The result is an autocorrelation curve whose decay reflects the residence time of the molecules in the detection volume (Fig. 3.3) and whose amplitude is inversely proportional to the number of observed molecules and thus to the concentration of fluorescent particles (Ries and Schwille, 2006; Subburaj et al., 2013).

Some variations of FCS have been introduced that enable the application of this technique to a broader range of biological systems, specially membranes:

- Fluorescence cross-correlation spectroscopy (FCCS): Allows for the measurement of interactions between molecules labeled with different fluorophores that diffuse together through the focal volume by temporally correlating two or more fluorescence channels.

- Scanning FCS (line, linear, circular): Allows for the study of slow diffusing species typical of lipid membranes. The detection volume is scanned through the sample so the residence time of the fluorophore in it is much smaller, thus decreasing the probability of photobleaching (Ries and Schwille, 2006).

- Two focus FCS: Provides a calibration free method, since it measures the intensity fluctuations from two partially overlapping foci that are separated by a known distance. Taking the distance between two volumes as a reference avoids errors in observation volume calibration when using samples with a refractive index mismatch (Fig. 3.2e,f).

- Z-scan FCS: The focal volume is placed at different positions along the z-axis, making it possible to measure above, below and at the membrane.

In conclusion, FCS is an excellent approach to investigate dynamic processes, due to the ability to measure diffusion coefficients, fluorophore concentrations, particle sizes, chemical reactions, conformational changes, and binding/unbinding processes. Moreover, the combination of this technique with many different imaging methods, such as laser scanning confocal microscopy, two-photon microscopy, total internal reflection fluorescence microscopy, STED, and others, has made it highly advantageous for cell biology (Bacia et al., 2014).

3.2.3. Other confocal-based techniques

Improvements in microscopy techniques and the development of new fluorescent proteins have opened the door to confocal-based approaches for

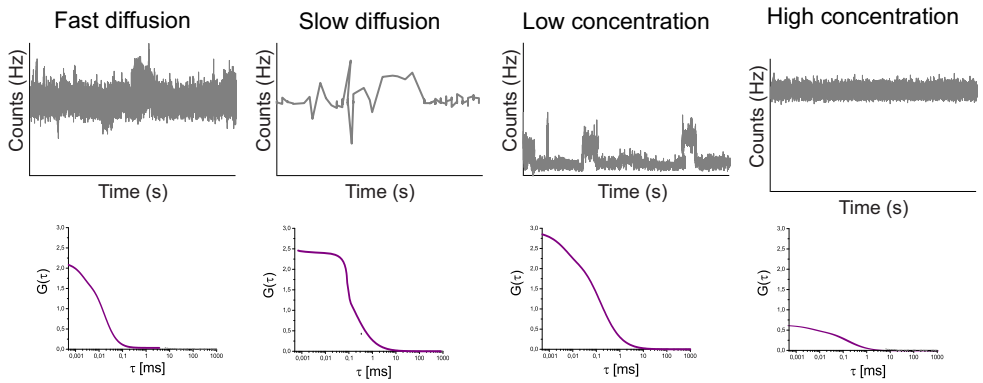

Figure 3.3. FCS autocorrelation curve: dependence on concentration and diffusion of the fluorescent molecules. Fast diffusion results in fast intensity fluctuations and a decay of the autocorrelation curve at smaller lag times τ. If the concentration of molecules is low, the amplitude of the autocorrelation curve is higher and the intensity fluctuations larger.

the research of the interactions and dynamic processes that govern the organization and structure of living cells. Among them, we can highlight Fluorescence recovery after photobleaching (FRAP), Forster resonance energy transfer (FRET) and Fluorescence-lifetime imaging microscopy (FLIM) (Ishikawa-Ankerhold et al., 2012).

The basic principle of FRAP is to photobleach a small region within a fluorescently labeled membrane and record the time necessary for the bleached region to recover. It was first described in the 1970s as a tool to follow protein or lipid mobility on the cell-surface, but its applications have been extended to the study of lipid fluctuations, vesicle transport, or cell adhesion, among others (Wong and Wessel, 2008; Zhang et al., 2010). Variations of this technique include FLIP (fluorescence loss in photobleaching), photoconversion, or photoactivation.

FRET serves to discern interactions in the nanometer range between proteins tagged with spectrally different fluorophores. It is based on the non-radiative energy transfer from an excited donor molecule to an acceptor molecule. In turn, the acceptor emits a fluorescence photon and the fluorescence lifetime of the donor molecule decreases. In this way, the interaction between both molecules is calculated by determining the efficiency of the transfer, which is inversely proportional to the sixth power of the distance between donor and acceptor. FRET requires an overlap of the emission spectrum of the donor with the excitation spectrum of the acceptor, and a favorable orientation of the dipoles.

In FLIM, the fluorescence lifetime, rather than the emission spectra, is used to create the image. When an excited fluorophore returns to the ground state, it can do so by emitting a fluorescence photon, converting the energy internally, or transferring the energy to the environment. The environment can affect how long the fluorophore stays in the excited state before emitting the photon to relax, resulting in a decay in the fluorescence lifetime. This

decay measured in FLIM mostly depends on the ion concentration, oxigen, pH, or protein binding. (Ishikawa-Ankerhold et al., 2012).

The combination of FLIM and FRET provides great advantages, such as internal calibration and increase in spatio-temporal resolution (Sun et al., 2011; Wallrabe and Periasamy, 2005). In FLIM-FRET, the donor lifetime is measured in presence and absence of the acceptor. Since the fluorescence lifetime is an inherent property of the dye and it does not depend on the intensity, this technique allows to better estimate the distance between the labeled proteins regardless of the possible intensity artifacts due to expression level variations or external effects (Sun et al., 2011; Wallrabe and Periasamy, 2005).

Useful terms in microscopy

Magnification: Ability to enlarge an image produced by an optical system in comparitson to its true size.

Resolution: Smallest distance apart at which two points can be seen separatelly.

Stoke's shift: Difference in wavelegth between the maxima of the absorpbtion and emission spectra of a fluorophore.

Numerical aperture (N.A.): Dimensionless number that characterizes the lens opening angle and measures the objective's resolving power and the brightness of the image.

Point Spread Function (PSF): 3D diffraction pattern resulting from the image of a single point object by an objective lens.

Airy disc: Central difraction maximum of the cross-section of a perfectly focused spot (cross-section of the PSF). 1 Airy unit is referred to the pinhole diameter that gives the maximum theoretical signal.

Gain: Detector's sesitivity (voltage). It adjusts the signal amplification at the detector.

Offset: Minimal signal intensity detected by the sensor. It adjusts the background level.

Photobleaching: Irreversible destruction of a fluorophore

Blinking: Random fluorescence intermittency of a fluorophore between ON and OFF states.

3.2.4. Super-resolution microscopy

There is no doubt about the potential of the fluorescence microscopy techniques explained above in biology, but one issue is that the relevant size range of many cellular structures is much smaller than the presumed 200 nm driffaction barrier (Fig. 3.4). Lately, "super-resolution" techniques have circumvented this limitation to explore the cell's internal life and its processes with up to one magnitude higher in resolution (Mund et al., 2014). The great feat of bringing optical microscopy to the nanodimension was awarded with the Nobel Chemistry Prize recently.

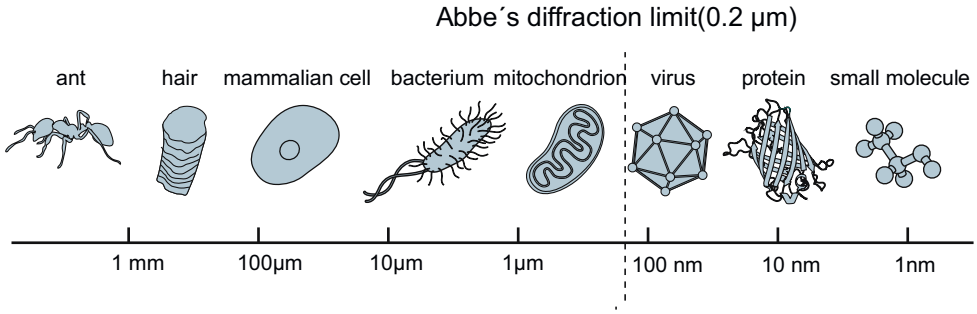

Figure 3.4. Representative sizes of microscopic samples. Illustration: © Johan Jarnestad/The Royal Swedish Academy of Sciences

Single-molecule Localization-based Microscopy

The term single molecule localization microscopy (SMLM) includes the super-resolution techniques based in the precise localization of isolated emitters, such as Photo-activated localization microscopy (PALM) (Betzig et al., 2006) and stochastic optical reconstruction microscopy (STORM) (Rust et al., 2006).

As previously mentioned, the width of the point spread function (PSF) limits resolution in optical microscopes. Nevertheless, the position of the point source is at the center of the spot and can be precisely estimated via centroid calculation or PSF fitting to a known geometrical function. This method is only reliable for isolated emitters. However, the imaging of dense biological samples produces generally many overlapping PSFs, so as to overcome this issue in SMLM controlled pulses of laser light separate the emitters over time. If only some fluorescent molecules are simultaneously active, their positions can be accurately discerned. Afterwards, those emitters are bleached or converted to a dark state and another set of fluorophores becomes activated. Iteration of this process for enough number of times ensures that all the flourescent molecules are eventually localized. A super-resolved 2D or 3D image is then reconstructed by superimpossing all the individual recordings. Therefore, the resolution of the final image is limited by the number of localizations and the localization precision, instead of by diffraction (Lakadamyali, 2014; Mund et al., 2014).

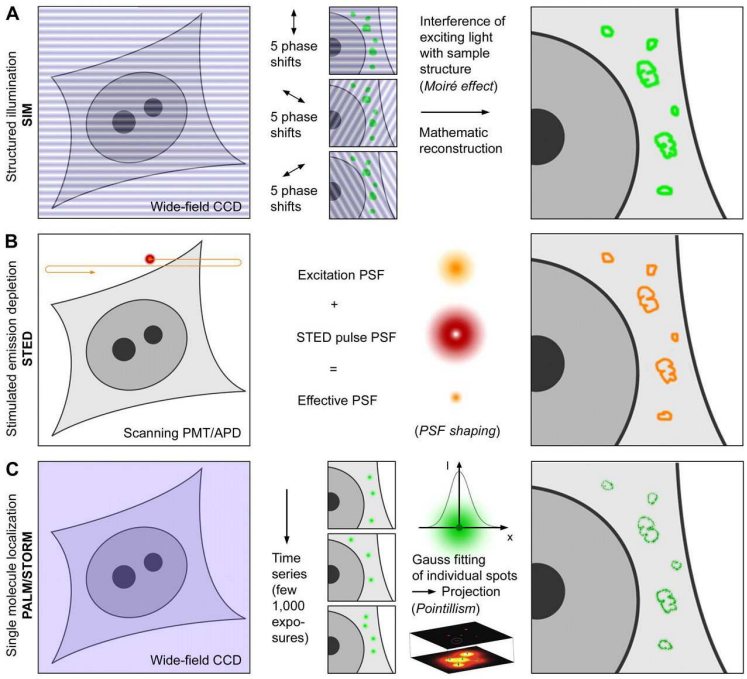

Figure 3.5. Super-resolution microscopy imaging principles. (A) In SIM the sample plane is excited by a nonuniform wide-field illumination. Laser light passes through an optical grating, which generates a stripe-shaped sinusoidal interference pattern. (B) In STED microscopy the focal plane is scanned with two overlapping laser beams. While the first laser excites the fluorophores, the second longer wavelength laser drives the fluorophores back to the ground state by the process of stimulated emission. (C) Single molecule localization microscopy assures that only a relatively low number of fluorophores are in the emitting (active) state. This is achieved either by photoactivation, photoswitching, triplet state shelving, or blinking. These molecules are detected on the CCD camera as diffraction-limited spots, whose lateral position is determined with very high accuracy by a fit. Schermelleh et al. (2010)

SMLM requires bright fluorophores which switch between "on" and "off" fluorescent states stochastically. In order to maximize resolution, the samples should also be densely labeled. A wide set of fluorophores have been optimized for the different SMLM methods, including photoactivable or photoswitchable FPs (PA-GFP, mMaple), organic dyes that can be switched under special buffer conditions (Alexa647, Cy5, CF680), or activator-photoswitacble dye-pairs (Cy3-Cy5) (Betzig et al., 2006; Heilemann et al., 2008; Rust et al., 2006). Due to the long measurements required for image acquisition, most of the localization-based investigation is performed with fixed samples. However, some research groups have taken the leap into live cell imaging (Huang et al., 2013; Shroff et al., 2008; Jones et al., 2011).

SMLM is admirably contributing to decipher the inner world of the cell. It has been a powerful tool to investigate the organization the cytoskeletal

structure (Xu et al., 2013), the endocytic machinery (Picco et al., 2015), the chromatin (Ricci et al., 2015), or the proteins that form the nuclear pore complex (Szymborska et al., 2013). This technique has also provided new insight into the proteins related to diseases like Huntington's or Alzheimer's (Ries et al., 2013; Duim et al., 2011).

Stimulated Emission Depletion Microscopy (STED)

In order to improve resolution, this technique exploits the non linear response of a fluorophore to its illumination by applying the principles of reversible saturable optical fluorescence transitions (RESOLFT) (Hell, 2003; Hofmann et al., 2005).

The STED approach is based on a confocal microscopy setup, but it uses two overlapping laser beams as the illumination source. The first one excites the fluorophores into a higher electronic state and the second, doughnut-shaped depletion beam (STED beam) quenches all the fluorescence except the one detected in the center of the doughnut. Once excited, the electrons are stimulated to emit a photon with the wavelength of the STED beam, but no fluorescence photon. This high intense depletion beam is red-shifted with respect to the excitation beam, allowing one to differentiate the two types of photons and to discard the stimulated ones. As a result, the fluorescence emission is confined to a sub-difraction limited spot, which improves the resolution. The scanning of the complete sample with these coupled lasers yields an image with a resolution better than Abbe's stipulated limit (Klar et al., 2000).

Although theoretically STED has no optical limit in resolution, in the practice the resolution is restricted by the photo-physical properties of the dyes (Jakobs, 2006; Hell, 2007). Apart from the commonly available FPs and organic dyes, better imaging is now possible thanks to quantum dots and tag-mediated labeling of fusion proteins with fluorescent molecules (Urban et al., 2011; Hanne et al., 2015). Since it was first develpoed, STED has been applied to the study of many proteins and processes at a sub-organelle level, such as mitochondrial proteins (Nienhaus and Nienhaus, 2015; Schmidt et al., 2009). Live cell STED has also allowed one to follow organelle dynamics (Hein et al., 2008; Westphal et al., 2008) and even image neurons in a living mouse at high resolution (Berning et al., 2012) .

(Saturated) Structured Illumination Microscopy—(S)SIM

SIM also uses two laser beams to excite the fluorophores in the specimen. However, instead of scanning the sample like in STED microscopy, SIM relies in the interference of the two beams to create periodic line patterns of bright and dark stripes. This sinusoidal illumination pattern has a peak intensity that does not result in fluorescent saturation, so the resolution can only be increased by a factor of two (Heintzmann and Cremer, 1999;

Gustafsson, 2000). However, SIM was proven very useful in live-cell imaging thanks to its low power illuminating source (Gustafsson, 2008).

In order to increase resolution, one can optically saturate the fluorescence markers in the sample to achieve a nonlinear response of the fluorescence signal (Gustafsson, 2005). The major drawback of (S)SIM is that the saturating excitation power causes extensive photodamage and reduced photostability of the fluorophores.

3.3. Labeling strategies

Fluorophores are molecules that emit fluorescent light when excited and have characteristic spectra, light absorbance efficiency, fluorescence lifetime, quantum yield, and photobleaching properties. Some approaches to obtain fluorescent samples for imaging are listed below.

Dyes

Synthetic dyes are bright and photostable and have engineered reactive groups which allow for their attachment to the biological molecules of interest (e.g. Xanthene, Cyanine, Alexa or Atto dyes).

Some of them are instrinsically fluorescent and have very specific binding properties, such as the DAPI or Hoechst nucleic acid stain, the mammalian actin fibre dye phallodin, or the anterograde neuron stain DiI. Since they change their fluorescent properties when bound to different amounts of molecules, they can be used directly in live cells (Progatzky et al., 2013).

Other synthetic fluorophores require a transportation system such an antibody that binds a specific target within the cell. These are used in immunofluorescence of fixed samples, where they are conjugated to a primary antibody or to a secondary antibody that binds to the primary, which recognizes a determined antigen (Hilderbrand, 2010).

Quantum dots

Quantum dots are nanometer-sized particules of purified semiconductors that exhibit long-term photo-stability as well as bright emission. They can be excited by wavelengths up to the blue range and their emission wavelength increases with the diameter (from 3 to 10 nm) (Reed et al., 1988). These dots are usually coated with an additional semiconductor shell and a polymer to enable coupling to proteins, oligonucleotides, or small molecules which then bind to the target. Due to their flexible capabilities, they can also be used for direct staining of cells (Hoshino et al., 2012).

Fluorescent proteins (FP)

Fluorescent proteins (FP) are genetically encoded fluorophores that constitute non-invasive markers for cells and do not need exogenous substrates

or co-factors to stain their target. A reporter gene encoding the FP is introduced into living organisms through cell transfection or injection with viral vectors in order to visualize the localization of the gene product. The first FP found was GFP, in the jellyfish *Aequorea victoria* (Shimomura et al., 1962; Ormö et al., 1996). The color palette has now been extended with the identification of FP from other species (e.g. dsRed or Kaede) and improved variants have been developed by mutagenesis techniques (Shaner et al., 2005). Interestingly, the photoactivable and photoconvertible fluorescent proteins, which undergo specific changes in their spectral properties after activation with laser light of determined wavelength and intensity, have become particularly useful for the study of organelle dynamics (Lippincott-Schwartz et al., 2003; Chudakov et al., 2004).

4 Aims

Apoptosis is essential to human development. The malfunctioning of this process can lead to the progression of autoimmune diseases or cancer. Therefore, the regulation of apoptosis is a fundamental question in biology. The point of no return in a cell's commitment to die by apoptosis is the permeabilization of the MOM, mediated in the last instance by the pro-apoptotic protein Bax. However, the molecular mechanisms underlying this process, as well as the supra-molecular arrangement of Bax in mitochondria remain enigmatic. In order to gain insight into Bax organization, and its relationship with MOM permeabilization and mitochondrial dynamics, the following objectives were proposed:

1. Elucidation of Bax assembly during apopotosis at the nanoscale using fluorescence super-resolution microscopy.

2. Determination of Bax orientation on mitochondria via dual-color super-resolution microscopy and characterization of Bax pores *in vitro* with atomic force microscopy.

3. Characterization of Bax influence in the mitochondrial fragmentation machinery by investigating its interplay with Drp1.

Part II.

Experimental procedures

5 Materials

5.1. Buffers

Anode I
0.3 M Tris 10%
Methanol pH 10.4

Anode II
25 mM Tris
10% methanol

Cathode
25 mM Tris
40 mM glycin
10% methanol pH 9.4

GTPase
20 mM HEPES pH 7.4
150 mM KCl
2 mM MgCl2

Imaging
50 mM Tris/HCl pH 8
10 mM NaCl
10% (v/w) glucose
35 mM cysteamine (MEA)
0.5 mg/mL glucose oxidase
40 μg/ml catalase

Laemmli 6x
4% SDS
10%
ß-mercaptoethanol
20% glycerol
0.004% bromophenol
blue
0.125 M Tris HCl

Lysis
10 mM Tris/HCl pH 8
150 mM NaCl
1 mM EDTA
1% NP40
0.1% SDS

MB
210 mM mannitol
70 mM sucrose
1 mM EDTA
10 mM Hepes pH 7.4

SDS Running
25 mM Tris
190 mM glycine
0.1% SDS

SLB
150 mM NaCl
10 mM HEPES pH 7.4

TBS-T
40 mM Tris
5 mM sodium acetate
1 mM EDTA
20 mM Tris/HCl
135 mM NaCl
1 M HCl pH 7.6
0.1% Tween 20

TAE 1X
40mM TRIS
20mM acetic acid
1mM EDTA.

5.2. Cell culture volumes

The transfection volumes are shown per well and the OptiMEM volume refers to the total quantity.

Vessel	Seeding density	Growth medium (ml)	DNA(μg)	Lipofectamine 2000 (μl)	OptiMEM (ml)
8-well μ-chamber	0.5-0.8·10^5	0.25	0.1-0.2	0.25	0.05
6-well plate	1-2·10^5	2	0.3-0.6	1-1.5	0.2
10 cm plate	4-6·10^5	7	1-2	4.5-6	1
15 cm plate	1-2·10^6	15	5-8	8-10	3

5.3. Antibodies

Name	Catalog #	Dilution	Application
AF647-anti-GFP nanobodies	Chromotek (home labeled)	1:2·10^3	IS
Actin	Milipore 691001	1:10^4	WB
Bax	Cell Signaling 2772S	1:10^3	WB
Cox IV	Cell Signaling 11967	1:50	WB
Drp1	Cell Signaling 26954	1:30	IS
VDAC	Abcam 14734	1:10^3	WB
Anti-mouse	Jackson 115-035-003	1:10^4	WB
Anti-rabbit	Jackson 111-035-003	1:10^4	WB
CF680 anti-mouse	Sigma SAB4600371	1:500	IS

WB = Western Blot, IS = Immunostaining

5.4. Fluorescent proteins

Gene	Backbone	Cloning sites	Primers for cloning (5'-3')
pEGFP-Bax	pEGFP -C1	HindIII EcoRI	Gift from N.Brady
Mito-dsRED	pEYFP -Mito	-	Gift from DKFZ Genomics Core Facility
mMaple-Mito	pEYFP -Mito	BamHI	CGCGGATCCATGGTGAGCAAGGGCGA
		XbaI	GCTCTAGATTACTTGTACAGCTCGTCC
mMaple-Bax	pEGFP -Bax	NheI	CTAGCTAGCACCATGGTGAGCAAGGGCGA
		HindIII	CCCAAGCTTGCACTGAGCAGCGTAATCTG

6 Protocols

6.1. Cells thawing, passing and freezing

Reagents

- Cells
- PBS
- Trypsin
- Cell culture medium (HeLa: DMEM + 10% FBS + 1% Pen/Strep. MEFs: DMEM + 10% FBS + 1 % Pen/Strep + 50 μM β-mercaphtoethanol. HCT116: McCoy 5A + 10% FBS + 1 % Pen/Strep)
- Freezing medium (Cell culture media with 20% FBS and 10% DMSO)

Materials

- Falcon tubes
- 1 ml-2 ml cryovials
- Cell culture dishes or flasks
- CO_2 incubator
- Laminar hood
- Vacuum pump
- Centrifuge

Procedure

1. Thawing and recovery of cells from liquid nitrogen must be done quickly. Prepare pre-warmed medium in advance. Remove cryovials from liquid nitrogen and immediately place in 37 °C water bath and quickly shake until about 80% has thawed (this should not take more than a minute).
2. Quickly pipette out into a falcon with 9 ml cell culture media and centrifuge at RT, 1200 rpm for 3 min.
3. Remove the media, dissolve the pellet in fresh media, transfer to a 25 cm^2 or 75 cm^2 flask and place in the incubator. Let the cells attach to the flask for at least 24 h before passing them.
4. To passage cells, remove and discard the medium from the cell culture vessel, wash gently with pre-warmed PBS and add pre-warmed trypsin (see Table 5.2 for appropiate volumes). Place in the incubator for 3 min (or until the cells have detached).

5. Once cells are detached, add back 5-10 ml media and transfer to a 15 ml Falcon. If cells are only used for subculturing, dilute the desired amount of cells in fresh media in a new cell culture vessel and place in the incubator. If cells are going to be frozen, continue to step 6.

6. To ensure the cells are healthy enough for freezing, the viability should be over 90%. Count the cells using trypan blue for a viable cell count. Spin down at 1500 rpm for 5 minutes and remove medium.

7. Resuspend cells in enough freezing medium to create a cell suspension of 10^6 cells per ml (do not pre-warm freezing medium). Pipette up and down to ensure even mixture and aliquot 1 ml into storage cryovials.

8. Transfer cells immediately to a freezing container and place them at -80 °C overnight before permanent storage in liquid nitrogen. This step must be done as soon as the cells are in freezing media. DMSO is toxic to cells and so should not be exposed to the cells at room temperature for any longer than necessary.

6.2. Confocal live cell imaging

Reagents

- Cells
- Phenol red free cell culture medium
- PBS
- Staurosporine

Materials

- Glass bottom 8-well chamber
- Confocal microscope LSM 710 (Carl Zeiss, Jena, Germany) with a ConfoCor3 module and a C-Apochromat 40x, 1.2 N.A. water immersion objective

Procedure

1. Grow cells on 8 well μ-slide for 24h to 70-80% confluency and transfect them if needed (see section 6.3).

2. Maintain cells in 200-300 μl of phenol-red free DMEM at 37 °C and 5% CO_2 for imaging. For apoptosis induction, add Staurosporine to the medium (1 μM final concentration).

3. Image acquisition: Use the 40x, N.A. 1.2 water immersion objective and select the appropriate optical setup for the fluorophores under study. For z-stack, time series measurements, choose the following settings:

   a) Frame: typically 512x512 for a good compromise between image quality and size.

b) Direction bidirectional.

c) Averaging: choose at least an averaging of 2. Increase it for single snapshots to have the best resolved image. For time series experiments, find a compromise between the averaging and the scan time to have a sufficient resolution in the desired scan time.

d) Scanspeed: adjust it depending on the time interval settings.

e) Z-stack: focus on the bottom on the cell, "set first" plane, then focus on the top and "set last". Choose a range of stacks with the smallest interval possible.

f) Time series: Choose the cycles and interval time according to the specific measurement. Be sure that the interval time is long enough to acquire one z-stack image with the chosen acquisition mode and averaging.

6.3. Cell transfection

Reagents

- Adherent cells (70% confluency)
- PBS
- Trypsin
- Cell culture medium (HeLa: DMEM + 10% FBS + 1 % Pen/Strep. MEFs: DMEM + 10% FBS + 1 % Pen/Strep + 50 μM β-mercaphtoethanol. HCT116: McCoy 5A + 10% FBS + 1 % Pen/Strep)
- Opti-MEM medium
- Transfection reagent (Lipofectamine 2000)
- DNA

Materials

- Falcon tubes
- Cell culture dishes or flasks
- CO_2 incubator
- Laminar hood
- Vacuum pump

Procedure

1. One day before transfection, seed 5000-8000 cells per well in 200 μl growth medium (Representative protocol for transfection in 1 well of a glass bottom 8-well chamber. See section 5.2 for extrapolation).

2. For each transfection sample, prepare complexes as follows:

   a) Dilute DNA (0.1 to 0.2 μg) in 25 μl of Opti-MEM. Mix gently

   b) Mix Lipofectamine 2000 gently before use, then dilute 0.5 μl in 25 μl of Opti-MEM. Incubate for 5 minutes at room temperature. Note: Proceed to step 2c within 25 minutes.

   c) After the 5 minute incubation, combine the diluted DNA with diluted Lipofectamine2000 (total volume = 50 μl). Mix gently and incubate for 20 minutes at room temperature (the solution may appear cloudy). Note: Complexes are stable for 6 hours at room temperature.

3. Add the 50 μl of complexes to each cell-containing wells and 200 μl medium. Mix gently by rocking the plate back and forth. Note: Although not required, you may replace the old growth mediums added the day before transfection (step 1 of this procedure) with fresh medium.

4. Incubate cells at 37 °C in a CO_2 incubator for 18-48 hours prior to testing for transgene expression. (Note: For plasmids containing Bax, do not let the transfection proceed for more than 12 hours to avoid massive cell death). The medium may be changed after 4-6 hours.

6.4. Western-blot

Reagents

- Cells
- PBS
- Lysis Buffer with protease inhibitors
- Bradford reagent
- Water
- BSA protein standard
- 6x Laemmli Buffer
- SDS Running Buffer
- Transfer buffers (Anode I, Anode II and Cathode)
- Milk (5% w/v in PBS)
- Antibodies
- Methanol
- TBS-T

Materials

- Falcon tubes
- PAGE gels
- Electrophoresis chamber
- Transfer system (Trans-Blot, Biorad)
- PVDF membranes

Procedure

1. Place the cell culture dish in ice and wash the cells with ice-cold PBS.
2. Drain the PBS, then trypsinize the cells.
3. Inactivate trypsin with cell culture medium and transfer the suspension into a tube. Centrifuge at 4 °C, 1500 rpm for 5 min. Discard the supernatant, resuspend the pellet with PBS and spin down again for 5 min.
4. Drain PBS and resuspend the pellet in 50 to 200 μl Lysis Buffer + protease inhibitors. Transfer to an 1.5 ml tube and incubate on ice for 30 min.
5. Centrifuge at 4 °C, 14000 rpm for 30 min.
6. For total protein extraction, gently remove the tubes from the centrifuge and place on ice, aspirate the supernatant and place in a fresh tube kept on ice. Discard the pellet.

7. Perform a Bradford assay with BSA as a protein standard (concentration range for the standard curve: 0 to 1.5 mg/ml).

8. Add Buffer Laemmli 6x to the protein suspension and boil the mixture at 99 °C for 5 min.

9. Load the samples in the PAGE gels (typically 10-15 μg per well) and run the gel at constant voltage (80V) while the samples are still in the stacking gel. Turn up the voltage to 120-150V afterwards if desired.

10. Transfer the proteins to a PVDF membrane:

    a) Equilibrate the gel in Cathode buffer for 10 min to remove residual SDS. (very important for a successful transfer).

    b) Activate the PVDF-membrane in methanol, water and anode II Buffer (1 min in each).

    c) Immerse the Whatman papers in the correct Buffer until wet (see d).

    d) Mount the transfer sandwich, membrane and gel in the following order (from bottom to top): 2 Whatman papers in Anode I Buffer - 1 Whatman paper in Anode II Buffer - membrane - Gel - 3 Whatman papers in Cathode Buffer. Proceed with the transfer.

11. Block the membrane with 5 % milk or with 5 % BSA in TBS-T as specified on the antibody datasheet.

12. Incubate in a 50 ml falcon with the primary antibody diluted into 10 ml of 5 % milk or into 5 % BSA n TBS-T. Rotate overnight at 4 °C.

13. Wash the membrane 3 times with TBS-T.

14. Incubate with secondary antibody for 1 h at room temperature.

15. Develop membrane.

6.5. Single-molecule localization microscopy

Reagents

- PBS
- PFA 4%
- Antibodies
- BSA
- Glycine
- Triton X-100
- Ammonium chloride (NH_4Cl)
- Imaging buffer

Materials

- Vacuum pump
- Humid chamber (plastic box with wet filter paper and parafilm)
- Tweezers
- Custom-made microscope

Procedure

1. Immunostaining:
   a) Grow cells on 24cm round glass coverslips for 24h to 70-80% confluency and transfect (see section 6.3).
   b) Fix cells in 4% PFA in PBS for 10 min at RT.
   c) Incubate the coverslides in 50 mM NH_4Cl (in PBS) for 15 min.
   d) Permeabilize cells with 0.25% Triton-X100 (in PBS) for 5 min.
   e) Wash cells 3 times for 5 minutes with PBS.
   f) Block for 45 min with 1% BSA (in PBS).
   g) Incubate slides with 50 ng/ml of AF647-anti-GFP nanobodies (1/2000) or the appropiate primary antibody diluted in 1% BSA (in PBS) for 90 min. Incubate with the first antibody (1:50 to 1:500 dilutions in BSA) for 90 minutes in the dark. For this step, put the antibody drop on a wet chamber (15 μl for 15 mm slides, 25 μl for 25 mm slides) and place the slide on the drop with the cells facing the liquid. In order to achieve an homogeneous incubation, touch first the drop with border of the slide and let it fall on it. Be sure that there are no air bubbles between the paper and the parafilm in the chamber.
   h) If secondary antibody labeling is required, dilute it in 1% BSA (in PBS) and incubate the slides for 30 min.
   i) Return the slides to the cell culture well-plate with the cells facing up and wash 3 times with PBS. Keep in PBS in the dark at 4 °C until imaged.

2. Mount the coverslides with the cells facing up covered with 300 μl of Imaging Buffer and image in a custom-made microscope.

3. The specific SMLM measurements in this work were done as follows: we used an exposure time of 15 ms for single color and 30s for dual color measurements and an EM gain of 100. Imaging laser intensity at 640 nm was 2.5 kW/cm^2 and the 405 nm activation laser intensity was automatically adjusted to keep a constant number of localizations per frame. Typically 70000-100000 frames were recorded. Analysis was performed using a custom Matlab script. Localizations with uncertainties above 15 nm were discarded.

4. Image analysis and quantification of structures was done with ImageJ. The histogram bin number was determined by the square root of the number of events.

6.6. Cloning

Reagents

- HF Buffer
- dNTP mix
- Primers
- Template DNA
- Agarose
- Restriction enzymes
- Phusion polymerase®
- T4 Ligase
- PCR purification Kit
- Gel extraction Kit
- MiniPrep Kit

Materials

- PCR machine
- Electrophoresis chamber
- UV gel developer
- Thermoblock

Procedure

1. Amplify the DNA product by PCR as in the Phusion Polymerase® manufacturer's protocol.

2. Purify PCR product with the purification kit (check the correct isolation of the product by running an aliquot on an agarose gel).

3. Digest PCR product and the backbone vector with the appropriate enzymes (use conditions and buffers recommended by NEB).

4. Run the digested DNA on an agarose gel, purify insert with the Gel extraction kit and quantify the DNA.

5. Ligate with T4 DNA Ligase as in manufacturer's protocol. Use a ligation molar ratio from 1:3 to 1:10 (insert:vector).

6. Transform DH5α bacteria with 5 to 10 μl of the ligation product and plate on agar. Incubate the plates ON at 37 °C

7. Pick single colonies and grow them in LB media plus antibiotics. Purify DNA by MINIPrep Kit.

8. Quantify and send DNA for sequencing.

6.7. Cell fractionation and protein cross-linking

Reagents as in section 6.4 plus MB Buffer, BMH (0.5 M in DMSO) and DTT
Materials as in section 6.4 plus Teflon douncer
Procedure:

1. Seed cells (at least 5 15 cm^2 dishes for a proper mitochondrial yield) and follow with protein extraction (steps 1 to 6 of section 6.4)

2. For mitochondrial protein extraction, resuspend cell pellet in MB Buffer (2 or 4 ml depending on the pellet size) and homogenize in a Teflon douncer for 100 strokes (check cell integrity by trypan blue dye, about 70% of the cells should be dyed).

3. Centrifuge samples at 4 °C, 800 x g for 10 min several times with 2 ml MB Buffer (until no pellet is visible). Save the supernatants of every centrifugation.

4. Collect all the supernatants and centrifuge at 4 °C 10,000 x g for 10 min to pellet the mitochondrial fraction. Resuspended pellet in MB Buffer (50 to 200 μl) and centrifuge post-mitochondrial supernatant at 4 °C, 100000 x g for 60 min to obtain the cytosolic fraction.

5. If no further crosslinking is required, boil mitochondrial and cytosolic extracts for 5 min in 6x Laemmli Buffer and process for electrophoresis and western blotting. For cross-linking assay, continue to step 6.

6. Incubate purified mitochondria with BMH (final concentration of 10 mM) at RT for 45 min under gentle agitation. Quench BMH in 0.5 M DTT in MB Buffer at RT for 15 min. Centrifuge mitochondria at 4

°C, 9000 x g, resuspend mitochondrial pellet and wash twice in MB Buffer.

7. Boil mitochondria in 6x Laemmli Buffer and process for electrophoresis in 10% acrylamide gels and western blotting.

6.8. STED microscopy

Reagents

- PBS
- Cells
- PFA 4%
- Mowiol

Materials

- Glass coverslips
- Tweezers
- STED custom-made microscope

Procedure

1. Grow cells on round glass coverslips for 24h to 70-80% confluency, transfect (see section 6.3) and fix with 4% PFA for 10 min at RT.

2. Wash 3 times with PBS, mount on slides with Mowiol and let them dry overnight.

3. The specific STED measurements in this work were done as follows: We used a pulsed diode laser operating at 485 nm and a pulsed raman fiber laser operating at 560 nm for excitation and stimulated emission, respectively. The STED beam was spatially formed to a doughnut by a vortex phase plate. On a longpass filter, both excitation and STED beam were overlaid and coupled to the microscope stand (Leica Microsystems, Germany) utilizing an 100x oil objective (1.4NA, HCX PL APO, Leica Microsystems, Germany). Four galvanometer mirrors scanned the image field. The fluorescence was separated on a bandpass filter and guided to a hybrid photodetector. A FPGA-based software controled the hardware and the data acquisition. Export of the raw data into tiff-Files and the Gaussian filtering was done with ImSpector® Image Acquisition & Analysis Software v0.10 (http://www.imspector.de).

6.9. Fluorescence correlation spectroscopy (FCS)

Reagents

- Lipids
- Recombinant proteins
- GTPase Buffer
- GTP
- BSA
- Sucrose
- Chloroform
- Ethanol

Materials

- Electroformation chamber with Platinum wires
- Function generator
- Labteck chambers 8-well
- Confocal microscope LSM 710 (Carl Zeiss, Jena, Germany) with a ConfoCor3 module and a C-Apochromat 40x, 1.2 N.A. water immersion objective
- Hardware autocorrelator

Procedure

6.9.1. System calibration

FCS measurements rely on proper alignment and characterization of the confocal volume. The calibration also serves to compute for the parameters related to the shape of the detection volume (W_0 and S).

$$S = \frac{W_z}{W_0} \tag{6.1}$$

$$D = \frac{W_0^2}{4\tau_D} \tag{6.2}$$

A calibration measurement is done with a dye that is spectrally similar to the fluorophore that will be measured in the membrane and whose diffusion coefficient (D) is known (e.g. Alexa 488 for GFP).

1. Switch on the lasers around 1 hr before the measurements to allow stabilization.

2. For dual color FCS, add 200-300 μl of a dilute solution of Alexa 488 and Alexa 633 (approx. 10 nM) to an empty blocked well of a Labteck chamber and place it under the microscope.

3. Go to FCS tab > Load method (Set up the FCS conFig.uration of the microscope that best fits the spectral properties of the fluorophore under study). The optical setup used in this work for dual color 488/633 was: dichroic mirror MBS was set at 488/561/633, beamsplitter at

575, the filter at the APD1 (red) was set at LP 650 and the APD2 (green) was at 505-540 nm.

4. Adjust laser: select a laser power that gives maximum counts per molecule without significant photobleaching during the acquisition time. Depending on the microscope and sample, this is usually around 0.3-1%. Usually start with 0.5 and go lower if you feel there is bleaching. Focus on the minimum z-value, Go to "count rate" and focus up until the count rate increases dramatically. Then focus 0.1-0.2 mm above to make sure we are inside the focal volume (neither on the coverslip, nor on the surface).

5. Adjust pinhole with respect to the beam path under Lightpath > Adjust pinhole: set the pinhole to 1 AU. Adjust ch1 and ch2 for X and for Y. Do a "fine" adjustment, and if there is no peak on the histogram, adjust on the "course" mode.

6. With the count rate ON, move the correction ring of the objective without forcing it until the count rate is maximum, to correct for glass thickness of the observation chamber.

7. Go to Acquisition and set the measurement time to a value 10^4 longer than the diffusion time of the dye to have a good aproximation to 0 in the crosscorrelation curve. Alexa 488's diffusion time is 15-30 μs, so measure for at least 10 s. Start measurement.

8. Fit the autocorrelation curve and estimate the diffusion time and the structure parameter under Fitting. Uncheck repetitions that are erroneous (going out-of-focus, with aggregates etc.). Go to the Correlate tab and select an appropriate model function. For the calibration samples or other solution samples, use "3D 1 component with triplet". Select "Fit All" and evaluate the average of all the curves.

6.9.2. Point FCS

Point FCS is done similar to the calibration measurement, but one has to adjust the measuring times and repetitions accordingly.

1. Mix the recombinant proteins with GTP (0.1 mM) in GTPase Buffer to a final volume of 300 μL and add the solution to a blocked well in a Labteck chamber. Incubate for 15-20 min or heat at 42 °C for 30 min (only for Bax activation). Place the chamber under the microscope. The protein concentration used were 50 nM Drp1_G, 50 nM Bax_R, and 100 or 150 nM Bcl-xL_R.

2. Set up measurement. For dyes and small proteins, 60 s may be sufficient. We do several repetitions (3-5 per well) to make sure that you can remove a repetition if a big aggregate passes through the confocal volume.

6.9.3. sFCS on GUVs (2 focus, 2 color)

1. Clean the electroformation chamber with water and ethanol and let it dry.

2. Block the wells of a Labteck chamber with 10 mg/ml BSA in PBS for 15 min. Wash with water and GTPase, let it dry for 5 min.

3. Dissolve lipids in chloroform and mix them in the ratio 54: 26: 20 mol % (DOPC/CL/EggPE , respectively)

4. Evaporate solvent under nitrogen flux and subject to vacuum for at least 1h.

5. Rehydrate lipid mixtures in chloroform to a final concentration of 2 mg/mL.

6. Take 2.5-3 μl of the lipid stock and spread it on each of the Pt wires on the side that screws inside the electroformation chamber. Allow the solvent to evaporate completely.

7. Add 350 μl of 300 mM sucrose solution to each electroformation chamber. Close the tube with the lid once the lipids are on the wire.

8. Connect the cables of the function generator to each of the two Pt-wires avoiding contact between them. Apply 10 Hz frequency, 1.5 V, 1h 45 min. (GUV are formed and stick to the platinum wire).

9. Decrease the frequency to 2 Hz, 1.5 V, 30-45 min (GUVs are detached from the wire).

10. Mix the recombinant proteins (20 nM $Drp1_G$, 50 nM Bax_R, 50 nM Bcl-xL_R, and 200-300 nM cBid). with the nucleosides or M-divi1 if needed in GTPase Buffer to a final volume of 300 μL and add the solution to a blocked well in a Labteck chamber.

11. Cut the end of a micropipette tip to widen the opening and gently take the GUV suspension from the electroformation chamber (usually 50-100 μL). Add it on the protein solution and let it incubate for 10-15 min or heat at 42 °C for 30 min (only for Bax activation).

12. Place the chamber under the microscope and adjust the optical setup for 488/633 dual color measurements: dichroic mirror MBS at 488/561/633, beamsplitter at 575, the filter at the APD1 (red) at LP 650 and the APD2 (green) at 505-540 nm.

13. Select a GUV (a good size for sFCS is ~20 μm). Be careful, the detectors are very sensitive, so do not choose the brightest GUVs.

14. Set up the measurement: Zoom to 6x on the GUV > Save image > Zoom to 12x on the tangent to the GUV > Set angle to 45° > Scan and select the equator of the GUV (if possible without aggregates) > Snap.

15. Choose the following settings: Frame size 32x2, Line step 1, Speed 15, direction unidirectional, 8 bit, Zoom 12 (scan time should then be 1.89 ms), angle 45°> Fix the crop center in the middle of the GUV equator > Start continuous acquisition.

16. Start the autocorrelator and collect photons for 300 s. Every single measurement has to be at least 10^4 times longer than the dye diffusion time ($\sim$ 30 ms in membranes) to obtain a good aproximation to 0 in the crosscorrelation curve.

Part III.

Results

7 Apoptosis imaging in single, mammalian cells

7.1. Optimization of apoptosis visualization

Several factors can affect the timing and progression of apoptosis in mammalian cells: type of cell death induction, mitochondrial priming status, treatment dose, rate of initiator caspases' cleavage, cell cycle stage, or gene expression, among others. These factors contribute to a cell-to-cell variability in the response to apoptosis stimuli. In order to standardize a protocol that allows the visualization of apoptotic progression in a large number of cells during a reasonably short time window, we must first determine when cells start to undergo apoptosis after certain stimuli. To do so, we optimized the following conditions: cell type, drug type, and treatment dose.

Table 7.1 summarizes the different apoptosis inducers tested (actinomycin D, etoposide, or staurosporine (STS)). After the addition of the drug, we recorded time series experiments with a confocal microscope (protocol 6.2). To rule out cell specific response to the treatments, we used different cell lines (HeLa, MCF-7, Cos). Although the response to the drugs was heterogeneous in the cell population, cells started to display apoptotic features one hour after drug addition (Video 1, HeLa cells after treatment with 1 μM STS, video starts 45 min after the treatment). Lower concentrations of actinomycin D did not induce apoptosis until four hours after the stimuli (Fig. 7.1). However, six hours after the induction, most of the cells were dead in every condition, as judged by blebbing, round morphology, and detachment from the surface. These observations indicated that, under the specific conditions tested, the range between two to six hours after apoptosis induction is the best time frame to study the molecular events related to this process. The standard method for apoptosis induction used throughout the experiments of this thesis was 1 μM STS.

Drug	Dose	Mechanism of action
Actinomycin D	5 or 10 μg/ml	Inhibition of mRNA synthesis
Etoposide	100 μM	Blocking of DNA synthesis
CCCP	5 μM	Uncoupling of the mitochondrial oxidative phosphorilation
Staurosporine	1 μM	Inhibition of protein kinases

Table 7.1. Drugs and treatment dose used to induce apoptosis

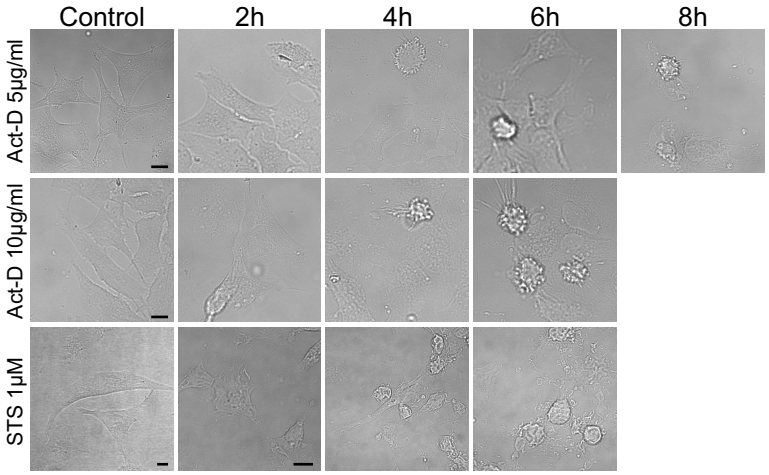

Figure 7.1. Apoptosis induction. Live cell imaging of HeLa cells treated with different drugs and dose.

7.2. Bax translocation to the MOM correlates with mitochondrial depolarization

Bax is a soluble monomeric protein constitutively shuttling between the cytosol and the mitochondrial surface of healthy cells (Edlich et al., 2011). Following cell stress, Bax is activated and accumulates at the MOM, where it undergoes major conformational changes (Lovell et al., 2008), inserts in the membrane, and oligomerizes to mediate MOM permeabilization (Annis et al., 2005; García-Sáez et al., 2004). The most accepted model of MOM permeabilization proposes the formation of Bax pores that allow cytochrome c and the other apoptotic factors to go through. Recent structural studies have also shown that active, membrane-embedded Bax arranges into symmetric dimers, which serve as building blocks for the larger aggregates that mediate membrane disruption (Bleicken et al., 2010, 2014; Czabotar et al., 2013; Subburaj et al., 2015). Yet, the supra-molecular arrangement of Bax in mitochondria during apoptosis and its relationship with MOM permeabilization remain elusive.

In order to tackle Bax organization in single apoptotic cells via microscopy, we used the cellular system described in section 7.1 , based on HeLa cells treated with STS. We transfected the cells with GFP-Bax and stained them with the membrane potential dependent dye TMRE (protocol 6.3). This allowed us to track Bax translocation in parallel to mitochondrial depolarization, and to identify the time point after apoptosis induction when most of the Bax signal is heterogeneously distributed in discrete foci at the MOM.

After STS treatment, Bax translocation from the cytosol to the mitochondria was detected by the change from diffuse, cytosolic fluorescence intensity to a discrete, heterogeneous signal in the green channel (Fig. 7.2a,b, Video 2). We related it with parallel mitochondria depolarization monitored by

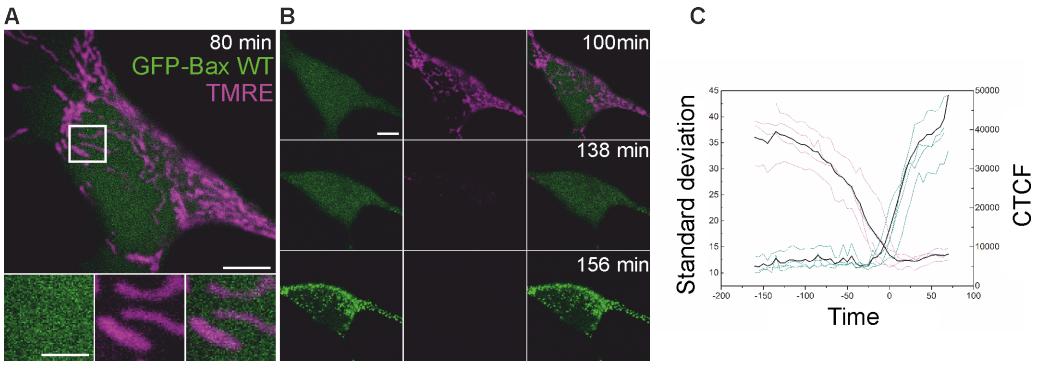

Figure 7.2. Bax translocation correlates with mitochondrial depolarozation. (A) Confocal live cell imaging of HeLa cells overexpressing GFP-Bax (green) and mitochondria stained with TMRE 100 nM (magenta) show cytosolic GFP-Bax distribution and healthy mitochondria. Lower panels are zoomed images corresponding to the white rectangle in the upper panel and represent the individual and merged channels. Time shows the minutes after apoptosis induction with STS 1 μM. Scale bars, 5 μm (overview) and 2 μm (zooms). (B) HeLa cells shown in A at longer times after STS treatment. Images show sequential GFP-Bax translocation (green), which correlates with mitochondria depolarization (TMRE, magenta). Scale bars, 5 μm. (C) Standard deviation of the fluorescence intensity of GFP-Bax (blue) versus the corrected total cell fluorescence (CTCF) of TMRE (purple) in individual cells (N=4). CTCF= Integrated Density – (Area of selected cell × Mean fluorescence of 3 background readings). Time 0 corresponds to the normalized time when both events cross in each cell. Black line represents the average of the individual cells. .

the loss of TMRE fluorescence in the red channel. After two-hour treatment, cells started to lose their potential and most GFP-Bax appeared translocated to mitochondria, although some cells still retained high mitochondrial membrane potential even after 4 hours. 6 hours after adding STS, all cells exhibited a heterogeneous Bax pattern and TMRE fluorescence was not perceptible any more. We plotted the kinetics of these events for each individual cell as the increase in the standard deviation of the GFP fluorescence intensity, corresponding to Bax translocation to the MOM, against the total TMRE fluorescence per cell, which indicates mitochondrial potential (Fig. 7.2c). These results indicated that GFP-Bax translocation and mitochondria depolarization correlate with each other, as expected, and that the most suitable time frame to study Bax structural organization in apoptosis was from 2 to 6 hours after the drug treatment.

As a functional control for Bax tagged with GFP, we transfected HeLa cells with GFP-Bax 1-2/L-6, an inactive Bax mutant that constitutively binds to mitochondria of healthy cells but does not permeabilize the membrane (Edlich et al., 2011) (Fig.7.3). This mutant remains in its inactive form but bound to the membrane due to the presence of a disulfide bond between Bax helices 1 and 2 and the constriction of the loop between those two helices to the tip of helix 6. Under control conditions, we detected most

of GFP-Bax 1-2/L-6 signal at polarized mitochondria, as indicated by the TMRE fluorescence. This indicates that the MOM remained impermeable despite the presence of GFP-Bax 1-2/L-6, in contrast to what we observed with GFP-Bax wild-type. Importantly, this mutant also served as a useful control in the superresolution studies (protocol 8.1).

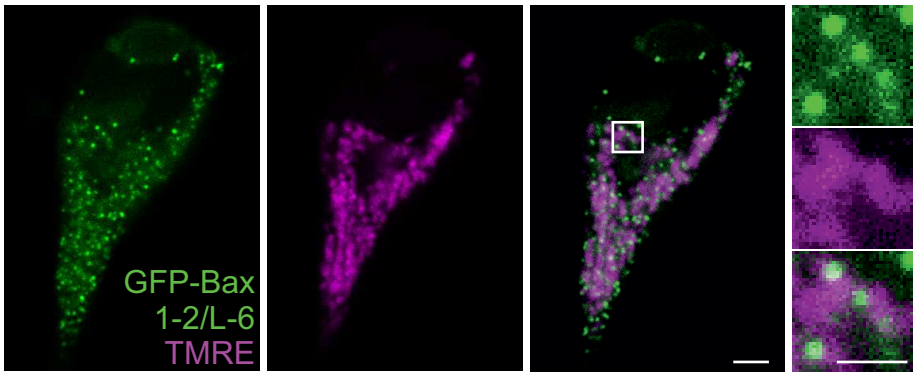

Figure 7.3. Bax inactive mutant does not induce membrane depolarization. HeLa cells overexpressing GFP-Bax mutant (1-2/L-6) (green) and mitochondria marked with TMRE 100 nM (magenta). Images show constitutive GFP-Bax localization to healthy mitochondria without apoptosis induction. Right panels are zoomed images corresponding to the white rectangle in the left panel and represent the individual and overlaid channels. Scale bars, 5 μm (overview) and 2 μm (zooms)

7.3. GFP-Bax is active and oligomerized after apoptosis induction

The depolarization of mitochondria upon GFP-Bax translocation indicated that Bax was active under the conditions tested. To rule out potential overexpression artifacts, we compared the protein expression levels of total Bax in HeLa cells transfected or not with GFP-Bax and found that they were very similar (Fig. 7.4a). It seemed that transfected HeLa cells down-regulated the levels of endogenous Bax so that the total amount of protein allowed survival. As an additional biochemical control for Bax activation, we confirmed that the protein was oligomerized by western blot (protocol 6.4). After cell fractionation and chemical cross-linking, we observed that most of the Bax signal was localized to the mitochondrial fraction and oligomerized into dimers and higher oligomers (Fig. 7.4b) (protocol 6.7).

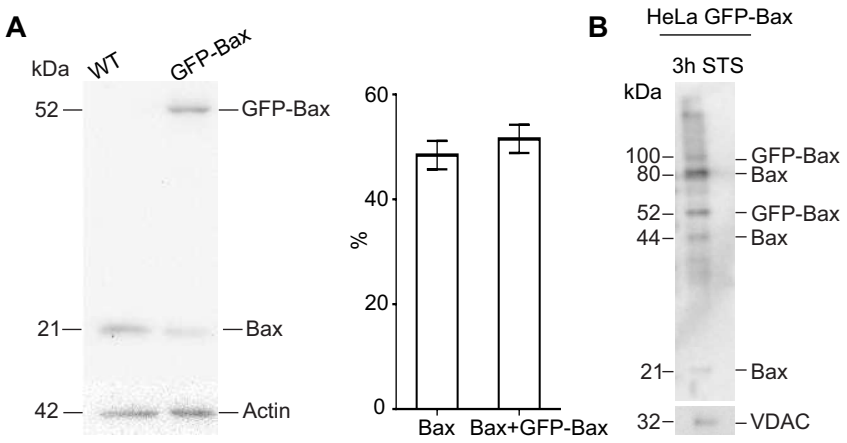

Figure 7.4. Bax is active and oligomerized in the cells after apoptosis induction. (A) Analysis of Bax protein levels in HeLa cells (wild-type and overexpressing GFP-Bax) by Western Blot. The bar graph corresponds to the quantification of Bax expression in HeLa WT and HeLa GFP-Bax cells. Protein expression was first corrected with respect to the loading control (actin). Then, the expression of endogenous Bax from WT cells was normalized to 100% and compared with the total amount Bax (arising from endogenous protein and GFP-Bax) in transfected cells. (B) Analysis of Bax translocation and oligomerization in the mitochondrial fraction by Western Blot. VDAC, loading control.

8 Super-resolution of Bax during apoptosis

8.1. Supramolecular strcuture of Bax oligomers in apoptotic cells: Single-molecule localization microscopy

Confocal live cell imaging revealed that GFP-Bax translocates to discrete foci after an apoptotic insult, presumably at mitochondria (see section 7.2). However, this technique does not have enough resolution to distinguish the shape of such clusters. To investigate the nanoscale organization of Bax oligomers during apoptosis, we used single molecule localization microscopy (SMLM).

We labeled HeLa cells overexpressing GFP-Bax with anti-GFP nanobodies coupled to Alexa Fluor 647 (Af647), a fluorescent probe optimized for super-resolution imaging (protocol 6.5) (Ries et al., 2012). These nanobodies are smaller than usual antibodies (1.5 nm x 2.5 nm) and bind GFP with high specificity (Rothbauer et al., 2006).

We acquired images on fixed cells that had been treated with STS for 2-6 hours and qualitatively showed no difference in the number or shape of structures within this range of incubation times with the drug. In particular, the individual cells selected for imaging in the different experiments exhibited a similar apoptotic state, characterized by GFP-Bax in a dotted distribution, but overall cellular integrity, as judged by the cell shape and the absence of blebs (Fig. 8.1, 8.2a). This was important to minimize the background signal of cytosolic Bax because it would interfere with a proper image reconstruction. Therefore we visualized a specific apoptotic stage corresponding to the organization of Bax signal once almost all molecules are irreversibly bound to mitochondria, but before most cellular components have been disassembled. As the pores induced by Bax are stable and permeabilize mitochondria for long periods of time (Bleicken et al., 2013; Muñoz-Pinedo et al., 2006), the stage of Bax organization we investigated was associated with the pore-forming state of Bax oligomers.

Reconstructed super-resolution images showed a large fraction of the Bax signal as random dots or big aggregates in which no particular structural organization could be distinguished. Strikingly, we also found a significant amount of well-defined non-random structures (Fig. 8.2b,c). Concretely, we identified both full and incomplete (arc-shaped) rings of Bax molecules, as

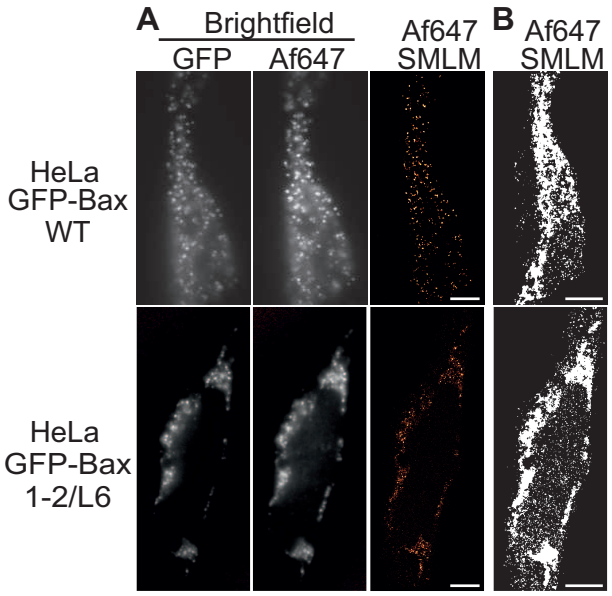

Figure 8.1. Cell shape outlined in super-resolution SMLM. (A) Bright field images and SMLM overviews of HeLa cells overexpressing GFP-Bax or GFP-Bax 1-2/L-6, respectively. Bright field images were taken in the GFP and AF647 channels before acquisition with single molecule localization. Scale bars, 500 nm. (B) SMLM images shown in A, reconstructed with all the localizations and no cut-off applied. Pictures were converted to binary images and a black-white mask was applied to define the cell shape. Scale bars, 500nm.

well as linear assemblies, which in a few cases appeared as double lines (Fig. 8.2c).

In an effort to validate the connection between these defined structures and Bax role in MOM permeabilization, we examined the signal of inactive Bax at mitochondria under control conditions by SMLM. We acquired super-resolution images of healthy HeLa cells transfected with the non-functional mutant GFP-Bax 1-2/L-6 (Figs. 8.1, 8.3). Consistent with the lack of activity, we detected a higher proportion of undefined dots and aggregates in GFP-Bax 1-2/L-6 with respect to its wild type counterpart (GFP-Bax WT), which were in general smaller. To ensure a systematic, blind analysis, we also classified the non-random structures as lines, arcs and full rings (we did not detect any double lines).

8.2. Quantification of GFP-Bax assemblies

8.2.1. Size of the assemblies

In order to compare quantitatively the GFP-Bax assemblies observed via SMLM under apoptotic and healthy conditions, we next counted the total number of structures observed by SMLM in the GFP-BaxWT and GFP-Bax 1-2/L-6 samples. Consistent with the lack of activity of the mutant, we

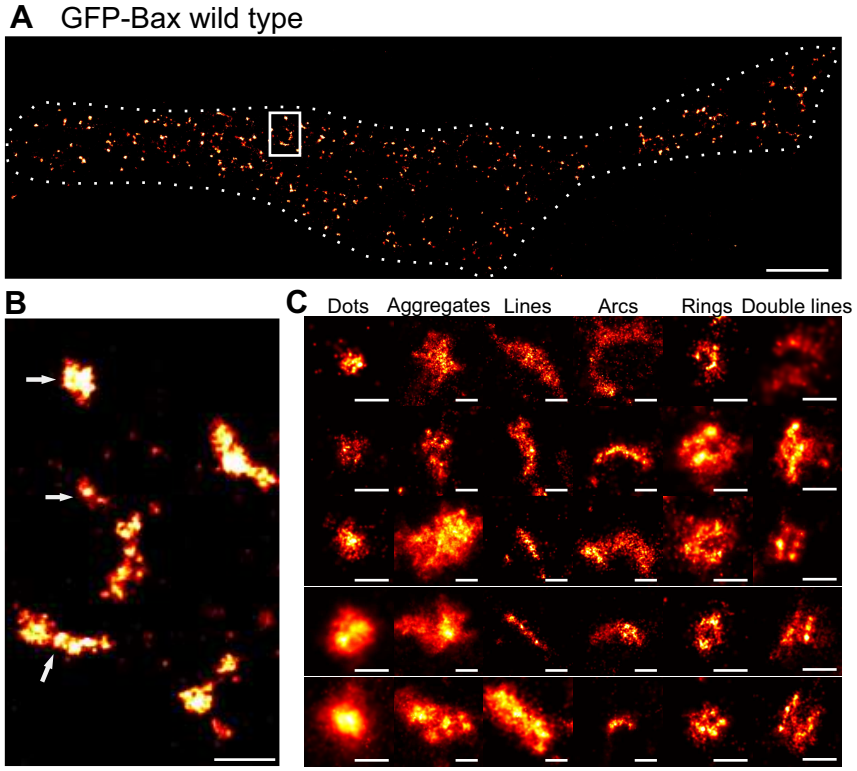

Figure 8.2. SMLM reveals non-random Bax structures during apoptosis. (A) Overview of a reconstructed superresolution image of GFP-Bax overexpressing HeLa cells stained with AF647-anti-GFP-nanobodies. Image was acquired on fixed cells 3 h after apoptosis induction with STS. Dotted line shows the cell shape. Scale bar, 5 μm. (B) Magnified reconstructed superresolution image corresponding to the white rectangle in A showing the shapes of GFP-Bax WT structures (white arrows). Scale bar, 500 nm. (C) Gallery of typical GFP-Bax WT structures during apoptosis found in all the analyzed cells. Scale bars, 100 nm.

detected a higher proportion of undefined dots and aggregates in GFP-Bax 1-2/L-6 with respect to its wild type counterpart (GFP-Bax WT) (Fig. 8.4).

We then calculated different parameters for each type of structure. Concretely, we measured: i) the area of dots and aggregates, ii) the length of the lines, iii) the length and the radius of curvature of the arc assemblies and iv) the radius of the full rings (Fig. 8.5). Although the number of clear complete rings of GFP-Bax WT molecules was lower than that of other structures, they were almost absent in the inactive mutant, which strongly supports their functional character (Fig. 8.4, Fig. 8.5a). Their radius followed a normal distribution centered on a diameter of 35 nm, in good agreement with Bax pores observed in liposomes (Bleicken et al., 2010). In the case of arc-shaped assemblies, their length was broadly distributed and two peaks at approximately 100-300 nm and 400-500 nm could be distinguished for GFP-Bax WT (Fig.8.5b,c). Linear structures also followed a wide distribution in GFP-Bax WT samples with lengths centered at 200-250 nm (Fig. 8.5d).

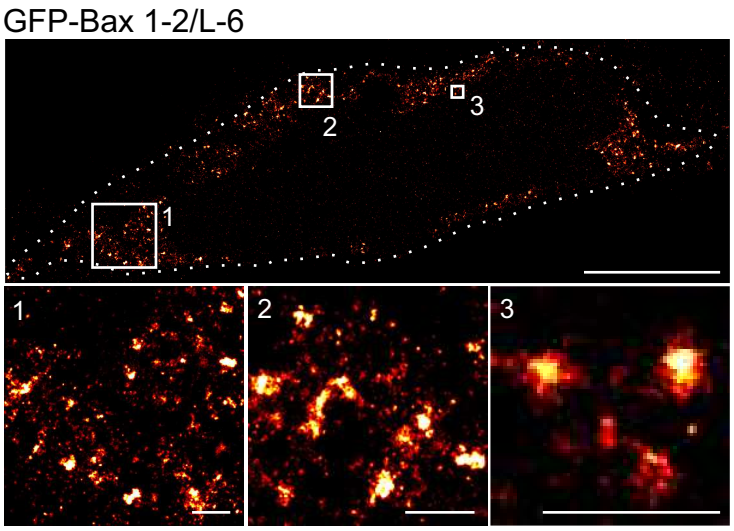

Figure 8.3. Bax inactive mutant displays random structures. Overview (top) and 3 enlarged insets (bottom) of HeLa cells overexpressing GFP-Bax 1-2/L-6 stained with AF647-anti-GFP-nanobodies. Figure shows reconstructed super-resolution images acquired without apoptosis induction. Scale bars, 5 μm (overview) and 500 nm (insets).

In contrast, the inactive mutant exhibited less and shorter arcs and lines (Fig. 8.5b-d). In agreement with Bax oligomerization during apoptosis, the undefined structures were also larger for GFP-Bax WT than for GFP-Bax 1-2/L-6 (Fig. 8.5e-f). In summary, these differences in the signal suggest that the defined structures detected in GFP-Bax WT are distinct from those of the inactive mutant and confirm that they are related to the functional role of Bax in MOM permeabilization during apoptosis.

8.2.2. Distribution of Bax assemblies among the cells

Our quantification involved the total number of structures found in all measured cells together, but it is also important to consider cell-to-cell heterogeneity. To account for this, single cell cumulative distribution functions were plotted. As shown in Fig. 8.6, mutant GFP-Bax 1-2/L-6 overexpressing cells displayed in all cases considerably smaller structures than the active protein. Besides, the cumulative distribution functions of individual cells corresponding to WT or mutant GFP-Bax were similar and could be distinguished as two different populations. These results confirm that the structures analyzed in the images of WT and mutant GFP-Bax are significantly different from each other and comparable in the different cells analyzed for each of them.

In the case of GFP-Bax structures organized as two lines or arcs parallel to each other (Fig. 8.2c), we cannot discard their possible relevance in the molecular mechanism of Bax function at the MOM despite their low numbers. They have a defined shape and their size is comparable to the

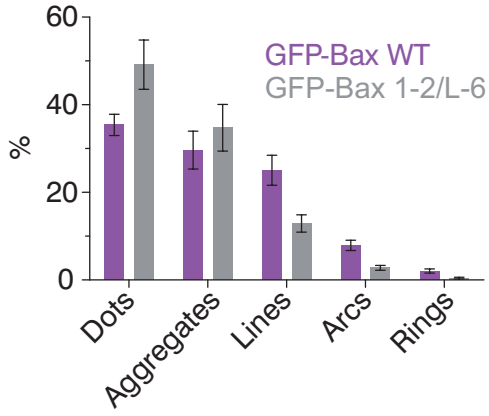

Figure 8.4. Bax inactive mutant shows more random structures. Frequency of the different types of Bax assemblies in HeLa cells with respect to the total number of assemblies found in each condition (GFP-Bax WT or GFP-Bax mutant 1-2/L-6).

single lines. Indeed, these double structures, only detected in GFP-Bax WT images, resembled the spiral assemblies proposed for the dynamin-like protein Drp1 during mitochondrial fragmentation (Mears et al., 2011).

8.3. GFP-Bax organization in Bax/Bak DKO cells

To rule out potential effects due to the presence of endogenous Bax and Bak in HeLa cells transfected with GFP-Bax, we also performed SMLM experiments in Bax/Bak double knock out (DKO) HCT116 cells transfected with GFP-Bax. Fig. 8.7 shows that untransfected cells had no expression of Bax at the protein level. In this different cellular background, these cells needed longer incubation times with the apoptotic drug than HeLa cells in order to show heterogeneous GFP-Bax distribution. After fixing the cells at different times following STS treatment, we observed that 7h was the best time point to analyze GFP-Bax structures by SMLM in HCT116 Bax/Bak DKO cells. In the absence of endogenous protein, we could also identify a significant fraction of non-random GFP-Bax structures including lines, double lines, arcs and full rings of comparable sizes (Fig. 8.7b,c).

8.4. STED microscopy reveals similar structures of Bax during apoptosis

In order to corroborate that the results of SMLM were not dependent on the sample preparation or imaging technique, we directly measured GFP-Bax distribution (without staining with nanobodies) during apoptosis with an alternative super-resolution method, stimulated emission depletion microscopy

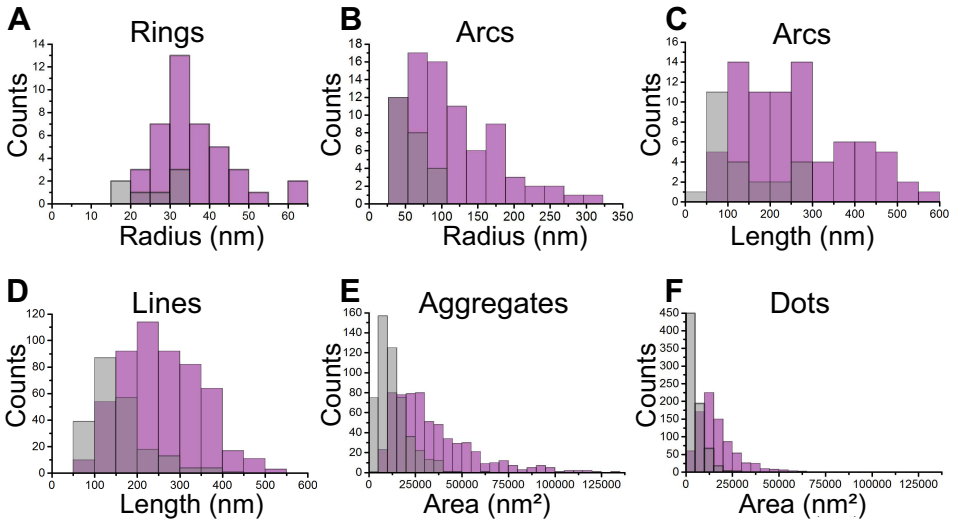

Figure 8.5. Bax wild type adopts different organization from the inactive mutant. (A-F) Histograms show the number and size of the structures found on GFP-Bax WT (purple) and on GFP-Bax 1-2/L-6 (grey) overexpressing cells. Data show the total number of structures in all the measurements. n (Bax WT)= 13, n (Bax 1-2/L-6)=11.

(STED) (Protocol 6.8). This technique has also showed improvements in resolution up to 60 nm for imaging of GFP labeled molecules (Willig et al., 2006; Rankin et al., 2011).

Fig. 8.8 depicts a substantial resolution increase in the STED pictures compared to those acquired with diffraction limited imaging. This technique also revealed comparable non-random assemblies of GFP-Bax shaped as lines, arcs, rings and even double lines (Fig. 8.8b), supporting that the structures characterized with localization microscopy reflect the organization of Bax in apoptotic mitochondria.

As an additional control, we measured the distribution of other mitochon-

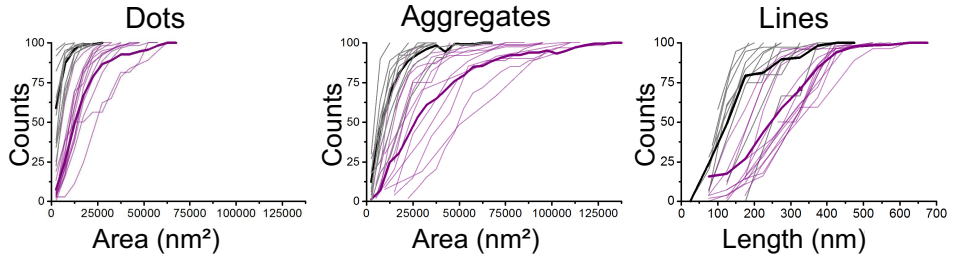

Figure 8.6. Distribution of GFP-Bax structures in each cell displays two different population. Cumulative distribution plots of GFP-Bax wild type (purple) and GFP-Bax 1-2/L-6 (grey) showing differences in amplitude and frequency. Each plot represents a single cell. Thick lines represent average cumulative distributions for all the single cells overexpressing GFP-Bax WT or mutant GFP-Bax 1-2/L-6.

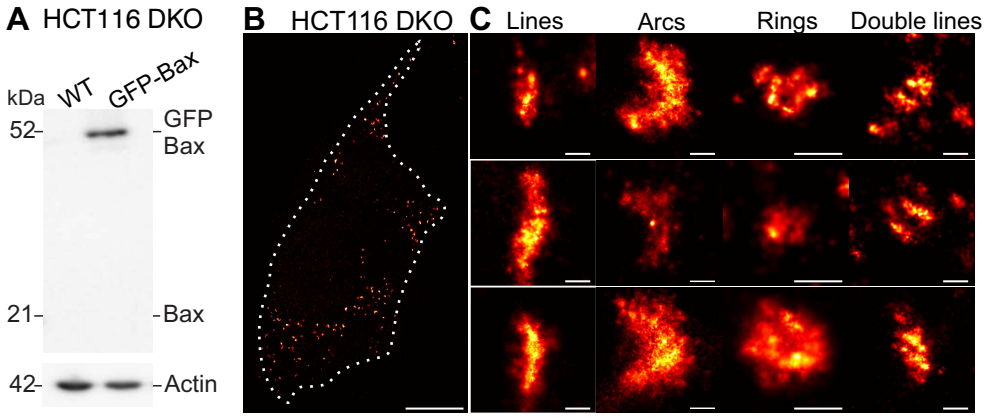

Figure 8.7. GFP-Bax non-random structures are not affected by endogenous Bax. (A) Analysis of Bax protein levels in HCT116 Bax/Bak DKO cells (wild-type and overexpressing GFP-Bax) by Western Blot. (B) Overview of a reconstructed superresolution image of GFP-Bax overexpressing HCT116 Bax/Bak DKO cells stained with AF647-anti-GFP-nanobodies Image was acquired on fixed cells 7 h after apoptosis induction with STS. Dotted line shows the cell shape. Scale bar, 5 μm. (C) Gallery of typical GFP-Bax WT non-random structures during apoptosis on HCT116 Bax/Bak -/- cells. Scale bars, 100 nm.

drial proteins with STED, concretely GFP-TOM20 and GFP-MitoNEET. As shown in Fig. 8.8c and d, the resolution also increased considerably with STED, but the distribution of these proteins differed from that of GFP-Bax. This indicated that the non-random assemblies detected for Bax were not a common organization of constitutive mitochondrial proteins.

8.5. Bax shows a heterogeneous distribution at mitochondrial foci during apoptosis

Previous studies have shown that mitochondria undergo massive fragmentation upon apoptosis induction and that Bax localizes at the specific foci where this process takes place (Karbowski et al., 2002).

To determine the position and orientation of GFP-Bax structures on the MOM, we carried out dual color confocal and super-resolution experiments.

We first performed time series confocal imaging on HeLa cells co-transfected with GFP-Bax and mito-dsRED (mitochondrial marker) following STS treatment. After approximately one hour, GFP-Bax started to accumulate at discrete sites at mitochondria (Fig. 8.9). This Figure (panel b) also illustrates that GFP-Bax localized specifically at mitochondrial tips after apoptosis induction (Videos 3-6).

However, confocal microscopy cannot provide information about the structure or orientation of Bax assemblies on the membrane at the nanoscale. For this reason, we performed two-color SMLM on HeLa cells transfected with GFP-Bax, which were immunostained 3 hours after apoptosis induction

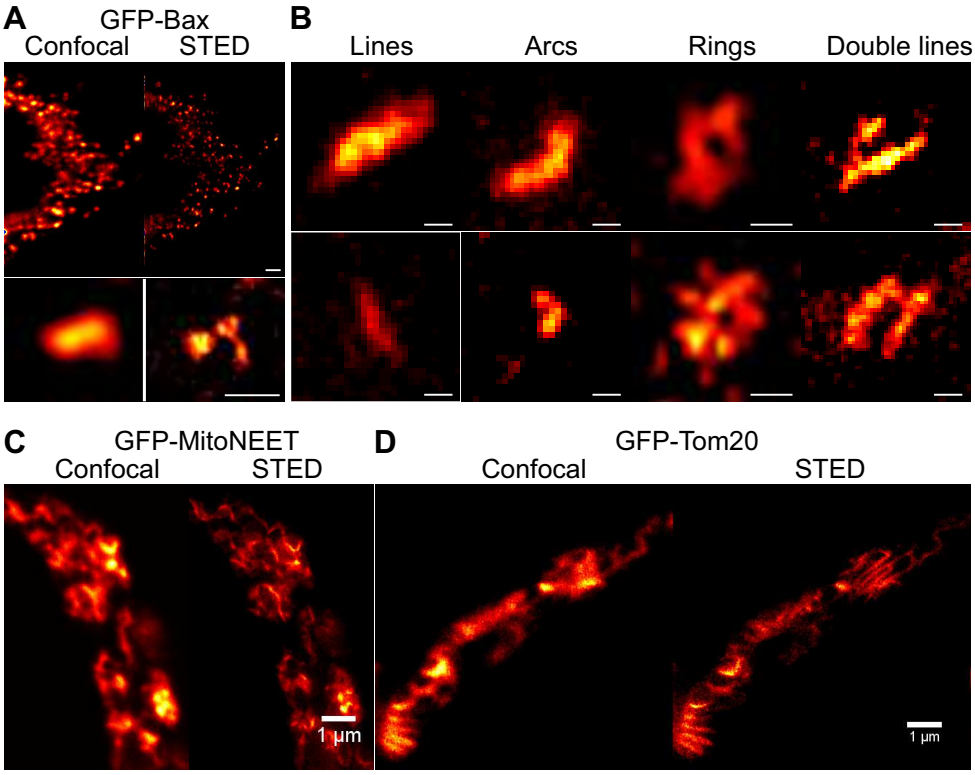

Figure 8.8. Bax non-random structures revealed by STED. (A) Comparison of confocal (left) and STED (right) images of GFP-Bax overexpressing HeLa cells 2h after STS treatment. STED reveals a notable increase in resolution. Scale bars, 500 nm. (D) Representative GFP-Bax non-random structures found with STED (lines, arcs, rings, double lines). Scale bars, 100 nm. (C-D) Comparison of confocal (left) and STED (right) images of HeLa cells overexpressing the mitochondrial proteins GFP-MitoNEET or GFP-Tom20 2h after STS treatment.

with AF647–anti-GFP nanobodies for Bax signal and CoxIV antibody (with CF680 as secondary antibody) as a mitochondrial marker (Fig. 8.10a). As an alternative to CoxIV imaging, we co-transfected the cells with mMAPLE-mito, a photo-switchable fluorescent protein suitable for SMLM that acted as mitochondrial marker (Fig. 8.10b). The images qualitatively showed all GFP-Bax signal heterogeneously distributed in discrete foci on mitochondria in both cases, as expected. In particular, it localized along the mitochondrial tubules as well as on mitochondrial ends. Non-random arrangements corresponding to Bax assemblies could be distinguished in structures wrapping mitochondria, in addition to dots and aggregates (Fig. 8.10). When we examined if the distribution of the non-random assemblies of GFP-Bax were detected preferentially at specific sites along the mitochondrial network, we did not observe any clear preference.

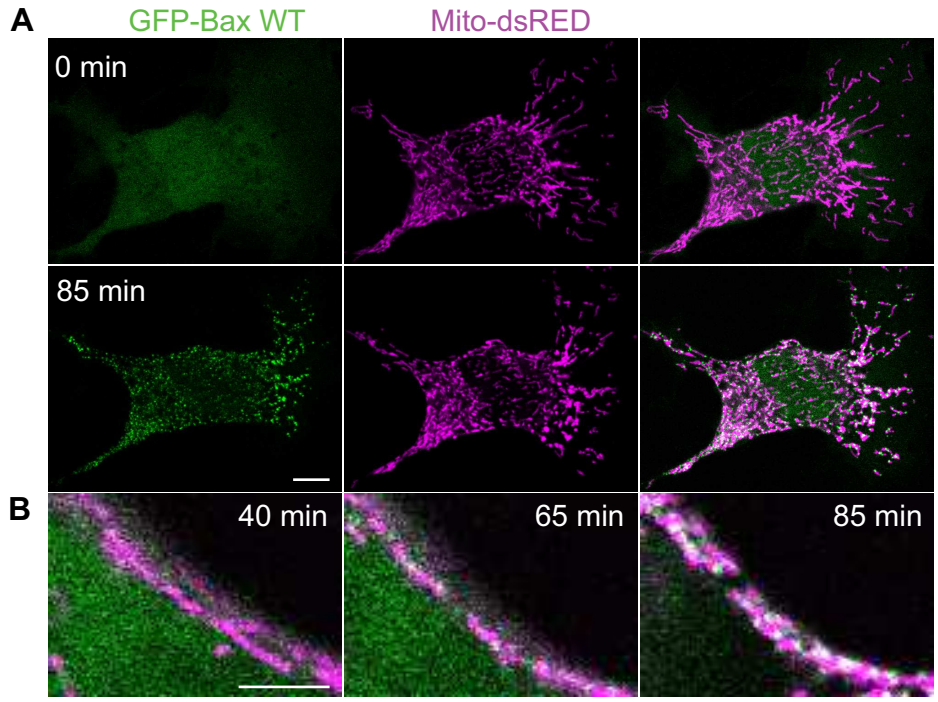

Figure 8.9. Confocal microscopy: Bax localizes to discrete mitochondrial foci during apoptosis. (A) Left panel shows the individual channels and overlaid images of confocal live cell imaging of HeLa cells overexpressing GFP-Bax (green) and mito-dsRed (magenta) at 0 and 85 minutes after apoptosis induction with STS 1µM. Scale bars, 10 µm. (B) Zoomed overlaid images of HeLa cells following GFP-Bax translocation (green) and mitochondrial fragmentation (magenta) during apoptosis induction with STS 1 μM. See also Videos 3 to 6. Scale bars, 2 μm.

8.6. MOM pores observed by electron microscopy

So far the existence of pores on the mitochondria of apoptotic mammalian cells has not been reported in the literature. In order to check if the presence of non-random Bax structures correlated with the opening of pores at the MOM, we analyzed the mitochondria of HeLa cells transfected or not with GFP-Bax using transmission electron microscopy (Fig. 8.11a). The embedding and imaging of the cells were done by the Electron Microscopy Core Facility at the University of Tübingen.

After 3h treatment with STS, cells presented the typical apoptotic phenotype with swollen endoplasmic reticulum and reorganized mitochondrial cristae. In both cases, we detected events of MOM disruption, which exhibited sizes in the same order of magnitude as the Bax structures identified in the superresolution images. These pores or defects were absent in the MOM of control healthy HeLa cells.

Additionally, we aimed to correlate the localization of GFP-Bax with the

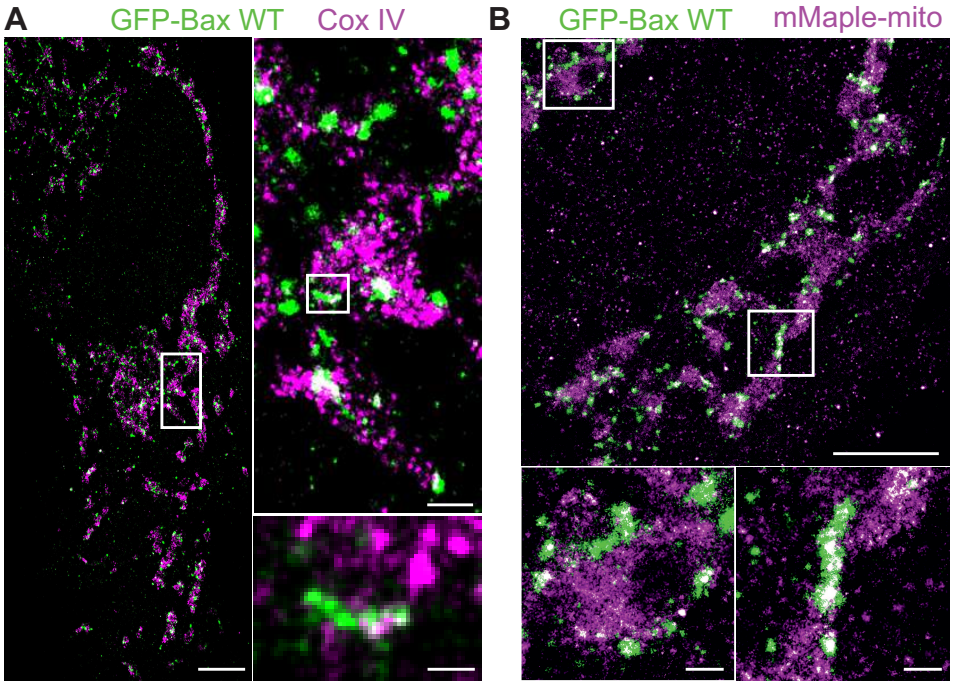

Figure 8.10. Super-reolution SMLM: Bax non-random structures at apoptotic mitochondria. (A) Reconstructed dual-color superresolution image of GFP-Bax overexpressing HeLa cells immunosstained with Af647-anti-GFP-nanobodies and with CoxIV (primary) and CF680 (secondary) antibodies (used as a mitochondria staining). Image was acquired 3h after STS treatment. Left panel shows the cell overview (scale bar, 5 μm), right panel up shows the overview inset (scale bar, 500 nm) and right panel down shows a non-random linear GFP-Bax assembly at mitochondria (scale bar, 100 nm). (B) Reconstructed dual-color superresolution image of HeLa cells co-overexpressing mMaple-mito and GFP-Bax and stained with Af647-anti-GFP-nanobodies. Image was acquired 3h after STS treatment. Lower panel shows enlarged insets corresponding to the white rectangles in the upper panel. Scale bars, 1 μm (overview) and 100 nm (insets)

pores on the MOM. For that, we used Mini-SOGs (mini Singlet Oxygen Generator) tagged to GFP-Bax, a label for correlated light and electron microscopy. Although the Mini-SOG precipitates were too big to discern if Bax was delineating the MOM openings, we could observe that GFP-Bax Mini-SOG acumulated selectively on apoptotic mitochondria, while healthy mitochondria did not show large Mini-SOG precipitates (Fig. 8.11b). These results provide another indication about Bax translocation and specific localization at apoptotic mitochondrial foci.

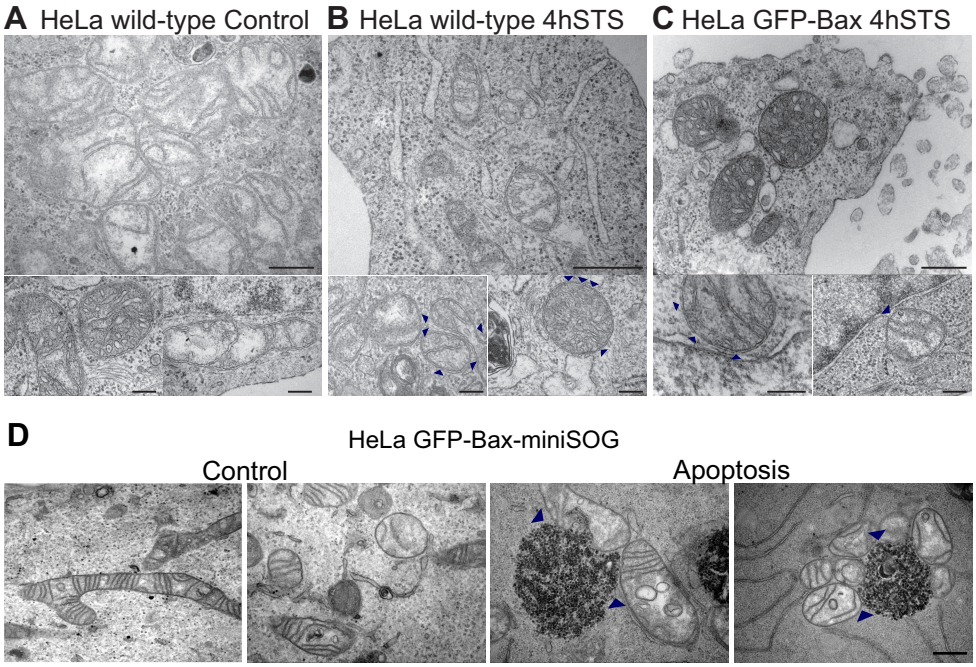

Figure 8.11. Transmission electron microscopy reveals MOM openings in apopotic mitochondria. (A-C) Representative TEM pictures of HeLa wild-type and GFP-Bax overepressing cells with and without STS treatment (1 μM). Scale bars, 500 nm (overview) and 200 nm (zooms). (C) Representative TEM pictures of HeLa GFP-Bax-miniSOG overexpressing cells (control and 4 h after STS treatment. Blue arrowheads point to miniSOG precipitates. Scale bars, 500 nm.

8.7. AFM demonstrates that full rings and arc-shaped assemblies of Bax perforate the membrane

To investigate if the oligomeric arrangements of Bax detected in apoptotic cells by super-resolution microscopy were related to pore formation, we performed experiments of atomic force microscopy (AFM). In addition to a high spatial resolution, this technique also provides information about the 3D topography of the membrane surface. The AFM experiments were performed by a colleague, Dr. Katia Cosentino. For this purpose, we prepared supported lipid bilayers from proteoliposomes containing activated, membrane-bound Bax and we analyzed them with AFM. In contrast to control samples, which exhibited largely flat membranes with few defects, the supported lipid bilayers containing activated Bax were rich in structures protruding 3.97 ± 1.02 nm from the membrane plane that corresponded most likely to Bax clusters (Fig. 8.12a,b). Interestingly, the higher structures in the samples with Bax had the same structural organization as the GFP-Bax clusters in the SMLM experiments, and were also heterogeneous in size

	Arcs (radius)	Lines (length)	Rings (radius)
SMLM	73±30	214±80	34±7
AFM	86±40	249±110	32±4

Table 8.1. Size comparison of Bax non-random structures between SMLM and AFM. Units in nm

and shape. They also included lines, rings and arc-shaped arrangements of protein in addition to random dots and aggregates.

For consistency, we performed the same analysis of the AFM images for the non-random assemblies as with the super-resolution images. As shown in Fig. 8.12d and Table 8.1, not only the size of the structures but also their distribution were in very good agreement with the SMLM results (Fig. 8.5). This strongly suggests that the defined architectures detected in both cases were alike. Importantly, we were able to visualize membrane pores associated with defined structures in the samples containing Bax (Fig. 8.12a,b). These pores were also heterogeneous in size and shape, but generally round with diameters ranging from around 24 to 176 nm and appeared as steep depressions of 3.85 ± 0.47 nm with respect to the flat surface of the lipid bilayer, which fits well with the membrane thickness. They were characterized by the presence of higher structures, congruent with Bax molecules distributed along the pore rim. Concretely, 97% of complete rings that we could resolve contained a pore in the interior. In the case of arc-shaped assemblies, 12% of them were also associated with membrane pores, where Bax molecules covered only a fraction of the pore rim and the rest corresponded to naked lipid bilayer. These results provided a functional link to the non-random Bax structures.

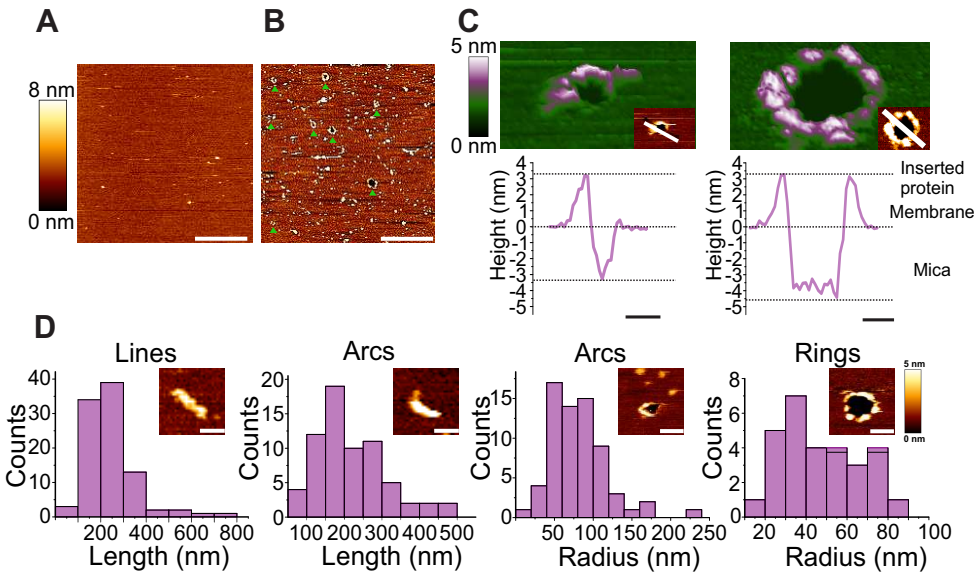

Figure 8.12. Full rings and arcs of Bax are associated with membrane pores. (A) AFM image of a control SLB prepared from LUVs with a mitochondrial-like lipid composition. The bilayer looks flat, without aggregates or defects. Scale bar, 1 μm. (B) AFM image of a SLB prepared from LUVs with a mitochondrial-like lipid composition pre-incubated with heat-activated Bax. The green arrows indicate the presence of membrane pores, which are heterogeneous in size and shape. The edges of the pores present protrusions corresponding to Bax clusters. Scale bar, 1 μm. (C) 3D AFM topography of a Bax arc (left) and ring (right). Both images reveal a circular dark hole that spans the lipid membrane (green). Bax molecules around the pore rim (magenta and white) protrude 3.97 $\pm$ 1.02 nm above the membrane plane, as confirmed by the height profiles shown below each image (corresponding to the white line in the 2D image insets). The topography of the arc structure reveals a pore only partially surrounded by Bax molecules, while lipids alone form the rest of the pore rim. Images are shown in a 42 °C tilted representation. (D) Quantitative analysis of the distinct structures found for activated Bax on SLBs. Data show the total number of structures in all the measurements. If not differently specified, the scale bar in all the images is 100 nm.

9 Interplay between Drp1 and Bcl-2 proteins

9.1. Dual-color single-molecule localization microscopy: colocalization of Bax and Drp1 at mitochondrial foci during apoptosis

Several studies have proposed a functional interplay between the Bax and Drp1 when they promote MOM permeabilization and mitochondrial fragmentation during apoptosis (Montessuit et al., 2010; Frank et al., 2001). Moreover, Bax and Drp1 have been shown to colocalize at the same discrete foci on the mitochondria of apoptotic cells using confocal imaging (Karbowski et al., 2002; Wasiak et al., 2007). However, the resolution limit of ∼200 nm in traditional optical microscopy does not allow one to know if, at the molecular level, both proteins are in contact, organizing next to each other or several nanometers apart, for example forming part of a larger supramolecular structure formed at the mitochondrial foci.

In order to check if the non-random assemblies of Bax indeed correlated with Drp1 distribution on mitochondria also at the nanoscale, we investigated the distance between Drp1 and GFP-Bax structures during apoptosis by two-color SMLM. Endogenous Drp1 was tagged with anti-Drp1-cf680 antibodies in HeLa cells overexpressing GFP-Bax, which was labeled with AF647–anti-GFP nanobodies after STS treatment. As shown in Fig. 9.1a, Drp1 is also heterogeneously distributed in a dotted manner within the cell, presumably at mitochondria. Moreover, we could also observe non-random structures of Drp1 (Fig. 9.1b). However, we could not detect as many of them as with GFP-Bax, probably due to the lower labeling densities achieved with the conventional anti-Drp1 antibody.

As expected, most of Drp1 structures appeared together with or next to GFP-Bax. Here it is important to note that, unlike with traditional fluorescence microscopy, the resolution limit is in the order of the molecular size of the structures analyzed and as a consequence, colocalizing signals often do not appear superimposed to each other. Therefore, to analyze how close the two proteins were and if there was a trend for them to be placed next to each other, we calculated the distance between all the detected GFP-Bax and Drp1 structures that had more than 100 localizations (to ensure that they did not correspond to arbitrary single antibodies). We chose a threshold for colocalization at 30nm, due to the limit in resolution of SMLM. Taking

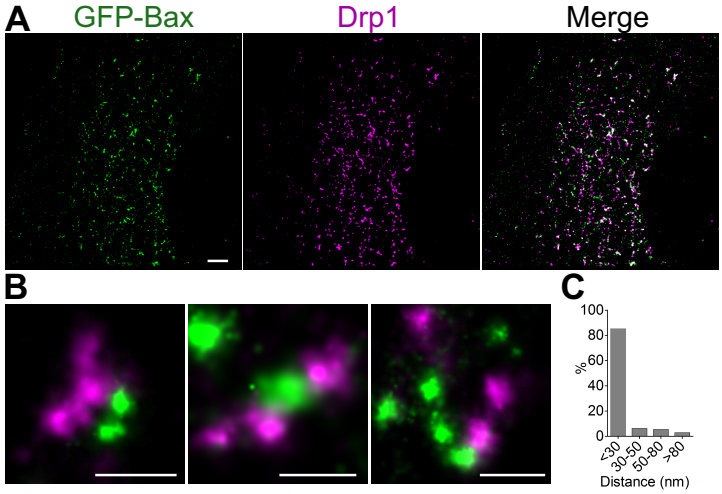

Figure 9.1. Dual color single molecule localization does not reveal a significant separation between Bax and Drp1. (A) Reconstructed dual super-resolution image of GFP-Bax WT overexpressing HeLa cells stained with AF647-anti-GFP-nanobodies and Drp1 cf680 antibody. Image was acquired 3 h after STS treatment. Scale bar, 2 μm (B) Magnified reconstructed superresolution images show GFP-Bax WT and Drp1 assemblies close to each other during apoptosis. Scale bar, 100 nm (C) Quantification of the distances between GFP-Bax WT and Drp1 structures on SMLM.

this into account, approximately 80% of the Bax/Drp1 signal was located less 30 nm apart, 20% of the structures were positioned at distance from 30 to 80 nm and only 5% were more than 80 nm apart. Altogether, these observations showed that, within a spatial resolution of 30 nm, GFP-Bax and Drp1 assemblies colocalized on the surface of apoptotic mitochondria. Considering the size of the resolved spot and that both proteins are forming high order oligomers, likely of the order of tens of nanometers each, these results also suggest that, under the conditions studied, Bax and Drp1 are very close if not in direct contact with each other.

9.2. FCCS: Drp1 binding to Bax and Bcl-xL

9.2.1. Bax and Drp1 interact in lipid membranes

To check if there is direct binding between Bax and Drp1, we used a cell-free reconstituted system with purified recombinant proteins, fluorescently labeled with Atto488 ($Drp1_G$) or Alexa633 (Bax_R). Then, we examined if these two proteins can directly interact by using FCCS in solution and in the membrane of giant unilamellar vesicles (GUVs).

GUVs are lipid vesicles of several micrometers in diameter that can be directly visualized by optical microscopy. sFCS can be applied on these liposomes, which makes them a very helpful system to study potein/protein

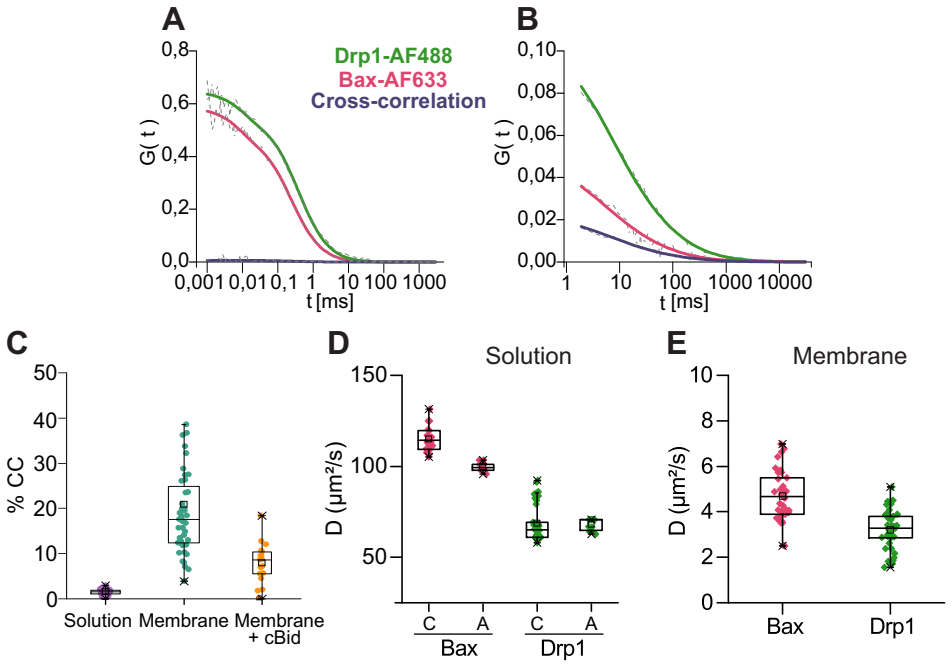

Figure 9.2. Drp1 interacts with Bax in lipid membranes. (A) Representative auto- and cross-correlation analysis of solution FCCS between $Drp1_G$, Bax_R. (B) Representative auto- and cross-correlation analysis of sFCCS between $Drp1_G$, Bax_R in the membrane of GUVs. Dash gray lines depict raw data. (C) Box plot for the percentage of cross-correlation measured between $Drp1_G$ and Bax_R in solution, in membrane, and in membrane with the presence of an excess of unlabeled cBid. GUV composition was DOPC:CL:PE (54:26:20) . (D) Diffusion coefficients calculated for Bax and Drp1 in the complex (C) and alone (A) in solution. (E) Diffusion coefficients calculated for Bax and Drp1 in the complex in GUVs.

interactions in membranes. We activated Bax by mild heat (42 °C) and included 0.1 mM GTP in the protein mixture to enhance Drp1 oligomerization and mimic its physiological function in mitochondrial fission.

In solution, point FCCS measurements gave rise to the autocorrelation curves in Fig. 9.2a, but no positive cross-correlation was observed, indicating that Bax and Drp1 do not associate in the aqueous environment.

Both proteins exert their main function when they insert in the mitochondrial membrane, where they are in an active, oligomerized conformation. To check the active role of the lipid membrane in Bax-Drp1 complex formation, we measured two-color two-focus scanning FCS (sFCCS) in giant unilamellar vesicles (GUVs). We added $Drp1_G$, Bax_R, and GTP to a suspension of GUVs composed by 1,2-Dioleoyl-sn-glycero-3-phosphocholine (DOPC), heart cardiolipin (CL), and Egg L-α-phosphatidylethanolamine (PE) (54:26:20). After 30 min incubation at 42 °C, we measured sFCS in single GUVs containing the bound proteins, specifically across the vesicle equator. As shown in (Fig. 9.2b), $Drp1_G$ and Bax_R formed complexes in lipid membranes, as seen by the positive amplitude of the cross-correlation curve. We detected a broad

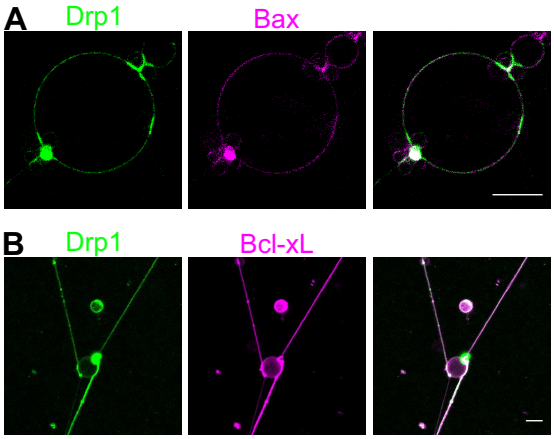

Figure 9.3. Drp1 induces vesicle tubes and tethering, colocalizing with Bax and Bcl-xL. (A) Representative GUV with bound $Drp1_G$ (green) and Bax_R (magenta). White regions represent colocalization. (B) Representative GUV with bound $Drp1_G$ (green) and $Bcl\text{-}xL_R$ (magenta).

distribution of cross-correlation percentages (21 ±14%, ±s.d.), which likely indicates heterogeneities in the extent of association in the different GUVs (Fig. 9.2c. From the respective autocorrelation curves, we calculated the diffusion coefficients for both proteins. In solution, Drp1 clearly diffused slower than Bax (69±9 and 122±5 $\mu m^2 s^{-1}$, respectively) but the diffusion coefficients measured in the samples with the presence of both proteins was very similar to that of the protein alone in solution (99±2 $\mu m^2 s^{-1}$ for Bax and 68±3 $\mu m^2 s^{-1}$ for Drp1), in line with the lack of complex formation in the aqueous environment (Fig. 9.2d). When Bax and Drp1 were forming complexes in membranes, we calculated diffusion coefficient that were one order of magnitude slower (4±1 $\mu m^2 s^{-1}$ for Bax and 3±1 $\mu m^2 s^{-1}$ for Drp1), as expected (Fig. 9.2e).

Importantly, we could observe that Drp1 binding to the GUVs induced tubulation and vesicle tethering, as expected. Bax colocalized partially with Drp1 in the GUVs. It bound extensively to the same regions of vesicle tethering as Drp1, but only faintly to the tubes (Fig. 9.3a).

Bax activation is regulated by the BH3-only protein Bid. In the presence of cleaved Bid (cBid), Bax exhibits pore fomation *in vitro* without altering vesicle integrity. Strikingly, cBid-induced Bax oligomerization is enhanced by Drp1 (Montessuit et al., 2010). To evaluate if cBid could affect Drp1-Bax interactions in membranes, we added an excess of non-fluorescent cBid to the GUV mixture containing $Drp1_G$ and Bax_R. Strikingly, as shown in Fig. 9.2c, cBid addition lead to a decrease in the cross-correlation from an average of 21±14 % to 8±4 %. These results indicate that cBid competes for the interaction between $Drp1_G$ and Bax_R, or that cBid-induced Bax activation alternatively precludes interaction.

9.2.2. Drp1 interacts with Bcl-xL

The anti-apoptotic protein Bcl-xL inhibits Bax activation and disrupts Bax homo-oligomers (Antonsson, 2001; Subburaj et al., 2015). If membrane remodeling by Drp1 helps Bax oligomerization and Bcl-xL disrupts the oligomers, we wondered if Bcl-xL may also form complexes with Drp1. To check this, we incubated Bcl-xL labeled with Alexa 647 (Bcl-xL$_R$) and Drp1$_G$ with a mixture of GUVs composed by DOPC:CL:PE (54:26:20).

Interestingly, in this case the proteins did not need to be previously activated to bind to the GUVs, and we observed that both proteins colocalized on the Drp1-induced tubes as well as at the tethering regions (Fig. 9.3b). These observations suggest that Drp1 and Bcl-xL induce each other's binding to membranes. In order to detect interactions *in vitro*, we measured FCCS in solution and in membranes between Drp1$_G$ and Bcl-xL$_R$. After 15 min incubation at room temperature, we could already detect cross-correlation between Drp1$_G$ and Bcl-xL$_R$ in solution (Fig. 9.4a). sFCCS measurements revealed that Drp1$_G$ and Bcl-xL$_R$ also interacted in membranes, with a similar percentage as in solution (20±9 % in solution and 19±9% in membranes).

We deduced diffusion coefficients in solution of 30±9 $\mu m^2 s^{-1}$ (Bcl-xL$_R$) and of 27±9 $\mu m^2 s^{-1}$ (Drp1$_G$) (Fig. 9.4b). Both proteins diffused slower compared to the individual proteins (68±3 $\mu m^2 s^{-1}$ for Drp1 and 86±5 $\mu m^2 s^{-1}$for Bcl-xL). As the diffusion coefficient depends on the hydrodynamic radius of the proteins, this decrease in mobility indicates that both proteins were forming a bigger complex under these conditions. The mean diffusion coefficient of Drp1$_G$ and Bcl-xL$_R$ in membranes was 4±1 $\mu m^2 s^{-1}$ (Fig. 9.4c), in line with previous work (Bleicken et al., 2013; García-Sáez et al., 2009). In this case, the diffusion coefficients between the proteins in the complex and alone were similar. This weak effect is explained by the fact that the diffusion coefficient in the two-dimensional membrane is related to the logarithm of the protein's hydrodynamic radius.

As with Bax, addition of an excess of non-fluorescent cBid led to a decrease in cross-correlation between Drp1$_G$ and Bcl-xL$_R$ in membranes to 8±6 %. These data not only pinpoint a direct interaction between Drp1$_G$ -Bcl-xL$_R$, but also show that the complex can be disrupted by cBid at the membrane level.

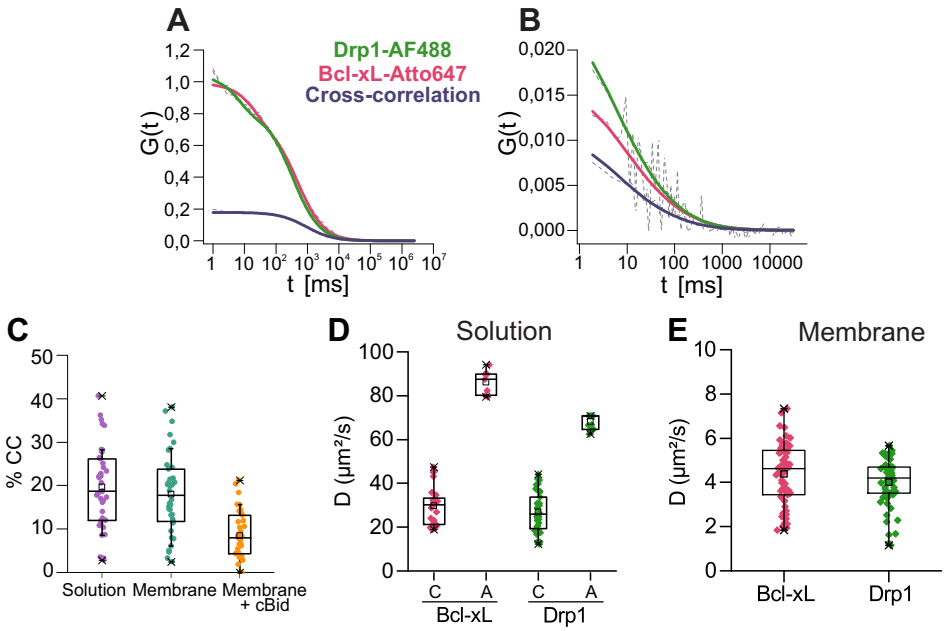

Figure 9.4. Drp1 interacts with Bcl-xL in solution and in membranes. (A) Representative auto- and cross-correlation analysis of solution FCCS between $Drp1_G$, $Bcl\text{-}xL_R$. (B) Representative auto- and cross-correlation analysis of sFCCS between $Drp1_G$, Bax_R in the membrane of GUVs. Dash gray lines depict raw data. (C) Box plot for the percentage of cross-correlation measured between $Drp1_G$ and $Bcl\text{-}xL_R$ in solution, in membrane, and in membrane with the presence of an excess of unlabeled cBid. GUV composition was DOPC:CL:PE (54:26:20). (D) Diffusion coefficients calculated for Bcl-xL and Drp1 in the complex (C) and alone (A) in solution. (E) Diffusion coefficients calculated for Bax and Drp1 in the complex in GUVs.

Part IV.

Discussion and conclusions

10 Discussion

In this thesis, we have characterized the supramolecular organization of active Bax oligomers involved in mitochondrial outer membrane permeabilization during apoptosis. We provide the first single and dual-color superresolution microscopy study of a Bcl-2 homolog in single cells to yield insight into the organization of the pro-apoptotic protein Bax in mitochondria and its association with a fission mediator protein, Drp1. The work is complemented with *in vitro* single-molecule studies on the characterization of this interplay.

10.1. Bax assembly into rings and arcs in apoptotic mitochondria is linked to membrane pores

This work reports the assembly of Bax oligomers into a distribution of rings and arc-shaped structures in the mitochondria of apoptotic mammalian cells. Based on the ability of these structures to form pores in pure lipid bilayers, we propose a new molecular mechanism for Bax-mediated MOM permeabilization during apoptosis (Salvador-Gallego et al., 2016).

The cellular distribution of Bax is dynamic. In healthy cells, the protein is diffusely located in the cytosol. Upon apoptosis induction, homogeneous Bax signal appears initially at the MOM, which then evolves into discrete mitochondrial foci that correlate with loss of mitochondrial potential, while still coexisting with cytosolic protein. This is in line with previous work that suggested that in single cells only minimal gathering of Bax is needed to burst mitochondria depolarization and fragmentation (Düssmann et al., 2010). In the final steps, total translocation of Bax to the MOM is achieved (Zhou and Chang, 2008).

We have studied the supra-molecular structure of active Bax in apoptotic cells by two superresolution techniques, SMLM and STED. In SMLM, only a portion of the fluorophores are stochastically activated at the same time and then precisely localized. After the accurate localization of all the molecules, the superresolution image can be reconstructed. The working principle of STED is different from SMLM: it is based on the overlay of a diffraction-limited spot with a doughnut-shaped laser which depletes the fluorescence everywhere in the focal region but in the very center of the spot (Hell and Wichmann, 1994). As a result, the fluorescence emission is confined to a very small region.

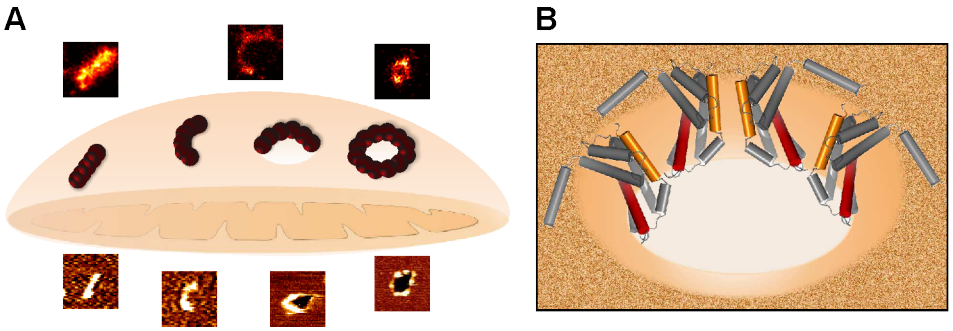

Figure 10.1. (A) Illustration of the possible roles for the Bax non-random assemblies revealed by SMLM and AFM during apoptosis. Linear and arc clusters not perforating the membrane could correspond to Bax at initial stages of gathering on healthy mitochondria. They would evolve towards opening of membrane pores, where the protein is covering completely (full rings) or partially (arcs) the pore rim. We cannot exclude that a fraction of the linear and arc-shaped assemblies correspond to Bax pores observed from different perspectives. The number of red spheres (Bax dimers) is illustrative and does not need to correlate with the actual number present in the structures. (B) The mechanism by which Bax permeabilizes the membrane is mainly by releasing the curvature stress at the membrane edge. Full as well as partial coverage of the pore rim by Bax molecules could reduce line tension enough to stabilize the open pore state. The illustration shows an incomplete ring assembly of active Bax dimers adopting a clamp-like structure at the pore interface (Bleicken et al., 2014).

To achieve the best performance with SMLM, we minimized the background cytosolic GFP-Bax signal to optimize the contrast of GFP-Bax signal at mitochondria and subsequent image reconstruction. Thus, we visualized a specific apoptotic stage, when Bax had completely translocated to the MOM, induced loss of mitochondrial potential and, presumably, release of cytochrome c, but before cells rounded-up as a result of the dismantling of the cellular components due to caspase activity.

The SMLM superresolution microscopy data showed a significant fraction of GFP-Bax signal localized at discrete foci along mitochondria and organized into distinct architectures, classified as full rings, arcs and lines. These were characterized by a wide distribution of sizes, with rings in the order of 50 to 100 nm in diameter. Moreover, we detected comparable structural arrangements of activated Bax using STED microscopy in apoptotic cells and in supported lipid bilayers using AFM imaging.

Importantly, the physiological relevance of the Bax structures reported here is sustained by the differences in assembly observed for the inactive mutant GFP-Bax 1-2/L-6, which is constitutively located at the MOM of healthy cells. Although confocal microscopy gives rise to similar images when transfecting both constructs, the differences become prominent when the structures are analyzed by SMLM. Aggregates and dots are considerably smaller, in good agreement with the lower tendency of the mutant version of GFP-Bax to oligomerize. In addition, the lower amount of non-random

structures detected reflects the tendency of WT GFP-Bax to arrange into specific assemblies, in contrast with the mutant.

The assembly of GFP-Bax into full as well as incomplete rings at the MOM reported here supports a molecular mechanism in which the pore structures formed by Bax in apoptotic mitochondria are lined by both lipids and proteins, where the latter may or not cover the full pore rim (Fig. 10.1a). The AFM images confirmed this pore formation hypothesis, showing that rings and a fraction of the arc assemblies pierced the membrane.

We cannot discard the presence of smaller Bax assemblies associated with pores that are below the resolution limit inherent to the techniques. This is around 20 nm for SMLM and between 20 to 45 nm for AFM under our specific experimental conditions (nominal tip radius of 20 nm). These results demonstrate that lipids directly participate in the pore architectures formed by Bax and that the protein molecules can partially or totally outline the pore edge.

To our knowledge, this is also the first direct evidence that Bax oligomers delineate membrane pores. Furthermore, these findings strongly suggest that the Bax structures identified at mitochondria are directly involved in MOM permeabilization via direct pore formation.

Recently, another 3D super-resolution study revealed that Bax rings are empty of fluorescent mitochondrial markers, also supporting the model of Bax pore formation (Große et al., 2016). Bax rings were detected in mitochondrial regions where cyt c was not yet released, suggesting that cyt c release needs additional steps besides Bax pore formation. It is likely that the overall mitochondrial reorganization happening during apoptosis includes important processes for this release (Scorrano et al., 2002; Prudent et al., 2015; Große et al., 2016).

Previous in vitro studies with cryo_EM reported the opening of pores induced by Bax on purified MOMs (Gillies et al., 2015). The transmission EM data on mammalian cells shown in this work provide the first evidence for the existence of these pores in the mitochondria of apoptotic cells. As the mitochondria of healthy cells appeared intact, these results support the role of the GFP-Bax assemblies identified here in the formation of pores at the MOM of apoptotic cells.

Bax arrangements were characterized by a wide distribution of shapes and sizes, which argues in favor of a non-uniform organization of Bax oligomers at the MOM. In agreement with our findings, Bax pores ranging from 3.5 to several hundreds of nanometers (Xu et al., 2013; Bleicken et al., 2010) as well as multiple types of Bax aggregates (Annis et al., 2005; Tan et al., 1999; Antonsson, 2001) have been previously described. This heterogeneity is in contrast with the results obtained for the nuclear pore (Szymborska et al., 2013) or for other pore-forming proteins (Metkar et al., 2015; Sonnen et al., 2014), which revealed highly homogeneous structures, and precluded further modeling of the Bax pore structure by averaging approaches.

Altogether, our structural data support a model by which Bax assembles

into a flexible toroidal pore structure able to change in size depending on Bax density in the membrane (Bleicken et al., 2013). This model would explain the different sizes of the pores and oligomers formed by Bax (Bleicken et al., 2013; Fuertes et al., 2010; Kuwana et al., 2002) without discarding that additional proteins like Bak or other unknown factors, not detected here, could also be forming part of the pore structure.

Most of the Bax signal detected with SMLM corresponded to random, undefined clusters, from which no specific molecular organization could be distinguished. This could be related to partial labeling with the nanobodies, insufficient spatial resolution due to out of focus effects, orientation of the structure with respect to the observation plane, or simply no supra-organization of a fraction of Bax oligomers at the nanometer scale. Along these lines of reasoning, it is important to consider that the variety of defined Bax structures including lines, arcs and rings, could correspond to the same type of supramolecular organization observed from different angles or with different degrees of assembly.

On the one hand, in the case of complete rings and arcs, only those which are observed perpendicular to the ring/arc plane would be detected as such in the two dimensional SMLM approach used here, while any other orientation would likely appear as a line, or less likely due to off-focus blurring, as an ellipse. Within the cell, the tubules of the mitochondrial network can adopt all possible orientations, where the longer tubes have a preference for those orientations best adapting to the cellular shape. As a result, it is unlikely that most of Bax rings and arcs would be detected and classified as such, which is in agreement with the lower frequency of these structures in comparison with lines. Besides, the length of lines and arcs is in the same range as the diameter of the full rings, taking into account the variations in the size of the different structures observed, which would also support this possibility.

On the other hand, lines, arcs, and rings could represent different stages in the assembly of nascent evolving Bax pores. In this scenario, Bax molecules would first organize into linear and arc-shaped structures and some of them would evolve into complete rings. It could also be that lines and arcs correspond to kinetically trapped intermediates in the process of full ring assembly. Interestingly, the AFM data in supported bilayers, where both rings and arc-shaped assemblies of Bax coexist with the same orientation with respect to the membrane plane and are involved in pore formation, demonstrate the existence of lines, arcs, and rings as distinct structures of Bax oligomers. Nevertheless, both situations are not mutually exclusive, and it is conceivable that the structures detected in apoptotic mitochondria correspond to a mixture of different assembly stages observed from different orientations.

Our finding that not only full rings but also arc-shaped Bax assemblies form membrane pores has unanticipated implications for the molecular mechanism how Bax permeabilizes the MOM in apoptosis (Fig. 10.1a).

Stabilization of toroidal pores requires a decrease in the line tension associated with the extremely high membrane curvature generated at the pore edge (Karatekin et al., 2003). In agreement with this, a peptide derived from helix 5 of Bax, which reproduces the pore activity of the full-length protein, is able to reduce line tension at interfaces with high curvature stress (García-Sáez et al., 2005, 2007). In this scenario, both full and partial coverage of the pore boundary by protein molecules could provide enough line tension reduction to stabilize the open pore state.

Recent studies with pore-forming toxins of the membrane attack complex perforin cholesterol-dependent cytolysin superfamily, which also form toroidal pores but based on β-structural elements, report the involvement of both complete rings as well as arc-shaped oligomeric assemblies in pore formation (Gilbert et al., 2014; Leung et al., 2014; Metkar et al., 2015; Sonnen et al., 2014; Stewart et al., 2015). Incomplete coverage of the pore rim has also been observed for Bax monomers in lipid nanodiscs (Xu et al., 2013).

Based on this, we propose that the physical-chemical principle by which Bax stabilizes membrane pores is not by building a poly-peptide wall that buries the hydrophobic membrane core, but rather by releasing the curvature stress at the membrane edge (Ros and García-Sáez, 2015). The set of architectures of Bax oligomers in apoptotic mitochondria and their relationship to pore formation demonstrated here support a new molecular mechanism of Bax during apoptosis (Fig. 10.1a).

Upon activation, Bax would accumulate in mitochondria, where it would undergo a conformational change accompanied by extensive membrane insertion (Annis et al., 2005; García-Sáez et al., 2004). Bax molecules would then stably associate via their dimerization domain (Aluvila et al., 2014; Bleicken et al., 2010, 2014; Czabotar et al., 2013; Dewson et al., 2008, 2012; Subburaj et al., 2015; Zhang et al., 2010) and continue to self-assemble into larger oligomers, which might contain Bak or other MOM proteins (Zhou and Chang, 2008). These oligomers would initially organize as linear and arc-shaped structures, some of which would induce the opening of MOM pores responsible for the release of the apoptotic factors. In order to stabilize these pores, Bax oligomers would partially delineate the pore edge in a "clamp" conformation (Bleicken et al., 2014) (Fig. 10.1b). Incorporation of additional Bax molecules into the pore structures would then lead to the formation of full Bax rings and to pore growth.

In summary, this work reports the supramolecular organization of Bax oligomers at mitochondria of apoptotic cells with unprecedented detail and the ability of ring and arc-shaped Bax assemblies to perforate lipid membranes.

10.2. Interplay between mitochondrial permeabilization and fission

Mitochondria undergo massive fragmentation under apoptotic conditions, which happens close in time with Bax-mediated MOM permeabilization (Brooks et al., 2011). Active Bax accumulates at specific sites on the MOM where fragmentation has happened or is about to happen, colocalizing with Drp1 (Karbowski et al., 2002). Drp1 is a dynamin-like GTPase that has been proposed to mediate mitochondrial fragmentation via the formation of constrictive tubular or spiral-like scaffolds around the mitochondrial perimeter.

Despite achieving a lower resolution for Drp1 due to the lower performance of the dye cf680 compared to alexa647, we found some non-random structures, mainly shaped as lines, which would agree with the formation of one ring around mitochondria and are comparable to those reported in a recent superresolution study of Drp1 (Rosenbloom et al., 2014). The identification of few GFP-Bax double-line assemblies would also support the possibility that in some cases two Drp1 rings could wrap mitochondria. Remarkably, a similar organization has been proposed for dynamin during vesicle neck scission (Chen et al., 2004).

We also found that active Bax and Drp1 assemblies are very close to each other, in the order of a few tens of nanometers, and have a similar shape and size. This provides a structural basis for the functional interplay between these two proteins. It is tempting to speculate that the Drp1 scaffold could contribute to the supra-molecular organization of Bax at the MOM. Bax oligomers could assemble as full or incomplete rings along the Drp1 assemblies, thus wrapping mitochondria. The different lengths measured for Bax linear assemblies fit well to the diameter of healthy or constricted mitochondria, respectively. On the other hand, the reported diameter for constricted mitochondria and the size of Drp1 helices is approximately 100-150 nm in yeast and *in vitro* (Ingerman et al., 2005; Mears et al., 2011; Friedman et al., 2011), which is comparable to the length of the shorter population of lines. A similar hypothesis can be applied to the two well-defined populations of arcs, which could accommodate well either in the constriction sites or at the mitochondrial tips. In that case, Bax would be able to collaborate with Drp1 to promote MOM permeabilization and/or mitochondrial fragmentation.

Along these lines, Drp1 deficient cells, besides presenting elongated mitochondria also show delayed cyt c release in apoptosis (Große et al., 2016). Moreover, the Drp1 adaptors MiD49/51 play an active role in cristae remodeling during intrinsic apoptosis, a requisite for cytochrome c release (Otera et al., 2016). In contrast to some reports in the literature arguing that inhibition of mitochondrial fission or Drp1 knock-out can lead to little or partial resistance to apoptosis (Wakabayashi et al., 2009; Ishihara et al., 2003), growing evidence supports a direct role of the fission machinery in

mitochondrial permeabilization, and, consequently, in apoptosis regulation. Our findings shed light on the nature of this interplay. Besides the close proximity between Drp1 and Bax in apoptotic cells, here we found direct complex formation between the two proteins in lipid membranes at the single molecule level. The lack of interaction in solution suggests that the membrane environment is needed for Bax and Drp1 interplay, consistent with the active role of the membrane proposed for the activation and function of Bcl-2 proteins (García-Sáez et al., 2009; Llambi et al., 2011; Lovell et al., 2008; Bleicken et al., 2013).

In order to achieve Bax binding to the GUVs and to investigate Bax and Drp1 interaction at the vesicle level, we needed to activate the protein by mild heat. This indicates that Drp1 alone is not sufficient to activate Bax, contrary to cBid. This is in agreement with previous observations by Montessuit et al. showing that Drp1 could only enhance Bax oligomerization once it was already activated by cBid (Montessuit et al., 2010).

Moreover, cBid decreased the cross-correlation between Drp1 and Bax on membranes, suggesting that it can compete for such interactions. It is known that cBid binding to membranes induces Bax oligomerization and activation (Bleicken et al., 2013). In this scenario, one possibility for Drp1-Bax complex disruption by cBid could be the competition of cBid and Drp1 for the same binding site in Bax. However, we cannot discard that cBid induces a conformation of Bax that is not able to interact with Drp1.

Mechanistically, Drp1 likely induces membrane hemifusion intermediates at sites enriched with cardiolipin, a lipid specific of mitochondria and with intrinsic monolayer curvature. Drp1 binding to GUVs also promotes tubulation and vesicle tethering, as part of its membrane remodeling function (Montessuit et al., 2010; Ugarte-Uribe et al., 2014; Stepanyants et al., 2015; Bleicken et al., 2016). In this work, we could reproduce Drp1-induced tubulation and vesicle tethering in free standing bilayers, using Drp1 protein purified without any tag.

Besides promoting tBid-induced Bax oligomerization (Montessuit et al., 2010), such Drp1-induced non-bilayer structures could contribute to Bax-induced MOM permeabilization by lowering the energy required for toroidal pore formation and stabilization. On these grounds, Bax and cBid induce membrane budding and vesicle tethering, and they both bind predominantly to the highly curved membranes at the neck of the bud (Bleicken et al., 2016), which strongly supports our hypothesis. Indeed, we observed that heat-activated Bax also binds to this specific lipidic regions in presence of Drp1. The likely preference for Bax to form pores at those sites could also play a role on its non-random localization along the mitochondria due to the restricted amount of those intermediates along the membrane.

Moreover, mitochondrial fragmentation involves a process of membrane fission, for which the opening of a pore has been proposed to be a structural intermediate (Kozlovsky and Kozlov, 2003). The stabilization of pore structures by Bax at the mitochondrial fission sites could also contribute to

lowering the energy for membrane fission and to Drp1-mediated mitochondrial fragmentation.

Bcl-xL has an opposing role to Bax in apoposis. In addition to inhibiting cBid/Bax pore formation, it hinders vesicle budding and fusion (Bleicken et al., 2016). Bax inhibition by Bcl-xL can happen at different levels: (1) via tBid binding to block Bax activation by this protein (García-Sáez et al., 2009; Bleicken et al., 2013), (2) by disrupting Bax homo-oligomers at the membrane (Subburaj et al., 2015), (3) by re-translocating Bax from the MOM to the cytosol (Todt et al., 2013; Edlich et al., 2011), and (4) by impairing its effect on stabilizing curved membranes (Bleicken et al., 2016).

On the other hand, membrane remodeling by Drp1 contributes to Bax oligomerization, so it is not trivial to think that Bcl-xL could localize at the same mitochondrial foci as Bax and Drp1 during mitochondrial fragmentation and contribute to Bax inhibition also by affecting Drp1 remodeling function. The interaction between of Bcl-xL and Drp1 in GUVs detected here pinpoints a direct association between this two proteins at the membrane level. Interestingly and similarly to Bax, Bcl-xL concentrated in highly curved vesicle regions, and cBid was also able to decrease Drp1-Bcl-xL interactions. Taking this into account, one could argue for a similar scenario of cBid inhibition as the one speculated for Bax. However, unlike Bax, Bcl-xL is also able to form complexes with Drp1 in solution. This could represent an additional mechanism for Bax inhibition by Bcl-xL, through the impairment of Drp1 contribution to Bax oligomerization. As Bcl-xL has already been shown to stimulate Drp1 GTPase activity (Li et al., 2008), our data also provide a step further in the understanding of Bcl-xL impact on mitochondrial fusion and fission. However, more research is still necessary before obtaining a definitive answer to the functional implications of Drp1 in Bcl-2 family regulation.

In conclusion, the close proximity to Drp1 scaffolds suggests that Bax ring and arc-shaped assemblies could contribute to the massive mitochondrial fragmentation during apoptosis. Altogether, our results shed new light on the cellular mechanism of apoptosis induction by Bax and pave the way for further characterization of the pore structures formed at the MOM during apoptosis. In addition, the data presented here support a mechanistic link between MOMP and mitochondrial dynamics.

11 Conclusions

The conclusions that can be drawn from this thesis are the following:

1. Bax assembles into non-random structures in mammalian cells, including complete rings, arcs, and lines which are related to the functional role of Bax in MOM permeabilization during apoptosis.

2. Rings and arc-shaped assemblies of Bax are able to perforate lipid membranes, providing a link of theses structures with Bax function.

3. Drp1 and Bax localize very close to each other if not completely colocalizing at discrete foci on apoptotic mitochondria.

4. Drp1 and Bax interact in vitro in lipid membranes, but not in the 3D solution. This interaction can be disrupted by cBid.

5. Drp1 is also able to form a complex with Bcl-xL both in membranes and in solution. cBid also can interfere in the complex at the membrane level.

Bibliography

Aluvila, S., T. Mandal, E. Hustedt, P. Fajer, J. Y. Choe, and K. J. Oh (2014, jan). Organization of the mitochondrial apoptotic BAK pore: oligomerization of the BAK homodimers. *The Journal of biological chemistry 289*(5), 2537–51.

Annis, M. G., E. L. Soucie, P. J. Dlugosz, J. A. Cruz-Aguado, L. Z. Penn, B. Leber, and D. W. Andrews (2005, jul). Bax forms multispanning monomers that oligomerize to permeabilize membranes during apoptosis. *The EMBO journal 24*(12), 2096–103.

Antonsson, B. (1997, jul). Inhibition of Bax Channel-Forming Activity by Bcl-2. *Science 277*(5324), 370–372.

Antonsson, B. (2001, dec). Bax and other pro-apoptotic Bcl-2 family "killer-proteins" and their victim the mitochondrion. *Cell and tissue research 306*(3), 347–61.

Ashkenazi, A. and V. M. Dixit (1998, aug). Death receptors: signaling and modulation. *Science (New York, N.Y.) 281*(5381), 1305–8.

Bacia, K., E. Haustein, and P. Schwille (2014, jul). Fluorescence correlation spectroscopy: principles and applications. *Cold Spring Harbor protocols 2014*(7), 709–25.

Bacia, K. and P. Schwille (2007, jan). Fluorescence correlation spectroscopy. *Methods in molecular biology (Clifton, N.J.) 398*, 73–84.

Baines, C. P., R. A. Kaiser, N. H. Purcell, N. S. Blair, H. Osinska, M. A. Hambleton, E. W. Brunskill, M. R. Sayen, R. A. Gottlieb, G. W. Dorn, J. Robbins, and J. D. Molkentin (2005, mar). Loss of cyclophilin D reveals a critical role for mitochondrial permeability transition in cell death. *Nature 434*(7033), 658–62.

Baines, C. P., R. A. Kaiser, T. Sheiko, W. J. Craigen, and J. D. Molkentin (2007, apr). Voltage-dependent anion channels are dispensable for mitochondrial-dependent cell death. *Nature Cell Biology 9*(5), 550–555.

Basañez, G. and J. M. Hardwick (2008, jun). Unravelling the bcl-2 apoptosis code with a simple model system. *PLoS biology 6*(6), e154.

Basañez, G., J. C. Sharpe, J. Galanis, T. B. Brandt, J. M. Hardwick, and J. Zimmerberg (2002, dec). Bax-type apoptotic proteins porate pure lipid bilayers through a mechanism sensitive to intrinsic monolayer curvature. *The Journal of biological chemistry 277*(51), 49360–5.

Basañez, G., J. Zhang, B. N. Chau, G. I. Maksaev, V. A. Frolov, T. A. Brandt, J. Burch, J. M. Hardwick, and J. Zimmerberg (2001, aug). Pro-apoptotic cleavage products of Bcl-xL form cytochrome c-conducting pores in pure lipid membranes. *The Journal of biological chemistry 276*(33), 31083–91.

Berman, S. B., Y.-b. Chen, B. Qi, J. M. McCaffery, E. B. Rucker, S. Goebbels, K.-A. Nave, B. A. Arnold, E. A. Jonas, F. J. Pineda, and J. M. Hardwick (2009, mar). Bcl-x L increases mitochondrial fission, fusion, and biomass in neurons. *The Journal of cell biology 184*(5), 707–19.

Berning, S., K. I. Willig, H. Steffens, P. Dibaj, and S. W. Hell (2012, feb). Nanoscopy in a living mouse brain. *Science (New York, N.Y.) 335*(6068), 551.

Betzig, E., G. H. Patterson, R. Sougrat, O. W. Lindwasser, S. Olenych, J. S. Bonifacino, M. W. Davidson, J. Lippincott-Schwartz, and H. F. Hess (2006, sep). Imaging intracellular fluorescent proteins at nanometer resolution. *Science (New York, N.Y.) 313*(5793), 1642–5.

Bleazard, W., J. M. McCaffery, E. J. King, S. Bale, A. Mozdy, Q. Tieu, J. Nunnari, and J. M. Shaw (1999, sep). The dynamin-related GTPase Dnm1 regulates mitochondrial fission in yeast. *Nature cell biology 1*(5), 298–304.

Bleicken, S., M. Classen, P. V. L. Padmavathi, T. Ishikawa, K. Zeth, H.-J. Steinhoff, and E. Bordignon (2010, feb). Molecular details of Bax activation, oligomerization, and membrane insertion. *The Journal of biological chemistry 285*(9), 6636–47.

Bleicken, S., G. Hofhaus, B. Ugarte-Uribe, R. Schröder, and A. J. García-Sáez (2016, jan). cBid, Bax and Bcl-xL exhibit opposite membrane remodeling activities. *Cell death & disease 7*, e2121.

Bleicken, S., G. Jeschke, C. Stegmueller, R. Salvador-Gallego, A. J. García-Sáez, and E. Bordignon (2014). Structural Model of Active Bax at the Membrane. *Molecular Cell 56*(4), 496–505.

Bleicken, S., O. Landeta, A. Landajuela, G. Basañez, and A. J. García-Sáez (2013). Proapoptotic Bax and Bak proteins form stable protein-permeable pores of tunable size. *Journal of Biological Chemistry 288*(46), 33241–33252.

Bleicken, S., C. Wagner, and A. J. García-Sáez (2013). Mechanistic differences in the membrane activity of bax and Bcl-xL correlate with their opposing roles in apoptosis. *Biophysical Journal 104*(2), 421–431.

Brenner, C. and S. Grimm (2006, aug). The permeability transition pore complex in cancer cell death. *Oncogene 25*(34), 4744–56.

Brooks, C., S.-G. Cho, C.-Y. Wang, T. Yang, and Z. Dong (2011). Fragmented mitochondria are sensitized to Bax insertion and activation during apoptosis. *American journal of physiology. Cell physiology 300*(3), C447–C455.

Brooks, C. and Z. Dong (2007). Regulation of mitochondrial morphological dynamics during apoptosis by Bcl-2 family proteins: A key in Bak? *Cell Cycle 6*(24), 3043–3047.

Brouwer, J. M., D. Westphal, G. Dewson, A. Y. Robin, R. T. Uren, R. Bartolo, G. V. Thompson, P. M. Colman, R. M. Kluck, and P. E. Czabotar (2014, sep). Bak core and latch domains separate during activation, and freed core domains form symmetric homodimers. *Molecular cell 55*(6), 938–46.

Cai, Z., S. Jitkaew, J. Zhao, H.-C. Chiang, S. Choksi, J. Liu, Y. Ward, L.-G. Wu, and Z.-G. Liu (2014, jan). Plasma membrane translocation of trimerized MLKL protein is required for TNF-induced necroptosis. *Nature cell biology 16*(1), 55–65.

Candi, E., R. Schmidt, and G. Melino (2005, apr). The cornified envelope: a model of cell death in the skin. *Nature reviews. Molecular cell biology 6*(4), 328–40.

Certo, M., V. Del Gaizo Moore, M. Nishino, G. Wei, S. Korsmeyer, S. A. Armstrong, and A. Letai (2006, may). Mitochondria primed by death signals determine cellular addiction to antiapoptotic BCL-2 family members. *Cancer cell 9*(5), 351–65.

Chauhan, D., T. Hideshima, S. Rosen, J. C. Reed, S. Kharbanda, and K. C. Anderson (2001, jul). Apaf-1/cytochrome c-independent and Smac-dependent induction of apoptosis in multiple myeloma (MM) cells. *The Journal of biological chemistry 276*(27), 24453–6.

Chen, H., S. a. Detmer, A. J. Ewald, E. E. Griffin, S. E. Fraser, and D. C. Chan (2003). Mitofusins Mfn1 and Mfn2 coordinately regulate mitochondrial fusion and are essential for embryonic development. *Journal of Cell Biology 160*(2), 189–200.

Chen, L., S. N. Willis, A. Wei, B. J. Smith, J. I. Fletcher, M. G. Hinds, P. M. Colman, C. L. Day, J. M. Adams, and D. C. S. Huang (2005, feb). Differential targeting of prosurvival Bcl-2 proteins by their BH3-only

ligands allows complementary apoptotic function. *Molecular cell 17*(3), 393–403.

Chen, Y.-J., P. Zhang, E. H. Egelman, and J. E. Hinshaw (2004, jun). The stalk region of dynamin drives the constriction of dynamin tubes. *Nature structural & molecular biology 11*(6), 574–5.

Cheng, E. H., D. G. Kirsch, R. J. Clem, R. Ravi, M. B. Kastan, A. Bedi, K. Ueno, and J. M. Hardwick (1997, dec). Conversion of Bcl-2 to a Bax-like death effector by caspases. *Science (New York, N.Y.) 278*(5345), 1966–8.

Chi, X., J. Kale, B. Leber, and D. W. Andrews (2014). Regulating cell death at, on, and in membranes. *Biochimica et biophysica acta 1843*(9), 2100–2113.

Cho, Y. S., S. Challa, D. Moquin, R. Genga, T. D. Ray, M. Guildford, and F. K.-M. Chan (2009, jun). Phosphorylation-driven assembly of the RIP1-RIP3 complex regulates programmed necrosis and virus-induced inflammation. *Cell 137*(6), 1112–23.

Chou, J. J., H. Li, G. S. Salvesen, J. Yuan, and G. Wagner (1999, mar). Solution structure of BID, an intracellular amplifier of apoptotic signaling. *Cell 96*(5), 615–24.

Chudakov, D. M., V. V. Verkhusha, D. B. Staroverov, E. A. Souslova, S. Lukyanov, and K. A. Lukyanov (2004, nov). Photoswitchable cyan fluorescent protein for protein tracking. *Nature biotechnology 22*(11), 1435–9.

Cipolat, S., O. M. de Brito, B. Dal Zilio, and L. Scorrano (2004, oct). OPA1 requires mitofusin 1 to promote mitochondrial fusion. *Proceedings of the National Academy of Sciences 101*(45), 15927–15932.

Cipolat, S., T. Rudka, D. Hartmann, V. Costa, L. Serneels, K. Craessaerts, K. Metzger, C. Frezza, W. Annaert, L. D'Adamio, C. Derks, T. Dejaegere, L. Pellegrini, R. D'Hooge, L. Scorrano, and B. De Strooper (2006, jul). Mitochondrial Rhomboid PARL Regulates Cytochrome c Release during Apoptosis via OPA1-Dependent Cristae Remodeling. *Cell 126*(1), 163–175.

Combs, C. A. (2010, jan). Fluorescence microscopy: a concise guide to current imaging methods. *Current protocols in neuroscience / editorial board, Jacqueline N. Crawley ... [et al.] Chapter 2*, Unit2.1.

Cosentino, K., U. Ros, and A. J. García-Sáez (2015, sep). Assembling the puzzle: Oligomerization of α-pore forming proteins in membranes. *Biochimica et biophysica acta*.

Cuervo, R. and L. Covarrubias (2004, jan). Death is the major fate of medial edge epithelial cells and the cause of basal lamina degradation during palatogenesis. *Development (Cambridge, England) 131*(1), 15–24.

Czabotar, P. E., D. Westphal, G. Dewson, S. Ma, C. Hockings, W. D. Fairlie, E. F. Lee, S. Yao, A. Y. Robin, B. J. Smith, D. C. S. Huang, R. M. Kluck, J. M. Adams, and P. M. Colman (2013, jan). Bax crystal structures reveal how BH3 domains activate Bax and nucleate its oligomerization to induce apoptosis. *Cell 152*(3), 519–31.

Dai, H., A. Smith, X. W. Meng, P. A. Schneider, Y.-P. Pang, and S. H. Kaufmann (2011, jul). Transient binding of an activator BH3 domain to the Bak BH3-binding groove initiates Bak oligomerization. *The Journal of cell biology 194*(1), 39–48.

Daugas, E., S. A. Susin, N. Zamzami, K. F. Ferri, T. Irinopoulou, N. Larochette, M. C. Prévost, B. Leber, D. Andrews, J. Penninger, and G. Kroemer (2000, apr). Mitochondrio-nuclear translocation of AIF in apoptosis and necrosis. *FASEB journal : official publication of the Federation of American Societies for Experimental Biology 14*(5), 729–39.

Day, C. L., L. Chen, S. J. Richardson, P. J. Harrison, D. C. S. Huang, and M. G. Hinds (2005, feb). Solution structure of prosurvival Mcl-1 and characterization of its binding by proapoptotic BH3-only ligands. *The Journal of biological chemistry 280*(6), 4738–44.

Degterev, A., Z. Huang, M. Boyce, Y. Li, P. Jagtap, N. Mizushima, G. D. Cuny, T. J. Mitchison, M. A. Moskowitz, and J. Yuan (2005, jul). Chemical inhibitor of nonapoptotic cell death with therapeutic potential for ischemic brain injury. *Nature chemical biology 1*(2), 112–9.

Dejean, L. M., S.-Y. Ryu, S. Martinez-Caballero, O. Teijido, P. M. Peixoto, and K. W. Kinnally (2010, jan). MAC and Bcl-2 family proteins conspire in a deadly plot. *Biochimica et biophysica acta 1797*(6-7), 1231–8.

Denisov, A. Y., G. Chen, T. Sprules, T. Moldoveanu, P. Beauparlant, and K. Gehring (2006, mar). Structural model of the BCL-w-BID peptide complex and its interactions with phospholipid micelles. *Biochemistry 45*(7), 2250–6.

Deveraux, Q. L., N. Roy, H. R. Stennicke, T. Van Arsdale, Q. Zhou, S. M. Srinivasula, E. S. Alnemri, G. S. Salvesen, and J. C. Reed (1998, apr). IAPs block apoptotic events induced by caspase-8 and cytochrome c by direct inhibition of distinct caspases. *The EMBO journal 17*(8), 2215–23.

Dewson, G., T. Kratina, H. W. Sim, H. Puthalakath, J. M. Adams, P. M. Colman, and R. M. Kluck (2008, may). To trigger apoptosis, Bak exposes its BH3 domain and homodimerizes via BH3:groove interactions. *Molecular cell 30*(3), 369–80.

Dewson, G., S. Ma, P. Frederick, C. Hockings, I. Tan, T. Kratina, and R. M. Kluck (2012, apr). Bax dimerizes via a symmetric BH3:groove interface during apoptosis. *Cell death and differentiation 19*(4), 661–70.

Ding, W.-X., H.-M. Ni, W. Gao, Y.-F. Hou, M. A. Melan, X. Chen, D. B. Stolz, Z.-M. Shao, and X.-M. Yin (2006, nov). Differential Effects of Endoplasmic Reticulum Stress-induced Autophagy on Cell Survival. *Journal of Biological Chemistry 282*(7), 4702–4710.

Duim, W. C., B. Chen, J. Frydman, and W. E. Moerner (2011, sep). Subdiffraction imaging of huntingtin protein aggregates by fluorescence blink-microscopy and atomic force microscopy. *Chemphyschem : a European journal of chemical physics and physical chemistry 12*(13), 2387–90.

Düssmann, H., M. Rehm, C. G. Concannon, S. Anguissola, M. Würstle, S. Kacmar, P. Völler, H. J. Huber, and J. H. M. Prehn (2010). Single-cell quantification of Bax activation and mathematical modelling suggest pore formation on minimal mitochondrial Bax accumulation. *Cell death and differentiation 17*(2), 278–290.

Dutta, S., S. Gullá, T. S. Chen, E. Fire, R. A. Grant, and A. E. Keating (2010, may). Determinants of BH3 binding specificity for Mcl-1 versus Bcl-xL. *Journal of molecular biology 398*(5), 747–62.

Edlich, F., S. Banerjee, M. Suzuki, M. M. Cleland, D. Arnoult, C. Wang, A. Neutzner, N. Tjandra, and R. J. Youle (2011, apr). Bcl-x(L) retrotranslocates Bax from the mitochondria into the cytosol. *Cell 145*(1), 104–16.

Edwards, A. L., E. Gavathiotis, J. L. LaBelle, C. R. Braun, K. A. Opoku-Nsiah, G. H. Bird, and L. D. Walensky (2013, jul). Multimodal interaction with BCL-2 family proteins underlies the proapoptotic activity of PUMA BH3. *Chemistry & biology 20*(7), 888–902.

Elmore, S. (2007, jun). Apoptosis: a review of programmed cell death. *Toxicologic pathology 35*(4), 495–516.

Eskes, R., S. Desagher, B. Antonsson, and J. C. Martinou (2000, feb). Bid induces the oligomerization and insertion of Bax into the outer mitochondrial membrane. *Molecular and cellular biology 20*(3), 929–35.

Fink, S. L. and B. T. Cookson (2007, nov). Pyroptosis and host cell death responses during Salmonella infection. *Cellular Microbiology 9*(11), 2562–2570.

Follis, A. V., J. E. Chipuk, J. C. Fisher, M.-K. Yun, C. R. Grace, A. Nourse, K. Baran, L. Ou, L. Min, S. W. White, D. R. Green, and R. W. Kriwacki (2013, mar). PUMA binding induces partial unfolding within BCL-xL to disrupt p53 binding and promote apoptosis. *Nature chemical biology 9*(3), 163–8.

Frank, S., B. Gaume, E. S. Bergmann-Leitner, W. W. Leitner, E. G. Robert, F. Catez, C. L. Smith, and R. J. Youle (2001, oct). The Role of Dynamin-Related Protein 1, a Mediator of Mitochondrial Fission, in Apoptosis. *Developmental Cell 1*(4), 515–525.

Frezza, C., S. Cipolat, O. Martins de Brito, M. Micaroni, G. V. Beznoussenko, T. Rudka, D. Bartoli, R. S. Polishuck, N. N. Danial, B. De Strooper, and L. Scorrano (2006, jul). OPA1 controls apoptotic cristae remodeling independently from mitochondrial fusion. *Cell 126*(1), 177–89.

Friedman, J. R., L. L. Lackner, M. West, J. R. DiBenedetto, J. Nunnari, and G. K. Voeltz (2011, oct). ER tubules mark sites of mitochondrial division. *Science (New York, N.Y.) 334*(6054), 358–62.

Friedman, J. R. and J. Nunnari (2014, jan). Mitochondrial form and function. *Nature 505*(7483), 335–43.

Fuertes, G., A. J. García-Sáez, S. Esteban-Martín, D. Giménez, O. L. Sánchez-Muñoz, P. Schwille, and J. Salgado (2010, dec). Pores formed by Baxα5 relax to a smaller size and keep at equilibrium. *Biophysical journal 99*(9), 2917–25.

Fulda, S. and K.-M. Debatin (2006, aug). Extrinsic versus intrinsic apoptosis pathways in anticancer chemotherapy. *Oncogene 25*(34), 4798–811.

Gandre-Babbe, S. and A. M. van der Bliek (2008, jun). The novel tail-anchored membrane protein Mff controls mitochondrial and peroxisomal fission in mammalian cells. *Molecular biology of the cell 19*(6), 2402–12.

García-Sáez, a. J. (2012). The secrets of the Bcl-2 family. *Cell Death and Differentiation 19*(11), 1733–1740.

García-Sáez, A. J., S. Chiantia, J. Salgado, and P. Schwille (2007, jul). Pore formation by a Bax-derived peptide: effect on the line tension of the membrane probed by AFM. *Biophysical journal 93*(1), 103–12.

García-Sáez, A. J., M. Coraiola, M. Dalla Serra, I. Mingarro, G. Menestrina, and J. Salgado (2005, jun). Peptides derived from apoptotic Bax and Bid reproduce the poration activity of the parent full-length proteins. *Biophysical journal 88*(6), 3976–90.

García-Sáez, A. J., I. Mingarro, E. Pérez-Payá, and J. Salgado (2004, aug). Membrane-insertion fragments of Bcl-xL, Bax, and Bid. *Biochemistry 43*(34), 10930–43.

García-Sáez, A. J., J. Ries, M. Orzáez, E. Pérez-Payà, and P. Schwille (2009). Membrane promotes tBID interaction with BCL(XL). *Nature structural & molecular biology 16*(11), 1178–1185.

Gavathiotis, E., M. Suzuki, M. L. Davis, K. Pitter, G. H. Bird, S. G. Katz, H.-C. Tu, H. Kim, E. H.-Y. Cheng, N. Tjandra, and L. D. Walensky (2008, oct). BAX activation is initiated at a novel interaction site. *Nature 455*(7216), 1076–81.

Germain, M., A. P. Nguyen, J. N. Le Grand, N. Arbour, J. L. Vanderluit, D. S. Park, J. T. Opferman, and R. S. Slack (2011, jan). MCL-1 is a stress sensor that regulates autophagy in a developmentally regulated manner. *The EMBO journal 30*(2), 395–407.

Giepmans, B. N. G., S. R. Adams, M. H. Ellisman, and R. Y. Tsien (2006, apr). The fluorescent toolbox for assessing protein location and function. *Science (New York, N.Y.) 312*(5771), 217–24.

Gilbert, R. J. C., M. Dalla Serra, C. J. Froelich, M. I. Wallace, and G. Anderluh (2014, nov). Membrane pore formation at protein-lipid interfaces. *Trends in biochemical sciences 39*(11), 510–6.

Gillies, L. A., H. Du, B. Peters, C. M. Knudson, D. D. Newmeyer, and T. Kuwana (2015, jan). Visual and functional demonstration of growing Bax-induced pores in mitochondrial outer membranes. *Molecular biology of the cell 26*(2), 339–49.

Golstein, P. and G. Kroemer (2007, jan). Cell death by necrosis: towards a molecular definition. *Trends in biochemical sciences 32*(1), 37–43.

Green, D. R. and G. Kroemer (2004, jul). The pathophysiology of mitochondrial cell death. *Science (New York, N.Y.) 305*(5684), 626–9.

Gross, A., X. M. Yin, K. Wang, M. C. Wei, J. Jockel, C. Milliman, H. Erdjument-Bromage, P. Tempst, and S. J. Korsmeyer (1999, jan). Caspase cleaved BID targets mitochondria and is required for cytochrome c release, while BCL-XL prevents this release but not tumor necrosis factor-R1/Fas death. *The Journal of biological chemistry 274*(2), 1156–63.

Große, L., C. A. Wurm, C. Brüser, D. Neumann, D. C. Jans, and S. Jakobs (2016, jan). Bax assembles into large ring-like structures remodeling the mitochondrial outer membrane in apoptosis. *The EMBO journal 35*(4), 402–13.

Grossmann, J. (2002, jun). Molecular mechanisms of "detachment-induced apoptosis–Anoikis". *Apoptosis : an international journal on programmed cell death 7*(3), 247–60.

Gustafsson, M. G. (2000, may). Surpassing the lateral resolution limit by a factor of two using structured illumination microscopy. *Journal of microscopy 198*(Pt 2), 82–7.

Gustafsson, M. G. L. (2005, sep). Nonlinear structured-illumination microscopy: wide-field fluorescence imaging with theoretically unlimited resolution. *Proceedings of the National Academy of Sciences of the United States of America 102*(37), 13081–6.

Gustafsson, M. G. L. (2008, may). Super-resolution light microscopy goes live. *Nature methods 5*(5), 385–7.

Hanne, J., H. J. Falk, F. Görlitz, P. Hoyer, J. Engelhardt, S. J. Sahl, and S. W. Hell (2015, may). STED nanoscopy with fluorescent quantum dots. *Nature Communications 6*, 7127.

Hardwick, J. M. (2001, feb). Apoptosis in viral pathogenesis. *Cell death and differentiation 8*(2), 109–10.

Heilemann, M., S. van de Linde, M. Schüttpelz, R. Kasper, B. Seefeldt, A. Mukherjee, P. Tinnefeld, and M. Sauer (2008, jan). Subdiffraction-resolution fluorescence imaging with conventional fluorescent probes. *Angewandte Chemie (International ed. in English) 47*(33), 6172–6.

Hein, B., K. I. Willig, and S. W. Hell (2008, sep). Stimulated emission depletion (STED) nanoscopy of a fluorescent protein-labeled organelle inside a living cell. *Proceedings of the National Academy of Sciences of the United States of America 105*(38), 14271–6.

Heintzmann, R. and C. Cremer (1999). Laterally modulated excitation microscopy: improvement of resolution by using a diffraction grating. *BiOS Europe'98*.

Hell, S. W. (2003, nov). Toward fluorescence nanoscopy. *Nature biotechnology 21*(11), 1347–55.

Hell, S. W. (2007, may). Far-field optical nanoscopy. *Science (New York, N.Y.) 316*(5828), 1153–8.

Hell, S. W. and J. Wichmann (1994, jun). Breaking the diffraction resolution limit by stimulated emission: stimulated-emission-depletion fluorescence microscopy. *Optics letters 19*(11), 780–2.

Hilderbrand, S. A. (2010, jan). Labels and probes for live cell imaging: overview and selection guide. *Methods in molecular biology (Clifton, N.J.) 591*, 17–45.

Hinds, M. G., C. Smits, R. Fredericks-Short, J. M. Risk, M. Bailey, D. C. S. Huang, and C. L. Day (2007, jan). Bim, Bad and Bmf: intrinsically unstructured BH3-only proteins that undergo a localized conformational change upon binding to prosurvival Bcl-2 targets. *Cell death and differentiation 14*(1), 128–36.

Hockenbery, D., G. Nuñez, C. Milliman, R. D. Schreiber, and S. J. Korsmeyer (1990, nov). Bcl-2 is an inner mitochondrial membrane protein that blocks programmed cell death. *Nature 348*(6299), 334–6.

Hofmann, M., C. Eggeling, S. Jakobs, and S. W. Hell (2005, dec). Breaking the diffraction barrier in fluorescence microscopy at low light intensities by using reversibly photoswitchable proteins. *Proceedings of the National Academy of Sciences of the United States of America 102*(49), 17565–9.

Hoppins, S., F. Edlich, M. M. Cleland, S. Banerjee, J. M. McCaffery, R. J. Youle, and J. Nunnari (2011). The Soluble Form of Bax Regulates Mitochondrial Fusion via MFN2 Homotypic Complexes. *Molecular Cell 41*(2), 150–160.

Hoshino, K., A. Gopal, M. S. Glaz, D. A. Vanden Bout, and X. Zhang (2012, jul). Nanoscale fluorescence imaging with quantum dot near-field electroluminescence. *Applied Physics Letters 101*(4), 043118.

Huang, F., T. M. P. Hartwich, F. E. Rivera-Molina, Y. Lin, W. C. Duim, J. J. Long, P. D. Uchil, J. R. Myers, M. A. Baird, W. Mothes, M. W. Davidson, D. Toomre, and J. Bewersdorf (2013, jul). Video-rate nanoscopy using sCMOS camera-specific single-molecule localization algorithms. *Nature methods 10*(7), 653–8.

Ingerman, E., E. M. Perkins, M. Marino, J. A. Mears, J. M. McCaffery, J. E. Hinshaw, and J. Nunnari (2005, sep). Dnm1 forms spirals that are structurally tailored to fit mitochondria. *The Journal of cell biology 170*(7), 1021–7.

Ishihara, N., A. Jofuku, Y. Eura, and K. Mihara (2003). Regulation of mitochondrial morphology by membrane potential, and DRP1-dependent division and FZO1-dependent fusion reaction in mammalian cells. *Biochemical and Biophysical Research Communications 301*(4), 891–898.

Ishikawa-Ankerhold, H. C., R. Ankerhold, and G. P. C. Drummen (2012, jan). Advanced fluorescence microscopy techniques–FRAP, FLIP, FLAP, FRET and FLIM. *Molecules (Basel, Switzerland) 17*(4), 4047–132.

Jakobs, S. (2006, jan). High resolution imaging of live mitochondria. *Biochimica et biophysica acta 1763*(5-6), 561–75.

James, D. I., P. A. Parone, Y. Mattenberger, and J.-C. Martinou (2003, sep). hFis1, a novel component of the mammalian mitochondrial fission machinery. *The Journal of biological chemistry 278*(38), 36373–9.

Jones, S. A., S.-H. Shim, J. He, and X. Zhuang (2011, jun). Fast, three-dimensional super-resolution imaging of live cells. *Nature methods 8*(6), 499–508.

Jouan-Lanhouet, S., M. I. Arshad, C. Piquet-Pellorce, C. Martin-Chouly, G. Le Moigne-Muller, F. Van Herreweghe, N. Takahashi, O. Sergent, D. Lagadic-Gossmann, P. Vandenabeele, M. Samson, and M.-T. Dimanche-Boitrel (2012, jul). TRAIL induces necroptosis involving RIPK1/RIPK3-dependent PARP-1 activation. *Cell Death and Differentiation 19*(12), 2003–2014.

Karatekin, E., O. Sandre, H. Guitouni, N. Borghi, P.-H. Puech, and F. Brochard-Wyart (2003, mar). Cascades of transient pores in giant vesicles: line tension and transport. *Biophysical journal 84*(3), 1734–49.

Karbowski, M. (2010, jan). Mitochondria on guard: role of mitochondrial fusion and fission in the regulation of apoptosis. *Advances in experimental medicine and biology 687*, 131–42.

Karbowski, M., Y.-J. Lee, B. Gaume, S.-Y. Jeong, S. Frank, A. Nechushtan, A. Santel, M. Fuller, C. L. Smith, and R. J. Youle (2002, dec). Spatial and temporal association of Bax with mitochondrial fission sites, Drp1, and Mfn2 during apoptosis. *The Journal of cell biology 159*(6), 931–8.

Karbowski, M., K. L. Norris, M. M. Cleland, S.-Y. Jeong, and R. J. Youle (2006, oct). Role of Bax and Bak in mitochondrial morphogenesis. *Nature 443*(7112), 658–62.

Kerr, J. F., A. H. Wyllie, and A. R. Currie (1972, aug). Apoptosis: a basic biological phenomenon with wide-ranging implications in tissue kinetics. *British journal of cancer 26*(4), 239–57.

Kim, W. R. and W. Sun (2011, feb). Programmed cell death during postnatal development of the rodent nervous system. *Development, growth & differentiation 53*(2), 225–35.

Kischkel, F.C., S Hellbardt, I Behrmann, M Germer, M Pawlita, P H Krammer, M. E. P. (1995, nov). Cytotoxicity-dependent APO-1 (Fas/CD95)-associated proteins form a death-inducing signaling complex (DISC) with the receptor.

Klar, T. A., S. Jakobs, M. Dyba, A. Egner, and S. W. Hell (2000, jul). Fluorescence microscopy with diffraction resolution barrier broken by stimulated emission. *Proceedings of the National Academy of Sciences of the United States of America 97*(15), 8206–10.

Korsmeyer, S. J., M. C. Wei, M. Saito, S. Weiler, K. J. Oh, and P. H. Schlesinger (2000, dec). Pro-apoptotic cascade activates BID, which oligomerizes BAK or BAX into pores that result in the release of cytochrome c. *Cell death and differentiation 7*(12), 1166–73.

Kozlovsky, Y. and M. M. Kozlov (2003, jul). Membrane fission: model for intermediate structures. *Biophysical journal 85*(1), 85–96.

Kroemer, G., L. Galluzzi, P. Vandenabeele, J. Abrams, E. S. Alnemri, E. H. Baehrecke, M. V. Blagosklonny, W. S. El-Deiry, P. Golstein, D. R. Green, M. Hengartner, R. A. Knight, S. Kumar, S. A. Lipton, W. Malorni, G. Nuñez, M. E. Peter, J. Tschopp, J. Yuan, M. Piacentini, B. Zhivotovsky, and G. Melino (2009, jan). Classification of cell death: recommendations of the Nomenclature Committee on Cell Death 2009. *Cell death and differentiation 16*(1), 3–11.

Kuwana, T., L. Bouchier-Hayes, J. E. Chipuk, C. Bonzon, B. A. Sullivan, D. R. Green, and D. D. Newmeyer (2005, feb). BH3 domains of BH3-only proteins differentially regulate Bax-mediated mitochondrial membrane permeabilization both directly and indirectly. *Molecular cell 17*(4), 525–35.

Kuwana, T., M. R. Mackey, G. Perkins, M. H. Ellisman, M. Latterich, R. Schneiter, D. R. Green, and D. D. Newmeyer (2002, nov). Bid, Bax, and lipids cooperate to form supramolecular openings in the outer mitochondrial membrane. *Cell 111*(3), 331–42.

Lakadamyali, M. (2014, mar). Super-resolution microscopy: going live and going fast. *Chemphyschem : a European journal of chemical physics and physical chemistry 15*(4), 630–6.

Lavrik, I., A. Golks, and P. H. Krammer (2005, jan). Death receptor signaling. *Journal of cell science 118*(Pt 2), 265–7.

Leber, B., J. Lin, and D. W. Andrews (2007, may). Embedded together: the life and death consequences of interaction of the Bcl-2 family with membranes. *Apoptosis : an international journal on programmed cell death 12*(5), 897–911.

Lee, Y.-j., S.-Y. Jeong, M. Karbowski, C. L. Smith, and R. J. Youle (2004, nov). Roles of the mammalian mitochondrial fission and fusion mediators Fis1, Drp1, and Opa1 in apoptosis. *Molecular biology of the cell 15*(11), 5001–11.

Legros, F., A. Lombès, P. Frachon, and M. Rojo (2002, dec). Mitochondrial fusion in human cells is efficient, requires the inner membrane potential, and is mediated by mitofusins. *Molecular biology of the cell 13*(12), 4343–54.

Lemasters, J. J. (2005, mar). Selective Mitochondrial Autophagy, or Mitophagy, as a Targeted Defense Against Oxidative Stress, Mitochondrial Dysfunction, and Aging. *Rejuvenation Research 8*(1), 3–5.

Leshchiner, E. S., C. R. Braun, G. H. Bird, and L. D. Walensky (2013, mar). Direct activation of full-length proapoptotic BAK. *Proceedings of the National Academy of Sciences of the United States of America 110*(11), E986–95.

Letai, A., M. C. Bassik, L. D. Walensky, M. D. Sorcinelli, S. Weiler, and S. J. Korsmeyer (2002, sep). Distinct BH3 domains either sensitize or activate mitochondrial apoptosis, serving as prototype cancer therapeutics. *Cancer cell 2*(3), 183–92.

Leung, C., N. V. Dudkina, N. Lukoyanova, A. W. Hodel, I. Farabella, A. P. Pandurangan, N. Jahan, M. Pires Damaso, D. Osmanović, C. F. Reboul, M. A. Dunstone, P. W. Andrew, R. Lonnen, M. Topf, H. R. Saibil, and B. W. Hoogenboom (2014, jan). Stepwise visualization of membrane pore formation by suilysin, a bacterial cholesterol-dependent cytolysin. *eLife 3*, e04247.

Lev, N., E. Melamed, and D. Offen (2003, apr). Apoptosis and Parkinson's disease. *Progress in Neuro-Psychopharmacology and Biological Psychiatry 27*(2), 245–250.

Levine, B. and G. Kroemer (2008, jan). Autophagy in the pathogenesis of disease. *Cell 132*(1), 27–42.

Li, A., J. C. Felix, J. Hao, P. Minoo, and J. K. Jain (2005, jun). Menstrual-like breakdown and apoptosis in human endometrial explants. *Human reproduction (Oxford, England) 20*(6), 1709–19.

Li, H., Y. Chen, A. F. Jones, R. H. Sanger, L. P. Collis, R. Flannery, E. C. McNay, T. Yu, R. Schwarzenbacher, B. Bossy, E. Bossy-Wetzel, M. V. L. Bennett, M. Pypaert, J. A. Hickman, P. J. S. Smith, J. M. Hardwick, and E. A. Jonas (2008, feb). Bcl-xL induces Drp1-dependent synapse formation in cultured hippocampal neurons. *Proceedings of the National Academy of Sciences of the United States of America 105*(6), 2169–74.

Li, H., H. Zhu, C. J. Xu, and J. Yuan (1998, aug). Cleavage of BID by caspase 8 mediates the mitochondrial damage in the Fas pathway of apoptosis. *Cell 94*(4), 491–501.

Lichtman, J. W. and J.-A. Conchello (2005, dec). Fluorescence microscopy. *Nature methods 2*(12), 910–9.

Lippincott-Schwartz, J., N. Altan-Bonnet, and G. H. Patterson (2003). Photobleaching and photoactivation: following protein dynamics in living cells. *Nature cell biology Suppl*(September), S7–S14.

Liu, Q., B. Leber, and D. W. Andrews (2012, oct). Interactions of pro-apoptotic BH3 proteins with anti-apoptotic Bcl-2 family proteins measured in live MCF-7 cells using FLIM FRET. *Cell cycle (Georgetown, Tex.) 11*(19), 3536–42.

Liu, X., C. N. Kim, J. Yang, R. Jemmerson, and X. Wang (1996, jul). Induction of apoptotic program in cell-free extracts: requirement for dATP and cytochrome c. *Cell 86*(1), 147–57.

Llambi, F., T. Moldoveanu, S. W. G. Tait, L. Bouchier-Hayes, J. Temirov, L. L. McCormick, C. P. Dillon, and D. R. Green (2011, nov). A unified model of mammalian BCL-2 protein family interactions at the mitochondria. *Molecular cell 44*(4), 517–31.

Lockshin, R. and C. Williams (1965, feb). Programmed cell death-I. Cytology of degeneration in the intersegmental muscles of the pernyi silkmoth. *Journal of insect physiology 11*, 123–33.

Locksley, R. M., N. Killeen, and M. J. Lenardo (2001, feb). The TNF and TNF receptor superfamilies: integrating mammalian biology. *Cell 104*(4), 487–501.

Losonczi, J. A., E. T. Olejniczak, S. F. Betz, J. E. Harlan, J. Mack, and S. W. Fesik (2000, sep). NMR studies of the anti-apoptotic protein Bcl-xL in micelles. *Biochemistry 39*(36), 11024–33.

Lovell, J. F., L. P. Billen, S. Bindner, A. Shamas-Din, C. Fradin, B. Leber, and D. W. Andrews (2008, dec). Membrane binding by tBid initiates an ordered series of events culminating in membrane permeabilization by Bax. *Cell 135*(6), 1074–84.

Luo, X., I. Budihardjo, H. Zou, C. Slaughter, and X. Wang (1998, aug). Bid, a Bcl2 interacting protein, mediates cytochrome c release from mitochondria in response to activation of cell surface death receptors. *Cell 94*(4), 481–90.

Martinez-Caballero, S., L. M. Dejean, M. S. Kinnally, K. J. Oh, C. A. Mannella, and K. W. Kinnally (2009, may). Assembly of the mitochondrial apoptosis-induced channel, MAC. *The Journal of biological chemistry 284*(18), 12235–45.

Martinou, J.-C. and R. J. Youle (2011, jul). Mitochondria in apoptosis: Bcl-2 family members and mitochondrial dynamics. *Developmental cell 21*(1), 92–101.

McDonnell, J. M., D. Fushman, C. L. Milliman, S. J. Korsmeyer, and D. Cowburn (1999, mar). Solution structure of the proapoptotic molecule BID: a structural basis for apoptotic agonists and antagonists. *Cell 96*(5), 625–34.

Mears, J. A., L. L. Lackner, S. Fang, E. Ingerman, J. Nunnari, and J. E. Hinshaw (2011, jan). Conformational changes in Dnm1 support a contractile mechanism for mitochondrial fission. *Nature structural & molecular biology 18*(1), 20–6.

Metkar, S. S., M. Marchioretto, V. Antonini, L. Lunelli, B. Wang, R. J. C. Gilbert, G. Anderluh, R. Roth, M. Pooga, J. Pardo, J. E. Heuser, M. D. Serra, and C. J. Froelich (2015, jan). Perforin oligomers form arcs in

cellular membranes: a locus for intracellular delivery of granzymes. *Cell death and differentiation 22*(1), 74–85.

Moldoveanu, T., C. R. Grace, F. Llambi, A. Nourse, P. Fitzgerald, K. Gehring, R. W. Kriwacki, and D. R. Green (2013, may). BID-induced structural changes in BAK promote apoptosis. *Nature structural & molecular biology 20*(5), 589–97.

Moldoveanu, T., Q. Liu, A. Tocilj, M. Watson, G. Shore, and K. Gehring (2006, dec). The X-ray structure of a BAK homodimer reveals an inhibitory zinc binding site. *Molecular cell 24*(5), 677–88.

Montessuit, S., S. P. Somasekharan, O. Terrones, S. Lucken-Ardjomande, S. Herzig, R. Schwarzenbacher, D. J. Manstein, E. Bossy-Wetzel, G. Basañez, P. Meda, and J. C. Martinou (2010). Membrane Remodeling Induced by the Dynamin-Related Protein Drp1 Stimulates Bax Oligomerization. *Cell 142*(6), 889–901.

Muchmore, S. W., M. Sattler, H. Liang, R. P. Meadows, J. E. Harlan, H. S. Yoon, D. Nettesheim, B. S. Chang, C. B. Thompson, S. L. Wong, S. L. Ng, and S. W. Fesik (1996, may). X-ray and NMR structure of human Bcl-xL, an inhibitor of programmed cell death. *Nature 381*(6580), 335–41.

Mund, M., C. Kaplan, and J. Ries (2014, jan). Localization microscopy in yeast. *Methods in cell biology 123*, 253–71.

Muñoz-Pinedo, C. (2012, jan). Signaling pathways that regulate life and cell death: evolution of apoptosis in the context of self-defense. *Advances in experimental medicine and biology 738*, 124–43.

Muñoz-Pinedo, C., A. Guío-Carrión, J. C. Goldstein, P. Fitzgerald, D. D. Newmeyer, and D. R. Green (2006, aug). Different mitochondrial intermembrane space proteins are released during apoptosis in a manner that is coordinately initiated but can vary in duration. *Proceedings of the National Academy of Sciences of the United States of America 103*(31), 11573–8.

Muzio, M., A. M. Chinnaiyan, F. C. Kischkel, K. O'Rourke, A. Shevchenko, J. Ni, C. Scaffidi, J. D. Bretz, M. Zhang, R. Gentz, M. Mann, P. H. Krammer, M. E. Peter, and V. M. Dixit (1996, jun). FLICE, a novel FADD-homologous ICE/CED-3-like protease, is recruited to the CD95 (Fas/APO-1) death–inducing signaling complex. *Cell 85*(6), 817–27.

Nakagawa, Y., T. Suzuki, H. Kamimura, and F. Nagai (2006, jan). Role of mitochondrial membrane permeability transition in N-nitrosofenfluramine-induced cell injury in rat hepatocytes. *European journal of pharmacology 529*(1-3), 33–9.

Narita, M., S. Shimizu, T. Ito, T. Chittenden, R. J. Lutz, H. Matsuda, and Y. Tsujimoto (1998, dec). Bax interacts with the permeability transition pore to induce permeability transition and cytochrome c release in isolated mitochondria. *Proceedings of the National Academy of Sciences of the United States of America 95*(25), 14681–6.

Nienhaus, K. and G. U. Nienhaus (2015, dec). Where do we stand with super-resolution optical microscopy? *Journal of molecular biology*.

Nikoletopoulou, V., M. Markaki, K. Palikaras, and N. Tavernarakis (2013, dec). Crosstalk between apoptosis, necrosis and autophagy. *Biochimica et biophysica acta 1833*(12), 3448–59.

Oh, K. J., P. Singh, K. Lee, K. Foss, S. Lee, M. Park, S. Lee, S. Aluvila, M. Park, P. Singh, R.-S. Kim, J. Symersky, and D. E. Walters (2010, sep). Conformational changes in BAK, a pore-forming proapoptotic Bcl-2 family member, upon membrane insertion and direct evidence for the existence of BH3-BH3 contact interface in BAK homo-oligomers. *The Journal of biological chemistry 285*(37), 28924–37.

Ormö, M., A. B. Cubitt, K. Kallio, L. A. Gross, R. Y. Tsien, and S. J. Remington (1996, sep). Crystal structure of the Aequorea victoria green fluorescent protein. *Science (New York, N.Y.) 273*(5280), 1392–5.

Otera, H., N. Miyata, O. Kuge, and K. Mihara (2016, feb). Drp1-dependent mitochondrial fission via MiD49/51 is essential for apoptotic cristae remodeling. *The Journal of cell biology 212*(5), 531–44.

Otera, H., C. Wang, M. M. Cleland, K. Setoguchi, S. Yokota, R. J. Youle, and K. Mihara (2010, dec). Mff is an essential factor for mitochondrial recruitment of Drp1 during mitochondrial fission in mammalian cells. *The Journal of cell biology 191*(6), 1141–58.

Overholtzer, M., A. A. Mailleux, G. Mouneimne, G. Normand, S. J. Schnitt, R. W. King, E. S. Cibas, and J. S. Brugge (2007, nov). A nonapoptotic cell death process, entosis, that occurs by cell-in-cell invasion. *Cell 131*(5), 966–79.

Palmer, C. S., K. D. Elgass, R. G. Parton, L. D. Osellame, D. Stojanovski, and M. T. Ryan (2013, sep). Adaptor proteins MiD49 and MiD51 can act independently of Mff and Fis1 in Drp1 recruitment and are specific for mitochondrial fission. *The Journal of biological chemistry 288*(38), 27584–93.

Parrish, J., L. Li, K. Klotz, D. Ledwich, X. Wang, and D. Xue (2001, jul). Mitochondrial endonuclease G is important for apoptosis in C. elegans. *Nature 412*(6842), 90–4.

Pattingre, S., A. Tassa, X. Qu, R. Garuti, X. H. Liang, N. Mizushima, M. Packer, M. D. Schneider, and B. Levine (2005, sep). Bcl-2 antiapoptotic proteins inhibit Beclin 1-dependent autophagy. *Cell 122*(6), 927–39.

Petros, A. M., D. G. Nettesheim, Y. Wang, E. T. Olejniczak, R. P. Meadows, J. Mack, K. Swift, E. D. Matayoshi, H. Zhang, C. B. Thompson, and S. W. Fesik (2000, dec). Rationale for Bcl-xL/Bad peptide complex formation from structure, mutagenesis, and biophysical studies. *Protein science : a publication of the Protein Society 9*(12), 2528–34.

Petros, A. M., E. T. Olejniczak, and S. W. Fesik (2004, mar). Structural biology of the Bcl-2 family of proteins. *Biochimica et biophysica acta 1644*(2-3), 83–94.

Picco, A., M. Mund, J. Ries, F. Nédélec, and M. Kaksonen (2015, jan). Visualizing the functional architecture of the endocytic machinery. *eLife 4*.

Polster, B. M., G. Basañez, A. Etxebarria, J. M. Hardwick, and D. G. Nicholls (2005, feb). Calpain I induces cleavage and release of apoptosis-inducing factor from isolated mitochondria. *The Journal of biological chemistry 280*(8), 6447–54.

Progatzky, F., M. J. Dallman, and C. Lo Celso (2013, jun). From seeing to believing: labelling strategies for in vivo cell-tracking experiments. *Interface focus 3*(3), 20130001.

Prudent, J., R. Zunino, A. Sugiura, S. Mattie, G. C. Shore, and H. M. McBride (2015, sep). MAPL SUMOylation of Drp1 Stabilizes an ER/Mitochondrial Platform Required for Cell Death. *Molecular cell 59*(6), 941–55.

Qian, S., W. Wang, L. Yang, and H. W. Huang (2008). Structure of transmembrane pore induced by Bax-derived peptide: evidence for lipidic pores. *Proceedings of the National Academy of Sciences of the United States of America 105*(45), 17379–17383.

Rankin, B. R., G. Moneron, C. A. Wurm, J. C. Nelson, A. Walter, D. Schwarzer, J. Schroeder, D. A. Colón-Ramos, and S. W. Hell (2011, jun). Nanoscopy in a living multicellular organism expressing GFP. *Biophysical journal 100*(12), L63–5.

Reed, M., J. Randall, R. Aggarwal, R. Matyi, T. Moore, and A. Wetsel (1988, feb). Observation of discrete electronic states in a zero-dimensional semiconductor nanostructure. *Physical Review Letters 60*(6), 535–537.

Rehm, M., H. Düssmann, and J. H. M. Prehn (2003, sep). Real-time single cell analysis of Smac/DIABLO release during apoptosis. *The Journal of cell biology 162*(6), 1031–43.

Renault, T. T., K. V. Floros, R. Elkholi, K.-a. Corrigan, Y. Kushnareva, S. Y. Wieder, C. Lindtner, M. N. Serasinghe, J. J. Asciolla, C. Buettner, D. D. Newmeyer, and J. E. Chipuk (2015). Mitochondrial Shape Governs BAX-Induced Membrane Permeabilization and Apoptosis. *Molecular Cell 57*(1), 69–82.

Ricci, M., C. Manzo, M. F. García-Parajo, M. Lakadamyali, and M. Cosma (2015). Chromatin Fibers Are Formed by Heterogeneous Groups of Nucleosomes InÂ Vivo. *Cell 160*(6), 1145–1158.

Ries, J., C. Kaplan, E. Platonova, H. Eghlidi, and H. Ewers (2012, jun). A simple, versatile method for GFP-based super-resolution microscopy via nanobodies. *Nature methods 9*(6), 582–4.

Ries, J. and P. Schwille (2006, sep). Studying slow membrane dynamics with continuous wave scanning fluorescence correlation spectroscopy. *Biophysical journal 91*(5), 1915–24.

Ries, J., V. Udayar, A. Soragni, S. Hornemann, K. P. R. Nilsson, R. Riek, C. Hock, H. Ewers, A. A. Aguzzi, and L. Rajendran (2013, jul). Super-resolution imaging of amyloid fibrils with binding-activated probes. *ACS chemical neuroscience 4*(7), 1057–61.

Ries, J., T. Weidemann, and P. Schwille (2012). *Comprehensive Biophysics*. Elsevier.

Roninson, I. B., E. V. Broude, and B.-D. Chang (2001, oct). If not apoptosis, then what? Treatment-induced senescence and mitotic catastrophe in tumor cells. *Drug Resistance Updates 4*(5), 303–313.

Ros, U. and A. J. García-Sáez (2015, jun). More Than a Pore: The Interplay of Pore-Forming Proteins and Lipid Membranes. *The Journal of membrane biology 248*(3), 545–61.

Rosenbloom, a. B., S.-H. Lee, M. To, a. Lee, J. Y. Shin, and C. Bustamante (2014). Optimized two-color super resolution imaging of Drp1 during mitochondrial fission with a slow-switching Dronpa variant. *Proceedings of the National Academy of Sciences*.

Rothbauer, U., K. Zolghadr, S. Tillib, D. Nowak, L. Schermelleh, A. Gahl, N. Backmann, K. Conrath, S. Muyldermans, M. C. Cardoso, and H. Leonhardt (2006, dec). Targeting and tracing antigens in live cells with fluorescent nanobodies. *Nature methods 3*(11), 887–9.

Rubio-Moscardo, F., D. Blesa, C. Mestre, R. Siebert, T. Balasas, A. Benito, A. Rosenwald, J. Climent, J. I. Martinez, M. Schilhabel, E. L. Karran, S. Gesk, M. Esteller, R. DeLeeuw, L. M. Staudt, J. L. Fernandez-Luna, D. Pinkel, M. J. S. Dyer, and J. A. Martinez-Climent (2005, nov). Characterization of 8p21.3 chromosomal deletions in B-cell lymphoma: TRAIL-R1

and TRAIL-R2 as candidate dosage-dependent tumor suppressor genes. *Blood 106*(9), 3214–22.

Rust, M. J., M. Bates, and X. Zhuang (2006, oct). Sub-diffraction-limit imaging by stochastic optical reconstruction microscopy (STORM). *Nature methods 3*(10), 793–5.

Saelens, X., N. Festjens, L. Vande Walle, M. van Gurp, G. van Loo, and P. Vandenabeele (2004, apr). Toxic proteins released from mitochondria in cell death. *Oncogene 23*(16), 2861–74.

Saito, M., S. J. Korsmeyer, and P. H. Schlesinger (2000, aug). BAX-dependent transport of cytochrome c reconstituted in pure liposomes. *Nature cell biology 2*(8), 553–5.

Salvador-Gallego, R., M. Mund, K. Cosentino, J. Schneider, J. Unsay, U. Schraermeyer, J. Engelhardt, J. Ries, and A. J. García-Sáez (2016, jan). Bax assembly into rings and arcs in apoptotic mitochondria is linked to membrane pores. *The EMBO journal*.

Scaffidi, C., S. Fulda, A. Srinivasan, C. Friesen, F. Li, K. J. Tomaselli, K. M. Debatin, P. H. Krammer, and M. E. Peter (1998, mar). Two CD95 (APO-1/Fas) signaling pathways. *The EMBO journal 17*(6), 1675–87.

Schellenberg, B., P. Wang, J. A. Keeble, R. Rodriguez-Enriquez, S. Walker, T. W. Owens, F. Foster, J. Tanianis-Hughes, K. Brennan, C. H. Streuli, and A. P. Gilmore (2013, mar). Bax exists in a dynamic equilibrium between the cytosol and mitochondria to control apoptotic priming. *Molecular cell 49*(5), 959–71.

Schermelleh, L., R. Heintzmann, and H. Leonhardt (2010, jul). A guide to super-resolution fluorescence microscopy. *The Journal of cell biology 190*(2), 165–75.

Schmidt, R., C. A. Wurm, A. Punge, A. Egner, S. Jakobs, and S. W. Hell (2009, jun). Mitochondrial cristae revealed with focused light. *Nano letters 9*(6), 2508–10.

Scorrano, L., M. Ashiya, K. Buttle, S. Weiler, S. A. Oakes, C. A. Mannella, and S. J. Korsmeyer (2002, jan). A distinct pathway remodels mitochondrial cristae and mobilizes cytochrome c during apoptosis. *Developmental cell 2*(1), 55–67.

Shamas-Din, A., H. Brahmbhatt, B. Leber, and D. W. Andrews (2011, apr). BH3-only proteins: Orchestrators of apoptosis. *Biochimica et biophysica acta 1813*(4), 508–20.

Shaner, N. C., P. A. Steinbach, and R. Y. Tsien (2005, dec). A guide to choosing fluorescent proteins. *Nature methods 2*(12), 905–9.

Shimomura, O., F. H. Johnson, and Y. Saiga (1962, jun). Extraction, Purification and Properties of Aequorin, a Bioluminescent Protein from the Luminous Hydromedusan,Aequorea. *Journal of Cellular and Comparative Physiology 59*(3), 223–239.

Shroff, H., C. G. Galbraith, J. A. Galbraith, and E. Betzig (2008, may). Live-cell photoactivated localization microscopy of nanoscale adhesion dynamics. *Nature methods 5*(5), 417–23.

Smirnova, E., L. Griparic, D. L. Shurland, and A. M. van der Bliek (2001, aug). Dynamin-related protein Drp1 is required for mitochondrial division in mammalian cells. *Molecular biology of the cell 12*(8), 2245–56.

Sonnen, A. F.-P., J. M. Plitzko, and R. J. C. Gilbert (2014, apr). Incomplete pneumolysin oligomers form membrane pores. *Open Biology 4*(4), 140044–140044.

Sperandio, S., I. de Belle, and D. E. Bredesen (2000, dec). An alternative, nonapoptotic form of programmed cell death. *Proceedings of the National Academy of Sciences 97*(26), 14376–14381.

Stepanyants, N., P. J. Macdonald, C. A. Francy, J. A. Mears, X. Qi, and R. Ramachandran (2015, sep). Cardiolipin's propensity for phase transition and its reorganization by dynamin-related protein 1 form a basis for mitochondrial membrane fission. *Molecular biology of the cell 26*(17), 3104–16.

Stewart, S. E., M. E. D'Angelo, S. Paintavigna, R. F. Tabor, L. L. Martin, and P. I. Bird (2015, jan). Assembly of streptolysin O pores assessed by quartz crystal microbalance and atomic force microscopy provides evidence for the formation of anchored but incomplete oligomers. *Biochimica et biophysica acta 1848*(1 Pt A), 115–26.

Su, J. H., A. J. Anderson, B. J. Cummings, and C. W. Cotman (1994, dec). Immunohistochemical evidence for apoptosis in Alzheimer's disease. *Neuroreport 5*(18), 2529–33.

Subburaj, Y., K. Cosentino, M. Axmann, E. Pedrueza-Villalmanzo, E. Hermann, S. Bleicken, J. Spatz, and A. J. García-Sáez (2015, aug). Bax monomers form dimer units in the membrane that further self-assemble into multiple oligomeric species. *Nature Communications 6*, 8042.

Subburaj, Y., R. S. Gallego, and A. J. García-Sáez (2013). Membrane Dynamics: Fluorescence Spectroscopy. *Encyclopedia of Analytical Chemistry*, 1–29.

Sun, L., H. Wang, Z. Wang, S. He, S. Chen, D. Liao, L. Wang, J. Yan, W. Liu, X. Lei, and X. Wang (2012, jan). Mixed Lineage Kinase Domain-like Protein Mediates Necrosis Signaling Downstream of RIP3 Kinase. *Cell 148*(1-2), 213–227.

Sun, Y., R. N. Day, and A. Periasamy (2011, sep). Investigating protein-protein interactions in living cells using fluorescence lifetime imaging microscopy. *Nature protocols 6*(9), 1324–40.

Susin, S. A., N. Zamzami, M. Castedo, T. Hirsch, P. Marchetti, A. Macho, E. Daugas, M. Geuskens, and G. Kroemer (1996, oct). Bcl-2 inhibits the mitochondrial release of an apoptogenic protease. *The Journal of experimental medicine 184*(4), 1331–41.

Suzuki, M., R. J. Youle, and N. Tjandra (2000, dec). Structure of Bax: coregulation of dimer formation and intracellular localization. *Cell 103*(4), 645–54.

Szymborska, a., a. de Marco, N. Daigle, V. C. Cordes, J. a. G. Briggs, and J. Ellenberg (2013). Nuclear Pore Scaffold Structure Analyzed by Super-Resolution Microscopy and Particle Averaging. *Science 341*(6146), 655–658.

Takacs-Vellai, K., T. Vellai, A. Puoti, M. Passannante, C. Wicky, A. Streit, A. L. Kovacs, and F. Müller (2005, aug). Inactivation of the Autophagy Gene bec-1 Triggers Apoptotic Cell Death in C. elegans. *Current Biology 15*(16), 1513–1517.

Tan, Y. J., W. Beerheide, and A. E. Ting (1999, feb). Biophysical characterization of the oligomeric state of Bax and its complex formation with Bcl-XL. *Biochemical and biophysical research communications 255*(2), 334–9.

Terrones, O., B. Antonsson, H. Yamaguchi, H.-G. Wang, J. Liu, R. M. Lee, A. Herrmann, and G. Basañez (2004, jul). Lipidic pore formation by the concerted action of proapoptotic BAX and tBID. *The Journal of biological chemistry 279*(29), 30081–91.

Todt, F., Z. Cakir, F. Reichenbach, R. J. Youle, and F. Edlich (2013, mar). The C-terminal helix of Bcl-x(L) mediates Bax retrotranslocation from the mitochondria. *Cell death and differentiation 20*(2), 333–42.

Tsujimoto, Y., L. R. Finger, J. Yunis, P. C. Nowell, and C. M. Croce (1984, nov). Cloning of the chromosome breakpoint of neoplastic B cells with the t(14;18) chromosome translocation. *Science (New York, N.Y.) 226*(4678), 1097–9.

Tsujimoto, Y., T. Nakagawa, and S. Shimizu. Mitochondrial membrane permeability transition and cell death. *Biochimica et biophysica acta 1757*(9-10), 1297–300.

Ugarte-Uribe, B. and A. J. García-Sáez (2014). Membranes in motion: mitochondrial dynamics and their role in apoptosis. *Biological chemistry 395*(3), 297–311.

Ugarte-Uribe, B., H.-M. Müller, M. Otsuki, W. Nickel, and A. J. García-Sáez (2014). Dynamin-related Protein 1 (Drp1) Promotes Structural Intermediates of Membrane Division. *Journal of Biological Chemistry 289*(44), 30645–30656.

Unsay, J. D., K. Cosentino, Y. Subburaj, and A. J. García-Sáez (2013). Cardiolipin effects on membrane structure and dynamics. *Langmuir : the ACS journal of surfaces and colloids 29*(51), 15878–87.

Urban, N. T., K. I. Willig, S. W. Hell, and U. V. Nägerl (2011, sep). STED nanoscopy of actin dynamics in synapses deep inside living brain slices. *Biophysical journal 101*(5), 1277–84.

Vandenabeele, P., L. Galluzzi, T. Vanden Berghe, and G. Kroemer (2010, oct). Molecular mechanisms of necroptosis: an ordered cellular explosion. *Nature reviews. Molecular cell biology 11*(10), 700–14.

Vaux, D. L., S. Cory, and J. M. Adams (1988, sep). Bcl-2 gene promotes haemopoietic cell survival and cooperates with c-myc to immortalize pre-B cells. *Nature 335*(6189), 440–2.

Wakabayashi, J., Z. Zhang, N. Wakabayashi, Y. Tamura, M. Fukaya, T. W. Kensler, M. Iijima, and H. Sesaki (2009, sep). The dynamin-related GTPase Drp1 is required for embryonic and brain development in mice. *The Journal of cell biology 186*(6), 805–16.

Walczak, H. and P. H. Krammer (2000, apr). The CD95 (APO-1/Fas) and the TRAIL (APO-2L) apoptosis systems. *Experimental cell research 256*(1), 58–66.

Wallrabe, H. and A. Periasamy (2005, feb). Imaging protein molecules using FRET and FLIM microscopy. *Current opinion in biotechnology 16*(1), 19–27.

Wasiak, S., R. Zunino, and H. M. McBride (2007). Bax/Bak promote sumoylation of DRP1 and its stable association with mitochondria during apoptotic cell death. *Journal of Cell Biology 177*(3), 439–450.

Wei, M. C., T. Lindsten, V. K. Mootha, S. Weiler, A. Gross, M. Ashiya, C. B. Thompson, and S. J. Korsmeyer (2000, aug). tBID, a membrane-targeted death ligand, oligomerizes BAK to release cytochrome c. *Genes & development 14*(16), 2060–71.

Wei, M. C., W. X. Zong, E. H. Cheng, T. Lindsten, V. Panoutsakopoulou, A. J. Ross, K. A. Roth, G. R. MacGregor, C. B. Thompson, and S. J. Korsmeyer (2001, apr). Proapoptotic BAX and BAK: a requisite gateway to mitochondrial dysfunction and death. *Science (New York, N.Y.) 292*(5517), 727–30.

Westphal, D., G. Dewson, M. Menard, P. Frederick, S. Iyer, R. Bartolo, L. Gibson, P. E. Czabotar, B. J. Smith, J. M. Adams, and R. M. Kluck (2014). Apoptotic pore formation is associated with in-plane insertion of Bak or Bax central helices into the mitochondrial outer membrane. *Proceedings of the National Academy of Sciences 111*(39), E4076–E4085.

Westphal, V., S. O. Rizzoli, M. A. Lauterbach, D. Kamin, R. Jahn, and S. W. Hell (2008, apr). Video-rate far-field optical nanoscopy dissects synaptic vesicle movement. *Science (New York, N.Y.) 320*(5873), 246–9.

Whelan, R. S., K. Konstantinidis, A.-C. Wei, Y. Chen, D. E. Reyna, S. Jha, Y. Yang, J. W. Calvert, T. Lindsten, C. B. Thompson, M. T. Crow, E. Gavathiotis, G. W. Dorn, B. O'Rourke, and R. N. Kitsis (2012, apr). Bax regulates primary necrosis through mitochondrial dynamics. *Proceedings of the National Academy of Sciences of the United States of America 109*(17), 6566–71.

Willig, K. I., R. R. Kellner, R. Medda, B. Hein, S. Jakobs, and S. W. Hell (2006, sep). Nanoscale resolution in GFP-based microscopy. *Nature methods 3*(9), 721–3.

Willis, S. N., L. Chen, G. Dewson, A. Wei, E. Naik, J. I. Fletcher, J. M. Adams, and D. C. S. Huang (2005, jun). Proapoptotic Bak is sequestered by Mcl-1 and Bcl-xL, but not Bcl-2, until displaced by BH3-only proteins. *Genes & development 19*(11), 1294–305.

Willis, S. N., J. I. Fletcher, T. Kaufmann, M. F. van Delft, L. Chen, P. E. Czabotar, H. Ierino, E. F. Lee, W. D. Fairlie, P. Bouillet, A. Strasser, R. M. Kluck, J. M. Adams, and D. C. S. Huang (2007, feb). Apoptosis initiated when BH3 ligands engage multiple Bcl-2 homologs, not Bax or Bak. *Science (New York, N.Y.) 315*(5813), 856–9.

Wong, J. L. and G. M. Wessel (2008, jan). FRAP analysis of secretory granule lipids and proteins in the sea urchin egg. *Methods in molecular biology (Clifton, N.J.) 440*, 61–76.

Xu, K., G. Zhong, and X. Zhuang (2013, jan). Actin, spectrin, and associated proteins form a periodic cytoskeletal structure in axons. *Science (New York, N.Y.) 339*(6118), 452–6.

Xu, S., E. Cherok, S. Das, S. Li, B. A. Roelofs, S. X. Ge, B. M. Polster, L. Boyman, W. J. Lederer, C. Wang, and M. Karbowski (2016, jan). Mitochondrial E3 ubiquitin ligase MARCH5 controls mitochondrial fission and cell sensitivity to stress-induced apoptosis through regulation of MiD49 protein. *Molecular biology of the cell 27*(2), 349–59.

Yang, R.-F., G.-W. Zhao, S.-T. Liang, Y. Zhang, L.-H. Sun, H.-Z. Chen, and D.-P. Liu (2012, nov). Mitofilin regulates cytochrome c release during

apoptosis by controlling mitochondrial cristae remodeling. *Biochemical and biophysical research communications 428*(1), 93–8.

Yao, Y., L. M. Fujimoto, N. Hirshman, A. A. Bobkov, A. Antignani, R. J. Youle, and F. M. Marassi (2015, jul). Conformation of BCL-XL upon Membrane Integration. *Journal of molecular biology 427*(13), 2262–70.

Zakeri, Z., D. Quaglino, and H. S. Ahuja (1994, sep). Apoptotic cell death in the mouse limb and its suppression in the hammertoe mutant. *Developmental biology 165*(1), 294–7.

Zaltsman, Y., L. Shachnai, N. Yivgi-Ohana, M. Schwarz, M. Maryanovich, R. H. Houtkooper, F. M. Vaz, F. De Leonardis, G. Fiermonte, F. Palmieri, B. Gillissen, P. T. Daniel, E. Jimenez, S. Walsh, C. M. Koehler, S. S. Roy, L. Walter, G. Hajnóczky, and A. Gross (2010, jun). MTCH2/MIMP is a major facilitator of tBID recruitment to mitochondria. *Nature cell biology 12*(6), 553–62.

Zhang, X., Y. H. Tee, J. K. Heng, Y. Zhu, X. Hu, F. Margadant, C. Ballestrem, A. Bershadsky, G. Griffiths, and H. Yu (2010, nov). Kinectin-mediated endoplasmic reticulum dynamics supports focal adhesion growth in the cellular lamella. *Journal of cell science 123*(Pt 22), 3901–12.

Zhou, L. and D. C. Chang (2008, jul). Dynamics and structure of the Bax-Bak complex responsible for releasing mitochondrial proteins during apoptosis. *Journal of cell science 121*(Pt 13), 2186–96.